High-speed phase-stable swept source optical coherence tomography: functional imaging and biomedical applications

Yuye Ling

Submitted in partial fulfillment of the

requirements for the degree

of Doctor of Philosophy

in the Graduate School of Arts and Sciences

COLUMBIA UNIVERSITY

2018

ABSTRACT

High-speed phase-stable swept source optical coherence tomography: functional imaging and biomedical applications

Yuye Ling

In the past decades, the performance of swept source optical coherence tomography (SS-OCT) has experienced an unprecedented improvement which is mainly driven by the rapidly evolving laser technologies: the state-of-art SS-OCT is now tens of dB more sensitive, six orders of magnitude faster, and seeing ten times deeper than the original version of time domain OCT. Regardless of the abovementioned progress, the phase instability is always considered the biggest weakness of SS-OCT and the mainstream belief often states that the mechanical tuning mechanism of the swept source is to blame.

In my study, I first developed a high-speed phase-stable SS-OCT based on a new-generation akinetic laser source, which is electrically tuned in wavelength, in the hope of reducing the phase noise to a shot-noise limited level. The experimental results turned out to be contradicted to the conventional phase noise theory, which inspires my discovery of a completely new interpretation for the phase noise in SS-OCT: I proposed that the timing jitter and scanning variability has to be taken into the consideration in the noise model as multiplicative noises. The

theory was later validated by another SS-OCT using a different light source. This study for the first time articulated the phase noise's origin and composition in the SS-OCT.

Although the SS-OCT performs relatively worse in phase stability compared with its spectral-domain counterpart (SD-OCT), it is still valuable since it images at a much faster rate than SD-OCT. Therefore, a better temporal resolution could be achieved, which is particularly attractive in areas such as time lapse imaging. I therefore utilize the system along with other two systems to conduct *ex vivo* imaging on human tracheobronchial epithelium. It is shown that the SS-OCT system could achieve equally good performance in this task. Moreover, thanks to the higher temporal and temporal frequency resolution, finer structure within the frequency response of the ciliary motion is picked up by our system.

During the study of *ex vivo* ciliary imaging, one of the challenges I was confronted with was the enormous amount of data generated by the SS-OCT, especially when high temporal frequency resolution is required. We thus came up with an idea of applying the compressive sensing (CS) to reduce the data size. Currently, we have demonstrated some preliminary results with using CS on reference *k*-clock channel compression. In the future, we will apply the same theory to compress the sample channel data, especially or time lapse OCT imaging.

Table of Contents

List of Figures vii

List of Tables xv

Acknowledgement xvi

Chapter 1 Introduction 1

1.1 OCT theory 2

1.1.1 Imaging theory 3

1.1.2 Physical implications 7

1.1.3 Noise theory 8

1.1.4 Data processing 9

1.2 OCT metrics: a comparative study between SD-OCT and SS-OCT 11

1.2.1 Imaging rate 11

1.2.2 Axial resolution 12

1.2.3 Coherence length and signal fall-off 13

1.2.4 Phase noise 14

1.3 OCT's opportunities and challenges 16

1.4 Outline of the dissertation 17

Chapter 2 The architecture of the SS-OCT system 19

2.1 The GUI 20

2.1.1 Multithreading 21

2.1.2 Signal and slot 24

2.2 Analog-digital interfacing sub-system 24

2.2.1 Data acquisition 25

2.3 Data processing, storage, and visualization 27

2.3.1 GPU computing 27

2.3.2 File input/output 29

2.3.3 Image visualization 29

2.4 Trigger configuration 29

2.4.1 A-line trigger 29

2.4.2 Frame trigger 29

2.5 Summary 30

Chapter 3 Optical system design 31

3.1 Sample arm 33

3.1.1 Sample arm design and simulation 35

3.1.2 Experimental evaluation 40

3.2 Discussions 41

3.2.1 System alignment 41

3.2.2 Discussion on SNR measurement 43

Chapter 4 Software development for SS-OCT system 44

4.1 Objectives 44

4.2 Device drivers 45

4.2.1 Mirror control 45

4.2.2 Data acquisition 50

4.3 Data processing by using GPU 52

4.3.1 Parallel computing 52

4.3.2 CUDA basics 53

4.3.3 Kernels and functions 54

4.3.4 Optimization 58

Chapter 5 Phase-resolved OCT 64

5.1 The theory of phase sensitive OCT 65

5.2 The source of the phase noise 67

5.3 Phasor interpretation of the noise 70

5.4 Calculation of the phase noise 71

5.4.1 Analytic analysis 71

5.4.2 Monte Carlo Simulation 72

5.5 Experimental verification 75

5.6 Summary 77

Chapter 6 High speed imaging of *ex vivo* human ciliary motion 78

6.1 Introduction 78

6.1.1 Objective 81

6.2 Method 82

6.2.1 Sample preparation 82

6.2.2 Experiment procedure 82

6.2.3 Image protocol 83

6.2.4 Histology processing 84

6.2.5 Post processing 84

6.3 Results 89

6.3.1 OCT structural image 89

6.3.2 Speckle variance image of ciliated epithelium layer 91

6.3.3 Temporal frequency analysis on the ciliary beat frequency 93

6.3.4 Phase variance analysis 95

6.3.5 Qualitative flow image 98

6.3.6 Quantitative flow analysis 99

6.4 Discussions 100

6.4.1 The noise from residual mucus in speckle variance imaging 101

6.4.2 Study limitations 102

6.4.3 Measuring CBF by using OCT 103

Chapter 7 Compressive sensing based SS-OCT 104

7.1 Theory 104

7.2 Previous research 106

7.3 Experiment configurations and procedures 107

7.4 Experimental results 110

7.4.1 Intensity based evaluation 110

7.4.2 Phase based evaluation 112

7.5 Compressed sensing in sample data compression 113

7.5.1 Frequency-constrained robust principal component analysis 114

7.5.2 Discussion 116

Chapter 8 Summary and future works 117

8.1 Improve the phase stability in SS-OCT based on the new theoretical framework 118

8.2 Observing new features in ciliary motion and connecting it with clinical significance ... 118

8.3 Study the possibility of using compressive sensing in sample arm 118

Bibliography 119

List of Figures

Figure 1-1 The schematics of three different types of OCT. (a) Time-domain OCT (TD-OCT), which uses a broadband light source along with a scanning reference mirror. The signal is detected by a photodetector. (b) Spectral-domain OCT (SD-OCT): the scanning reference mirror of the TD-OCT is replaced by a static mirror and a spectrometer is used to detect the interference signal. (c) Swept-source OCT (SS-OCT): a wavelength swept laser source is installed as the illumination. The scanning reference arm is made static, while the photodetector from the TD-OCT is kept.... 3

Figure 1-2 Layered model of OCT. The sample used in OCT could be assumed a collection of multiple discrete reflective layers. The backscattered light, which is the signal in OCT, is a superposition of the reflected light all the layers. 4

Figure 1-3 The flow diagram for processing SS-OCT data. 10

Figure 2-1 The block diagram of an exemplary SS-OCT system. The system including four sub-systems including graphic user interface, data processing, A/D interfacing and imaging. 19

Figure 2-2 The GUI for the SS-OCT system. 20

Figure 2-3 The sequence diagram for the entire SS-OCT software with (a) single thread, (b) multithread. 22

Figure 2-4 The multi-threading implementation of the application. Signal 1 will be emitted once the “acquisition” button is pressed in the GUI. Once slot 1, which is connected with the signal 1, receive the signal, the host thread “Data acquisition” will start. After the data stream fills one buffer, signal 2 will be emitted to notify the slot 2 that the data is ready and could be sent for post processing. Finally, the processed data will be transferred back to the GUI via “signal 3-to-slot 3” connection for final visualization..... 23

Figure 2-5 The data throughput of the DAQ board used in the proposed system. 26

Figure 2-6 An illustrative block diagram for GPU data processing. Two channels of analog signals are digitized by a DAQ board and later transferred to the host memory at the full speed. After that, one every ten B-scans will be sent to the GPU for *real-time* processing. 28
Figure 3-1 The schematic of the proposed highly phase-stable high-speed SS-OCT. The entire system could be divided into two sub-systems: an OCT imaging engine, and a simultaneously recorded *k*-reference clock. 32
Figure 3-2 Ideal layout of a 1D laser scanning microscope. Scanning is achieved by placing the scan mirror's rotation axis at the focal plane of the scan lens. The scan lens together with the tube lens form an afocal telescope system that projects an expanded image of the laser beam from the galvanometric mirror onto the objective pupil (or back-focal plane) that only pivots within the objective pupil without any lateral shift. As the focused spot moves across the sample, it generates fluorescence which is collected by the objective and in the case of twophoton laser scanning microscopy, directed on to one or more detectors by a dichroic mirror placed between the tube lens and objective. [Adapted] with permission from ref [66], [OSA]. 33
Figure 3-3 The optical design of the OCT sample and the configuration for the computer simulation in OpticStudio (version 14.2 SP3, Zemax, USA). The incident light is first collimated by a collimation package before being deflected by a MEMS scanner. The beam is then expanded by an afocal telescope. It is finally focused by an objective lens. 36
Figure 3-4 Spot diagram of the sample arm optics at different planes (columns) including the focal plane (middle column) obtained in OpticStudio. The first row shows the on-axis results, while the second and the third row gives the results when the mirror is rotated by 5 ºand 10 º, respectively. 38

Figure 3-5 (a) The field curvature and (b) the F-Theta distortion of the sample arm optics at different incident angles. The solid curves in different colors in (a) represent for the tangential focus of different wavelength, while the dashed curves coded in different colors stand for their sagittal counterparts. 39
Figure 3-6 The optical transfer function of the sample arm optics at different incident angle. Blue, green, red, yellow, purple and cyan represent 10 cycle/mm, 20 cycle/mm, 30 cycle/mm, 40 cycle/mm, and 50 cycle/mm, respectively. The solid lines show the tangential results and the dashed lines give the sagittal ones. 39
Figure 3-7 The actual optical assemble of OCT sample arm. 40
Figure 3-8 The standardized test for the OCT system. (a) The axial point spread function. (b) An en face image of resolution target. (c) The signal fall off plot of the system. 41
Figure 4-1 The current stand-alone MEMS mirror control program. 50
Figure 4-2 A block diagram for the GPU data processing of the SS-OCT data. The blocks in red, e.g. type casting, phase unwrap, and linear interp, are custom-implemented. 54
Figure 4-3 Block size & grid size optimizations for the typecasting kernel 59
Figure 4-4 Memory coalescing. 60
Figure 4-5 Execution time for type-casting kernel versus stride size (log2). 61
Figure 4-6 The error generated by using single-float cuFFT. 63
Figure 4-7 The error generated by using double cuFFT. 63
Figure 5-1 Effect of (a) scanning variability, (b) timing jitter, and (c) both on the scanning curve of SS-OCT. 68
Figure 5-2 A phasor depiction for the phase angle in SS-OCT. 70

Figure 5-3 Monte Carlo simulation of the proposed model. The calculated standard deviation of the final phase angle is first plotted as a pseudo-color image against SNR and W in logarithmic scale in (a). The σ_ψ are plotted against W in (b) and SNR in (c), respectively. 74

Figure 5-4 Experimental verification of the proposed model. (a) A No. 1 glass coverslip was tested by both SD-OCT and SS-OCT systems. The theoretical limit of SD-OCT was calculated using Choma's model 76

Figure 6-1. (a) H&E stained histology of trachea cross-section, (b) Scanning electron microscope image of ciliated cells. Reprinted with permission from ref [82], [OSA]. 79

Figure 6-2 An illustration for ciliary motion. Black lines represent the position of a single cilium during the effective stroke. Red lines represent the positions of a single cilium during the recovery stroke. 80

Figure 6-3 The flow diagram for speckle variance image processing. 85

Figure 6-4 The flow diagram for temporal frequency analysis. 86

Figure 6-5 A schematic shows the particle pairing algorithm. Starting with the #n bead (red) in i^{th} frame, I first search the image and found #m bead (green) in the neighborhood within a pre-defined radius. 88

Figure 6-6 Human tracheobronchial tissue OCT images (a), (c), (e), and (g) and corresponding H&E stained tissue section (b), (d), (f), and (h). The OCT images were imaged by Thorlabs Telesto system. BM: Basement membrane, C: Cartilage ring. CE: Ciliated Epithelium, M: Mucus. MG: Mucus secreting glands. MD: Mucus gland duct. PC: Perichondrium. 90

Figure 6-7 Observation of mucus excretion and its effect (a) Mucus secreted from the mucus gland duct. (b) Mucus layer is protecting the epithelium from the microspheres. A: 5.15 μm microspheres. M: Mucus. MD: Mucus gland duct. T: Tracheal wall. 90

Figure 6-8 The calculated speckle variance image in comparison with its corresponding H&E stained tissue. (a) The calculated speckle variance image, where the ciliated epithelium has a higher variance than other parts of the sample. It is visualized as a layer on top of the specimen. Two zoom-in regions (b) and (d) of the speckle variance image and their corresponding H&E stained tissue (c) and (e). In (b), the entire specimen is covered by ciliated epithelium as confirmed in (c). In (d), there are two regions, where no high contrast layer-like structure is presented. Those two regions are not covered by cilia, which is verified by the H&E stained tissue (e). NC: cilia-denuded. C: ciliated epithelium. Note: the protrusions that C1 pointed to in (d) is really an interpolation artifact instead of cilia. The cilia are represented by the high intensity layer beneath. 92

Figure 6-9 Three-dimensional visualization of human tracheal specimen. The volumetric dataset consists of 500 pixels (width) x 45 pixels (length) x 1024 pixels (depth) and was obtained by using the customized scanning protocol with high resolution SDOCT detailed in the method section. (a) Structural image overlaid against threshold variance image. The ciliary motion is only observed on the right half surface of the sample (b) The cross-sectional view of the sample, and (c) its corresponding variance image. M: mucus. CE: ciliated epithelium, which is visible in speckle variance image. T: trachea 93

Figure 6-10 The temporal frequency analysis on the ciliary beat frequency of human trachea sample with the presence of mucus layer (sample 13). (a) A color-coded spatial map of dominant frequency amplitude after thresholding and normalization. The pseudo-color spatial map was overlaid with the original intensity OCT image. (b) Speckle variance image. (c) A color-coded spatial map of dominant frequency. The pseudo-color spatial map was overlaid with the original intensity OCT image. (d) The temporal spectra of two locations. The red curve represents the ciliated epithelium, and the blue curve represents the cilia-denuded epithelium. We observed an 8

Hz peak on ciliated epithelium. The original intensity OCT image was averaged 4 times. All images were taken by the custom-built high-resolution SD-OCT system. CE: ciliated epithelium. CD: cilia-denuded epithelium 94
Figure 6-11 Structural image of human ciliated epithelium (averaged 10 times). 95
Figure 6-12 Functional imaging of human ciliated epithelium with various techniques. (a) Speckle variance imaging, (b) temporal frequency analysis, (c) phase variance (over the entire 2000 frames), (d) averaged phase difference overlaid on the structural image. We observed elevated contrast from ciliated epithelium region by using all techniques. For better visualization, the structural images are contrast-enhanced. I, II, and III represent for ciliated, background, and cilia-denuded regions, respectively. 96
Figure 6-13 The temporal frequency analysis of the human trachea sample. The temporal frequency response of four different locations including (a) ciliated site 1, (b) ciliated site 2, (c) air-medium interface site, and (d) ciliate denuded site. The temporal frequency responses obtained from the cilia sites show very high peaks around 9 Hz, while that of the cilia denuded region has mostly flat response over the entire spectrum. The temporal frequency response measured at air-medium interface presents elevated low frequency components, due to the higher reflectivity or intensity. (e) The selected regions are illustrated and marked in the structural image. All of them are representative single-pixel values. (f) The histogram of the peak frequencies extracted from ciliated sites. 97
Figure 6-14 The flow images of the microspheres induced by the beating of ciliated epithelium. (a) and (c) are MIP image by integrating all 200 B-scans. (b) and (d) are corresponding color-coded images. The time span of all the images are 16.627 s, while the 1st eighth interval of the entire time

duration is colored by red, the 2nd of that is colored by yellow, …, and 8th of that is colored by purple. 98
Figure 6-15 The quantitative cilia-driven flow analysis. The dataset is the same as that in Figure 5(a). (a) The vector visualization of flow dynamics. The direction of the arrow represents the averaged flow direction and the flow rate is encoded in both arrow length and color. (b) The histogram of all the tracked particles inside the red box shown in (a). The total time duration is 16.627s and 2,251 microspheres are tracked. 100
Figure 7-1 Schematic of proposed down-sampling scheme. 108
Figure 7-2 Experimental results (a) The fully sampled original clock signal. (b) The randomly generated 2D mask. (c) The resultant down-sampled clock signal. (4) The reconstructed clock signal. (e) The residual error. 110
Figure 7-3 The experimental results on the intensity reconstruction quallity. (a) 111
Figure 7-4 Measured phase noise at mirror surface at different SNR levels and different sampling/calibration strategies..... 112
Figure 7-5 (a) *Ex-vivo* OCT B-scan image of ciliated epithelium from human trachea (Sample 5) and (b) corresponding histology. (c) The Maximum Intensity Projection of the FC-RPCA sparse output painted over the image in (a) using MATLAB's jet colormap. (d) A closer look at a dense area of cilia located directly under a mucus cloud from (c). In contrast, (f) examines a sparsely populated area of cilia where the cells may be damaged or non-functioning. (e) and (g) are closer views of the histology corresponding to (d) and (f), respectively. The locations of these two regions are marked with the corresponding figure letter in the full view histology (b) and OCT B-scan (c) images. Colorbar indicates normalized intensity of the FC-RPCA sparse component. The arrows

and corresponding labels mark key physiological regions (CE = ciliated epithelium, BM = basement membrane, M = mucus). 114
Figure 7-6 Differences between FC-RPCA and Speckle Variance. Left image is the FC-RPCA overlay (the same image shown in manuscript Figure 7-5(c)) and the right is the Speckle Variance overlay for the same dataset. 115

List of Tables

Table 6-1 Imaging system configuration for B-scan imaging 83

Acknowledgement

It has been slight over four years since I first landed in the Morningside Heights campus, and I finally reached this emotional moment to officially conclude my doctoral study. My utmost gratitude and appreciations goes to my beloved family. Thanks to my father for his teaching. He always told me “It’s dogged that does it”, which I always remember. Thanks to my mother for her caring. I missed her cooking so much. As the only kid to my parents and the only grandson to my grandparents, I was a spoiled kid since I was born. It is their unconditional love and support that energized me to conduct scientific research at a place thousands miles away from home.

My greatest gratitude also goes to my advisor Dr. Christine P. Hendon. I was really lucky to have Christine as my advisor, because she is simply the best advisor I could ever ask for. Her guidance on my doctoral research is indispensable, without which my dissertation will not possibly be written. In addition to that, she always encourages me to think big and novel, which makes some my boldest or even heretical ideas later turns into quality researches. More importantly, she is such a supportive mentor and always stand by my side whenever I was encountered with obstacles along my way. I still recall the frustration that filled within me in the spring of 2016, when I shared that with Christine. During that time, some of my peers was starting to getting published and graduating, while there is no progress on my side. She soon assigned me a collaborative work with Dr. Michael Choma in a totally different area, which later led to my first publication. After that, it was just like magic: good results were obtained one after another.

I would also like to thank my committee members, Dr. Keren Bergman, Dr. Ioannis (John) Kymissis, Dr. Elizabeth S. Olson, and Dr. Elsa Angelini for serving as my committee members and offering advice, support and encouragement.

Special appreciations go to the team we have in Structure Function Imaging Laboratory: Dr. Yu Gan, Dr. Xinwen Yao, Rajinder Singh-Moon, Theresa Lye, Nathan C. Lin, Diana Mojahed, and McLean James. It was my greatest honor and pleasure to work with all of them. The time I have spent in the office and laboratory is so enjoyable and I will definitely miss them.

In Memory of My Grandmother Xuihua Cai,

and My Grandfather Zugui Cao

Chapter 1 Introduction

Optical coherence tomography (OCT) is an optical imaging modality based on low-coherence interferometry (LCI), whose theory has been extensively studied in the past [1]. By taking advantage of the short coherence length of a broadband light source, the axial and lateral resolution, both of which are micrometer-level, are de-coupled in OCT: the lateral resolution is ruled by the optical design, while the axial resolution at the image plane is solely dependent on the bandwidth of the light source. If being operated within the near infrared (NIR) regime, a moderate penetration depth (1~3 mm in tissue) could usually be achieved in OCT. These features make OCT a very suitable tool for both *in vivo* and *ex vivo* biomedical applications where a noninvasive and nondestructive high-resolution imaging techniques is highly sought after [2, 3].

Compared with its predecessors such as optical coherence-domain reflectometry [4-6], modern OCT possesses huge advantages in performance partially thanks to the technological advances in the related field including lasers [7-9], photodetectors [10, 11], and electronics [12]. For example, a state-of-art spectral-domain OCT system equipped with a Fourier-domain mode locking (FDML) laser, high-speed balanced photodetectors and a Giga-hertz digitizer could render real-time Giga-voxel volumetric structural images of the sample to the users [13].

Since its invention in 1991 [14], OCT has achieved an unprecedented success in the past 26 years. Especially, OCT has now evolved into a standard of care in ophthalmology for retinal diseases and glaucoma [15]. It is estimated now that more than 10,000 OCT units have been sold and ~20 million ophthalmic OCT images are performed worldwide in clinical settings [16]. However, there are also some technical challenges for OCT alongside the rapid growth.

In this chapter, I will first give a brief introduction on the OCT theory, which is followed by a discussion on its instrumental features. A summary of the current usage of the technology is provided, and the future directions of the technology is also discussed.

1.1 OCT theory

The optical arrangement of OCT is very similar to that of a Michelson interferometer except that the monochromatic illumination is replaced by a broadband light source. The illumination is first split into two branches, a reference arm and a sample arm, where the mirror is replaced by an object. The reflected light from both arms are later re-combined and interfere on the surface of the detector.

OCT could be categorized into three types including time-domain OCT (TD-OCT), spectral domain OCT (SD-OCT) and swept source OCT (SS-OCT) based on the different choices of the light sources, reference mirror configurations, and the detection schemes as illustrated in Figure 1-1. For example, TD-OCT detects the power density of the interference signal, when a broadband illumination is used. By scanning the reference mirror in the axial direction, an interference fringe could be obtained in the time domain. The de-modulated signal envelope provides an one-dimensional depth profile of the sample [17]. Based on the Fourier diffraction theorem [18], Fercher *et al.* pointed out that the depth profile of the sample could be obtained by conducting a single Fourier transform on the measured scattered spectrum: scanning the reference arm in the spatial domain z is equivalent to scanning the interference signal in the wavenumber domain k followed by a Fourier transform [19]. Two different implementations were thus proposed, and they are collectively called Fourier domain OCT (FD-OCT). The first one is SD-OCT, which spatially disperses the wavenumber k, and the other one is SS-OCT, which temporally disperses k. In SD-OCT, the same broadband light source as that in TD-OCT is used, while the signal is detected by a

spectrometer with a linear camera [19, 20]. On the other hand, SS-OCT adopts a totally different light source: the wavelength swept laser source is essentially a rapidly tunable laser. Therefore, a simple photodetector similar to that of TD-OCT is sufficient to detect the signal [20, 21]. Due to the superior performance of FD-OCT in terms of signal-to-noise ratio (SNR), imaging speed (A-line rate), phase stability, and portability, among others, TD-OCT is mostly superseded by FD-OCT with very few exceptions [22-24]. Therefore, I will only focus on the theory of FD-OCT in the following sections.

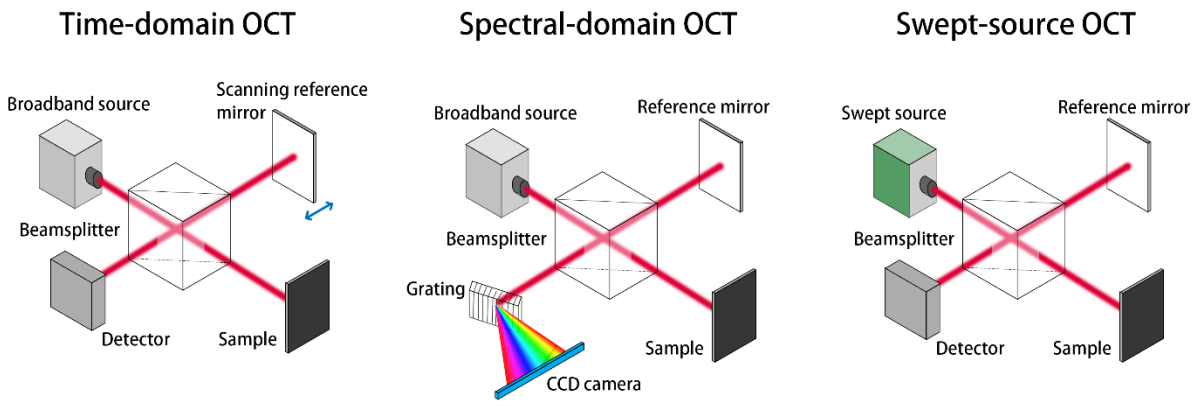

Figure 1-1 The schematics of three different types of OCT. (a) Time-domain OCT (TD-OCT), which uses a broadband light source along with a scanning reference mirror. The signal is detected by a photodetector. (b) Spectral-domain OCT (SD-OCT): the scanning reference mirror of the TD-OCT is replaced by a static mirror and a spectrometer is used to detect the interference signal. (c) Swept-source OCT (SS-OCT): a wavelength swept laser source is installed as the illumination. The scanning reference arm is made static, while the photodetector from the TD-OCT is kept.

1.1.1 Imaging theory

In most real-world applications including biomedical imaging, the sample under inspection could be any random object. The interaction between the light and the object is usually very complicated and a thorough and rigorous study often requires solving an inverse scattering problem, in which

the illumination and scattering field is known and the scattering potential of the object would be extracted [18, 25].

However, it has been proven sufficient to adopt a simple hybrid model to describe the process: the sample could be modelled as a continuous collection of reflectors with infinitesimal thickness and its interaction with the light is in the scope of geometric optics, while the interference between the reference field and sample field is described by wave optics [26].

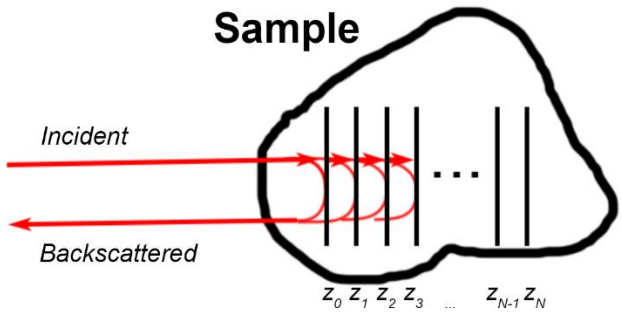

Figure 1-2 Layered model of OCT. The sample used in OCT could be assumed a collection of multiple discrete reflective layers. The backscattered light, which is the signal in OCT, is a superposition of the reflected light all the layers.

The layered model of the object is illustrated in Figure 1-2. Without losing generality, we could assume that the incident light field is a plane wave and study a single axial line of the sample. If we could further ignore the light attenuation occurred during its travelling within the tissue, the backscattered light from the sample could be calculated by summing up the reflected light from each reflector. The backscatter field could be written as,

$$E_S(k) = \int_0^\infty r(z)s(k)e^{-j2k2z}\mathrm{d}z \tag{1.1}$$

where $r(z)$ gives the spatial distribution of the object, and $s(k)$ is the emission spectrum of the light source. Here, I confine the support of the object function $r(z)$ to $z \geq 0$. It is worth noting that $r(z)$ could also be approximated by taking the square root of the reflectivity $R(z)$.

Accordingly, the reflected field from the mirror could be written as,

$$E_R(k) = \int_0^\infty \delta(z - z_0) s(k) e^{-j2k2z} \mathrm{d}z = s(k) e^{j2k2z_0} \tag{1.2}$$

where z_0 is the optical path length (OPL) between the light source and reference mirror. Therefore, the optically mixed signal at the surface of the photodetector will form a spectral interference fringe, whose intensity is given by,

$$I(k) = |E_S(k) E_R(k)|^2 = |E_S(k)|^2 + |E_R(k)|^2 + E_S(k) E_R^*(k) + \text{c.c.} \tag{1.3}$$

The detected signal consists of four terms. The first term on the right-hand side of Equation (1.3) denotes the autocorrelation term, while the second term represents for a DC background. Both terms are usually regarded as artifacts or noises in OCT images [27, 28]. Fortunately, most OCT system is operated in shot-noise limited regime, where the autocorrelation term is much smaller than the DC background and could thus be ignored. The third term, which is the interference term, provides the information that we are looking after and the fourth term is its complex conjugate. If I explicitly expand the third term (interference term), it could be written as,

$$I_{int}(k) = E_S E_R^* = |s(k)|^2 \cdot \int_0^\infty r(z) e^{-j2k2(z - z_0)} \mathrm{d}z \tag{1.4}$$

where the integral can be viewed as a Fourier transform of the object function $r(z)$ and the support of $r(z)$ is $[0, +\infty)$. If I perform an inverse Fourier transform on Equation (1.4), I could reach the following equation,

$$S(z) * r(\pi z / 2) = \mathcal{F}^{-1}\{I_{int}(k)\} \tag{1.5}$$

where $S(z)$ is the autocorrelation function of the $s(k)$ according to Wiener–Khinchin theorem. An important conclusion could be reached here: the obtained OCT image, which is the inverse Fourier transform of the interference signal, is not the original object $r(z)$ but rather its convoluted version with a blurring kernel $S(z)$. Therefore, the imaging quality (i.e. point spread function) of the image is heavily dependent on the point spread function of the $S(z)$, and a delta-function like $S(z)$ with small side lope is desired.

Since $S(z)$ is a band-limited function, its spatial bandwidth Δz_S is related to its spectral bandwidth Δk via the Fourier relationship,

$$\Delta z_S = \frac{2\pi}{\Delta k} \tag{1.6}$$

Equation (1.6) could be further rewritten in the wavelength domain,

$$\Delta z_S = \frac{2\pi}{\frac{2\pi}{\bar{\lambda} - \Delta\lambda/2} - \frac{2\pi}{\bar{\lambda} + \Delta\lambda/2}} = \frac{(2\bar{\lambda} - \Delta\lambda)(2\bar{\lambda} + \Delta\lambda)}{4\Delta\lambda} \approx \frac{\bar{\lambda}^2}{\Delta\lambda} \tag{1.7}$$

The approximation is valid as long as the bandwidth of the light source $\Delta\lambda$ is much smaller than the central wavelength $\bar{\lambda}$. It could be concluded from Equation (1.7) that the spatial bandwidth of the function $S(z)$ is proportional to the square of the central wavelength $\bar{\lambda}^2$ and inversely proportional to the $\Delta\lambda$. Therefore, a light source with large wavelength bandwidth $\Delta\lambda$ and a shorter central wavelength $\bar{\lambda}$ is often a better choice, if a high axial resolution system is to be built.

To better understand the OCT theory and some subtle differences brought by the discrete signal processing, I further derive a discrete domain version of the abovementioned equations. Let assume the analog-to-digital (AD) conversion is applied after the signal mixing (Equation(1.4)). The spectral resolution of the detection is δk, and the spectral bandwidth is Δk. Since sampling a function in the transform domain is equivalent to performing an inverse discrete-time Fourier transform (IDTFM) on the original function, the sampled spectral interference fringe is indeed the Fourier transform of the periodic summation of the original object function,

$$\begin{aligned} E_S[n]E_R^*[n] &= (|s(k)|^2 \cdot \int_0^\infty r(z)e^{-j2k2(z-z_0)}\mathrm{d}z) \cdot \sum_{n=0}^{M-1}\delta(k-n\delta k) \\ &= \frac{2}{\pi}|s(n\delta k)|^2 \cdot \mathcal{R}(\frac{2n\delta k}{\pi}) \end{aligned} \tag{1.8}$$

where $\mathcal{R}$ is the Fourier transform of $r(z)$. The inverse discrete Fourier transform is then applied to obtain the OCT signal in discrete domain,

$$S[n] * r[\pi n/2] = \mathcal{F}^{-1}\{E_S[n]E_R^*[n]\} \tag{1.9}$$

where

$$S[n] = S(z) \cdot \sum_{n=0}^{M-1}\delta(z-n\delta z) \tag{1.10}$$

1.1.2 Physical implications

This simplified theory turns out to be extremely powerful, and most of the important performance metrics of OCT could be inferred solely based on the theory described above.

1.1.2.1 Imaging range

The imaging range of OCT represents the longest OPL difference between the sample and the reference mirror that the system could image without aliasing. This value is depending on the

spectral sampling resolution δk due to the Fourier relationship. As we mentioned before, the sampled spectral interferogram is equivalent to the IDTFT of the original signal $r(z)$, which is then corresponding to the Fourier transform of $r(z)$ and its spatially shifted replica (period is given by $\pi/\delta k$). Therefore, the maximum imaging range of the OCT system without aliasing based on this scheme could not exceed $\pi/\delta k$.

1.1.2.2 Axial point spread function

The axial resolution of OCT is renowned for its decoupling from the optical system it resides: it is affected by neither the focusing optics nor the detection scheme (e.g. confocal gating).

Interestingly, it is only dictated by the bandwidth of the illumination spectrum $s(k)$. As indicated by Equation (1.9), the obtained OCT image after inversely Fourier transforming the spectral interferogram is the convolution of the original object function $r(z)$ and a blurring function $S[n]$. The axial point spread function (PSF) of the system is the blurring function $S[n]$.

Therefore, the emission spectrum $s(k)$ need to be carefully chosen. Otherwise, excessive side lobes will appear in the PSF $S[n]$, and thus impair the image quality. Tripathi *et al.* has previously suggested that spectral reshaping could be used to suppress this effect [29]. In addition, a zero-padding on the original sampled spectral interferogram before conducting IDFT could also increase the digital resolution and smooth the point spread function (PSF).

1.1.3 Noise theory

Another essential aspect with regard to OCT is the noise performance. The OCT signal is measured via optical intensity: In SD-OCT, a charged coupled device (CCD) converts the time-accumulated photons into charges, while a photodetector in SS-OCT senses the instantaneous optical intensity and generate electric current accordingly. In comparison, only averaged intensity is measured by

the first-generation time-domain technique. The OCT signal measured at wavenumber k_n in the system could be written as,

$$I_D[n] = \rho I[n] = \rho(|E_S[n]|^2 + |E_R[n]|^2 + E_S[n]E_R^*[n] + \text{c.c.}) \tag{1.11}$$

where ρ gives the responsivity of the opto-electronic device. Let first assume that the sample is a single mirror. The power at the peak location of the OCT image is given by the summation of $I_D[n]$ based on Parseval's Theorem,

$$\text{Signal} = \rho^2 r_S^2 r_R^2 I_{\text{total}}^2 \approx N\rho^2 r_S^2 r_R^2 I_{\text{pixel}}^2 \tag{1.12}$$

There are major types of noise in OCT: the thermal noise, relative intensity noise and the shot noise [23, 24, 30]. It is well known that the shot noise will dominate the other two, if the reference arm power is much larger than the signal arm power, which is usually the case in biomedical imaging since the sample (e.g. tissue) is weak in scattering. The shot noise power in this case could be approximated by an additive, uncorrelated Gaussian white noise and could be written as,

$$\text{Noise} = e\rho r_R^2 I_{\text{total}} B \tag{1.13}$$

where B is the bandwidth of the noise [31]. The signal-to-noise ratio (SNR) is then the ratio,

$$\frac{\text{Signal}}{\text{Noise}} = \frac{N\rho r_S^2 I_{\text{pixel}}}{eB} \tag{1.14}$$

Equation (1.14) shows that the SNR in OCT is not dependent on the sample arm power when the system is operated in shot-noise-limited regime.

1.1.4 Data processing

A flow diagram of data processing in SS-OCT is give in Figure 1-3. The reference *k*-clock is first discrete Hilbert transformed to obtain its corresponding analytic signal, from which the phase

angle is extracted. The extracted phase is unwrapped, and the resultant unwrapped phase is proportional to the wavenumber sweeping curve. After being centered and scaled according to the experimentally measurements, the curve is then used to linearly resample the sample spectrum. The recalibrated sample curve is therefore linear in the wavenumber *k* domain. A spectral reshaping is optional to optimize the axial PSF. Finally, an inverse fast Fourier transform (IFFT) is performed to obtain the OCT image (A-line). This process could also be applied to SD-OCT: the only difference is that the calibration signal (*k* curve) is directly measured from the spectrometer.

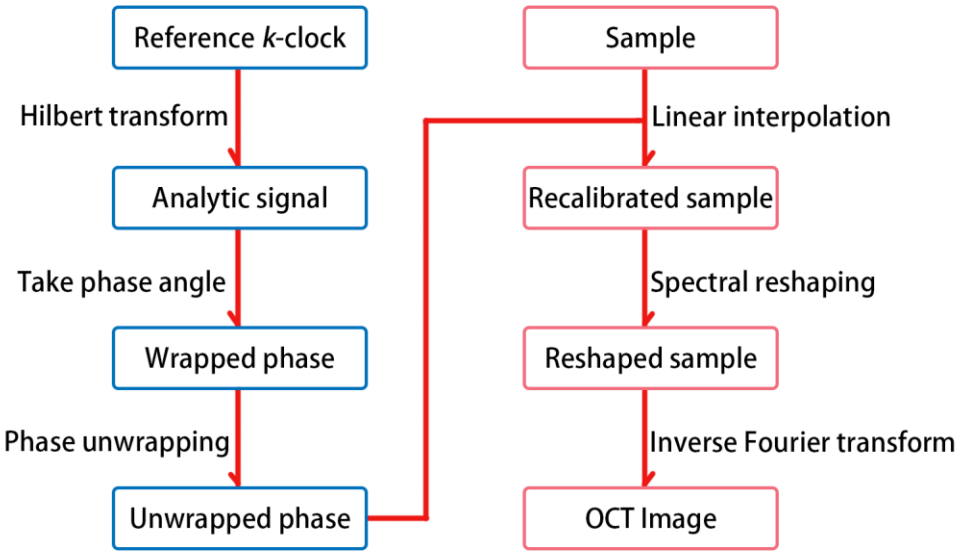

Figure 1-3 The flow diagram for processing SS-OCT data.

1.1.4.1 Discrete Hilbert transform

In most OCT literatures, the discrete Hilbert transform is often performed by first multiplying the spectrum of reference *k*-clock signal by a Heaviside function followed by an IFFT [32]. However, this process is not precise. Although it has been known for almost a century that the real part and

the imaginary part of a continuous causal signal's Fourier transform forms a Hilbert transform pair [33], it is difficult to find a proper equivalent of Hilbert transform in discrete time domain, which could satisfy all the properties as it is in the continuous time domain [34-36]. Recently, Kim *et al.* has proposed to perform the discrete Hilbert transform by complex FIR filtering [37]. This could a possible alternative to later implemented in our system.

1.1.4.2 Phase unwrapping

Phase unwrapping is another deceptively simple process: performing one-dimensional phase unwrapping is straightforward in a noise-free scenario, but it is extremely difficult if the wrapped phase is corrupted by noises or if the change in phase is too dramatic [38]. In my current study, only a simple discontinuities detection algorithm is used. In the future, I will further explore alternative ways to unwrap the phase to improve the phase performance.

1.2 OCT metrics: a comparative study between SD-OCT and SS-OCT

After an introductory discussion on the basic theory of FD-OCT, it seems that the SD-OCT and SS-OCT share the same mathematical formulation and theoretical framework. The only difference is manifested in the different form of implementations. In the following subsections, I will discuss some of the OCT performance metrics in a comparative way and detail how different flavors are introduced by different implementations.

1.2.1 Imaging rate

One of the major applications for OCT is *in vivo* clinical imaging. The key to success in this field is to image fast; the samples are often alive and various motions take place in clinical settings [39]. For example, in retinal imaging, the patient might have involuntary eye movements, which will

lead to severe motion artifacts if the imaging speed is slow [40]. Although it is possible to use post-processing techniques to correct the artifact [41], a fast imaging technique is always preferred.

In the past decade, the acquisition speed of both SD-OCT and SS-OCT have experienced dramatic improvements in the orders of magnitude. However, the SS-OCT is currently leading the tide: a typical SS-OCT could reach 200 kHz A-line rate easily [42-44], and the fastest commercial SS-OCT system could acquire over 10 million A-lines every second which is sufficient to render volumetric images at video rates [45].

To the contrary, the imaging rate of SD-OCT is limited by performance of CCD camera at two different levels. First of all, the CCD camera used in SD-OCT is an integral device. With increased A-line scan rate, the exposure time for individual A-line will be inevitably reduced, which will lead to a drop in SNR. Unlike the photodetector used in SS-OCT, it is not practical to amplify the electrical signal after photoelectric conversion; an amplification of the linear CCD camera would require a linear array of amplifiers. Secondly, the read-out time of the camera is dependent on the speed of the analog to digital converter (ADC) circuits equipped as well as the read-out schemes. These factors are both limited by the current integrated circuits design technologies, and is out of the scope of our current discussion. It is also worth noting that there is parallel SD-OCT that could reach very high A-line rate, but requires tremendous efforts to build and operate [46].

1.2.2 Axial resolution

The axial resolution is the full-width half maximum (FWHM) of the axial PSF by definition. Follow the discussion in section 1.1.2.2. and assume the shape $s(k)$ is Gaussian, we could directly calculate the FWHM of the axial PSF,

$$\text{FWHM} = \frac{2\ln 2 \cdot \bar{\lambda}}{\pi \cdot \Delta\lambda} \tag{1.15}$$

The resolution of the system is determined by two factors: central wavelength $\bar{\lambda}$ and the wavelength span $\Delta\lambda$. Equation (1.15) gives us an illusion that we could arbitrarily choose the combination, so that any desired resolution could be obtained. Unfortunately, there are multiple constraints existed.

For SS-OCT, it is difficult to increase the wavelength span $\Delta\lambda$ at the first place. The sweeping range is determined by the tunability of the underlying device, and there is an inherent trade-off to be made between the scanning range and the imaging rate.

Although this constraint does not exist in SD-OCT, there are other considerations. One of the most prominent issues is the optical design of a broadband spectrometer. With the increment on the emission bandwidth $\Delta\lambda$, the system will introduce significant chromatic aberration which will severely degrade the signal fall-off (section 1.2.3). Moreover, the sample dispersion will be exaggerated with larger bandwidth. Both the introduced chromatic aberration and dispersion will in turn lead to a degraded axial resolution.

1.2.3 Coherence length and signal fall-off

In FD-OCT, the coherence length is experimentally defined: it is the maximum OPL displacement of the reference arm when the peak intensity of a mirror surface's OCT image is dropped by 6 dB. The signal fall-off is defined accordingly as the decay rate, which is simply 6 dB divided by the coherence length. Therefore, a longer coherence length (or smaller signal fall-off) is more suitable for imaging a sample with complex morphology.

In general, SD-OCT has a shorter coherence length than SS-OCT, which is mainly due to the imperfect spectrometer design. Any aberrations introduced in spectrometer's optical design

will eventually result in a crosstalk between adjacent spectral components and lead to a wash-out in detected spectral interferogram. The fringe wash-out could be conceptualized as the OCT signal convoluted with a low-pass filter in the discrete wavenumber domain. After the inverse DFT (Equation (1.8)), the convolution in the wavenumber domain will be translated to a multiplication with a low-pass filter in the spatial domain, which attenuates the signal from deeper location.

Even if the optical aberration could be eliminated by advanced optical design, the limited size (resolution) of the camera pixel could still jeopardize the resolving of higher frequency fringes, which can be understood as another low-pass filter imposed on the wavenumber domain.

In contrast, the spectral fringes in SS-OCT is detected by a photodetector and later sampled by a data acquisition (DAQ) board in time domain. Thanks to the relatively high bandwidth of the photodetector and DAQ board, no such low-pass filtering occurs in the detection part of SS-OCT. However, in SS-OCT, the coherence length is fundamentally limited by the instantaneous linewidth of the light source. The emission of swept source could be seen as a parallelism of multiple monochromatic lasers. As for each monochromatic laser, its coherence length is simply the inversely proportional to its linewidth, which is determined by the quality factor of the cavity. The coherence lengths of these individual monochromatic lasers will collectively determine the coherence length of the system. Recently, with the miniaturization of the tuning devices, more and more swept sources are using extremely short cavity design and thus enabled very long coherence length [47].

1.2.4 Phase noise

There are several mathematical models to theoretically describe and analyze the phase noise of FD-OCT systems. Park *et al.*, proposed a phasor picture to understand the composition of the phase

noise in spectral-domain OCT (SD-OCT): the noise, which is much smaller than the signal, was modeled as a vector orthogonal to the signal vector with a random magnitude [48]. Choma *et al*., proposed a similar model [49] and further reframed it as a constant phasor plus additive white Gaussian noise (AWGN) problem: the noise was considered as a phasor with a constant magnitude but with a uniformly distributed random angle [50]. Szkulmowski *et al*., on the other hand, modeled the same problem as a constant phasor plus a sum of random phasors [51]. Despite the differences among these models, similar conclusions were drawn: the phase stability (sensitivity) of the FD-OCT measurement was found inversely proportional to the square root of the system's signal-to-noise ratio (SNR) if the system was shot noise limited [48-51]. In addition to the aforementioned studies based on SD-OCT, Vakoc *et al*., discussed the impact of the timing jitter on the phase performance of swept-source optical coherence tomography (SS-OCT), and they reached a similar conclusion that the phase stability of SS-OCT was also SNR limited.

Currently, phase-resolved OCT or related phase-sensitive techniques rely on the previously mentioned frameworks to predict the system's phase performance. Although the models generally fit the data from SD-OCT systems, their effectiveness was contested in SS-OCT platforms: the measured phase stability of SS-OCT could be orders of magnitude worse than the predictions [43, 52]. The experimental results I obtained from the proposed SS-OCT also deviated from the predicted value based on the theory, which inspires me to develop a new phase noise theory for SS-OCT. This will be discussed later in details (Chapter 5).

1.3 OCT's opportunities and challenges

After two decades' rapid evolving, OCT now is an indispensable tool in both clinical and basic research: OCT has been commercialized in various branches of medicines and is considered a standard of care in ophthalmology [53].

In cardiology, OCT could be implemented in the catheter form to perform intravascular inspections of intracoronary stenting [54]. It is also possible to integrate the OCT with other imaging modalities such intravascular ultrasound (IVUS) to real-time imaging the coronary [55]. In term of interventional medicine, researchers have also showcased the use of OCT to guide the radio frequency ablation (RFA) procedure [56].

In gastrointestinal imaging, endoscopic OCT have been used to inspecting various organs including esophagus [57], stomach, and colon [58].

Respiratory imaging is another application for endoscopic OCT. It has been recently presented that airway cilia and mucus clearance could be directly observed and evaluated by μOCT [59].

Towards the manifestation of optical biopsy [2], there are still a lot of hurdles confronted by the OCT technologies. Recent advance in SS-OCT makes it as the most suitable candidate: it possesses the high speed and long coherence length in order to be operated in *in vivo* clinical settings. However, there are still a lot of obstacles.

First of all, only structurally imaging the samples is often not sufficient. Additional contrasts are needed to identify different tissue types with similar structures. Various functional imaging extensions including polarization sensitive OCT [60], phase-resolved OCT [49],

spectroscopic OCT [61], and optical coherence elastography [62] have been proposed to provide additional contrasts. However, more efforts from the research community is required to fully understand the nature of these imaging extensions and provide solid proofs of their utilities in clinical settings.

Secondly, the increasing imaging rate of SS-OCT created more data to handle, process and store, which is a challenging task to engineer. For a typical SS-OCT operated at 200 kHz, more than 1.6 GB of data will be generated every second, and over 800,000 times 2048-point FFTs are needed to reconstruct the image.

Last but not the least, the increased imaging rate will eventually lead to performance degradation including imaging range, SNR, and axial resolution as we discussed in section 1.2. How to de-couple this relationship in SS-OCT is another interesting topic.

1.4 Outline of the dissertation

In this dissertation, I will describe the explorations I have made in the past four and half years. I first built a highly phase-stable, high-speed SS-OCT from scratch. Based on the experimental findings by using the custom system, I developed a new theory for explaining the phase noise in SS-OCT. The theory has been validated in two different systems. A series of clinically relevant researches are conducted on *ex vivo* human tissues including hearts and trachea. For human tracheal imaging, I reported the first time *ex vivo* visualization of ciliary beating and ciliary beating frequency (CBF) measurement. This result has a great clinical importance, as it might facilitate precise diagnosis of related diseases such as ciliary dyskinesia and cystic fibrosis. I also proposed a data reduction scheme based on the compressed sensing theory. The layout of the dissertation is given below.

In Chapter 2 to Chapter 4, I will first give a detailed explanation on the system development of the highly phase-stable, high-speed SS-OCT from scratch. The system architecture is given in Chapter 2, which is followed by a discussion on optical system design (Chapter 3). Chapter 3 will be focused on the realization of the software package including graphic user interface, data processing and data visualization unit.

In Chapter 5, the new phase noise theory I developed for SS-OCT is introduced. A full spectrum of study including analytical analysis, computer simulation, and experimental verification is conducted to support my argument.

In the next chapter (Chapter 6), I will describe how OCT could be used in the study of mucuciliary clearance in human. I conducted a comparative study by using three different OCT systems (1 SS-OCT and 2 SD-OCTs) with different specs. The first time *ex vivo* measurement of human ciliary beating frequency (CBF) will be reported.

Before concluding the dissertation, I will address the data issue in SS-OCT by introducing a compressive sensing (CS) based acquisition scheme in Chapter 7. It is demonstrated that a data reduction by at least 30% can be achieved without compromising the system performance. A potential way to further compress the data by applying CS is also discussed.

Last but not the least, a summary will be provided in Chapter 8 followed by a discussion on the future directions of my research.

Chapter 2 The architecture of the SS-OCT system

One of the main contributions of my dissertation is having developed a highly phase-stable high-speed SS-OCT system from scratch. In this chapter, I will paint the first stroke and start with the overall architecture design of the SS-OCT.

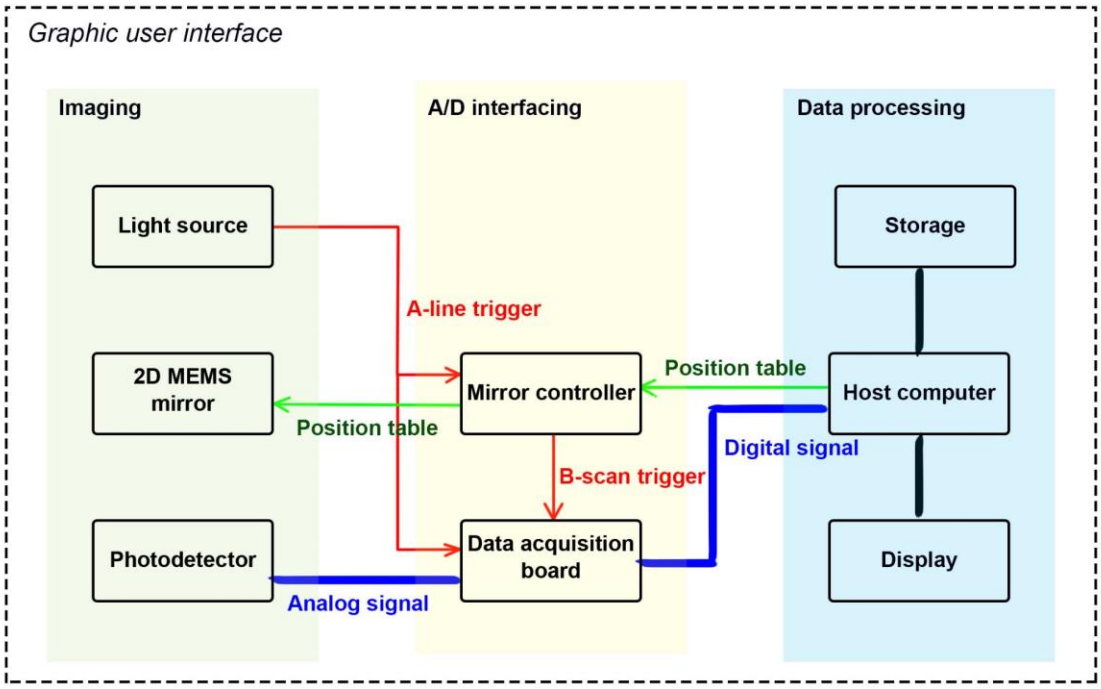

Figure 2-1 The block diagram of an exemplary SS-OCT system. The system including four sub-systems including graphic user interface, data processing, A/D interfacing and imaging.

A typical modern SS-OCT system could be divided into four sub-systems: an imaging sub-system, an analog-digital interfacing (ADI) sub-system, a data processing sub-system, and a graphic user interface as illustrated in Figure 2-1. The imaging sub-system is a LCI with a raster-scanning sample arm optics. There are at least two devices in the imaging sub-system that need to be interfaced with the ADI sub-system: the ADI sub-system oversees the operation of both the

mirror scanner and the DAQ board. During the operation, the digitized data stream is first parsed by the ADI sub-system and later transferred to the data processing sub-system, where the data is further post-processed for storage or visualizations. The entire process is interfaced with the users through a graphic user interface (GUI).

The objective here is to implement a real-time SS-OCT system. Before starting to build the system, I have to bear one thing in my mind: the SS-OCT is very fast and it is producing tremendous amount of data every single second. Therefore, some advanced technologies such as RAID-0, graphic processing unit (GPU) computing, and multithreading will be implemented in this system to ensure the smooth running of the application.

2.1 The GUI

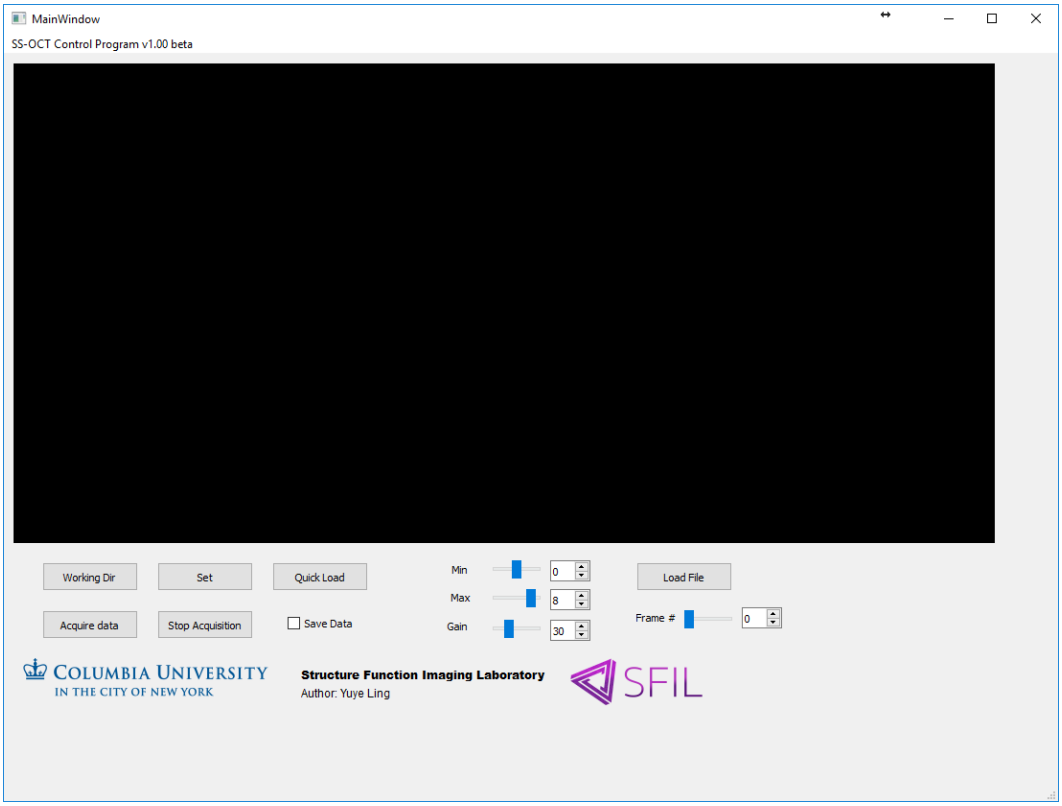

Figure 2-2 The GUI for the SS-OCT system.

As one of the most important elements of the system, the GUI solely determines the user experience. The proposed GUI could be segmented into the following panels as illustrated in Figure 2-2,

1. OCT system setting

2. OCT image display

3. File input/output handling

4. System status monitoring

I choose Qt (The Qt Company, Finland) as the application framework to design the GUI and handle its interaction with other sub-systems. Qt is a very popular framework used in GUI development. It is object-oriented and based on C++. Compared with the other potential candidate, Microsoft .NET Framework, it has the advantage of light weight and cross-platform supportability. Unlike .NET, Qt support literally all the operating systems ranging from Linux to Windows.

In the following sections, I will discuss how the application is organized in Qt and the main techniques we have used to facilitate the real-time human-machine interaction.

2.1.1 Multithreading

Most applications I have developed before are based on single-threading. Within each application (i.e. process), only one thread is launched. Therefore, the progression of the application has to be sequential. An exemplary sequential diagram of how the software part of the SS-OCT could be implemented in a single threaded program is provided in Figure 2-3(a). The program starts with the GUI operations, which include setting up the hardware such as microelectromechanical systems (MEMS) mirror and DAQ board. Once the preparations are done, the user could start the

data acquisition. The post-processing on the data will not be initiated unless a pre-defined size of buffer is acquired. Immediately after the post-processing, the reconstructed image will be posted and ready for visualization. The control of the process is then returned to the GUI. During the period that the control is under other working tasks, the GUI is non-responsive and can appear to freeze.

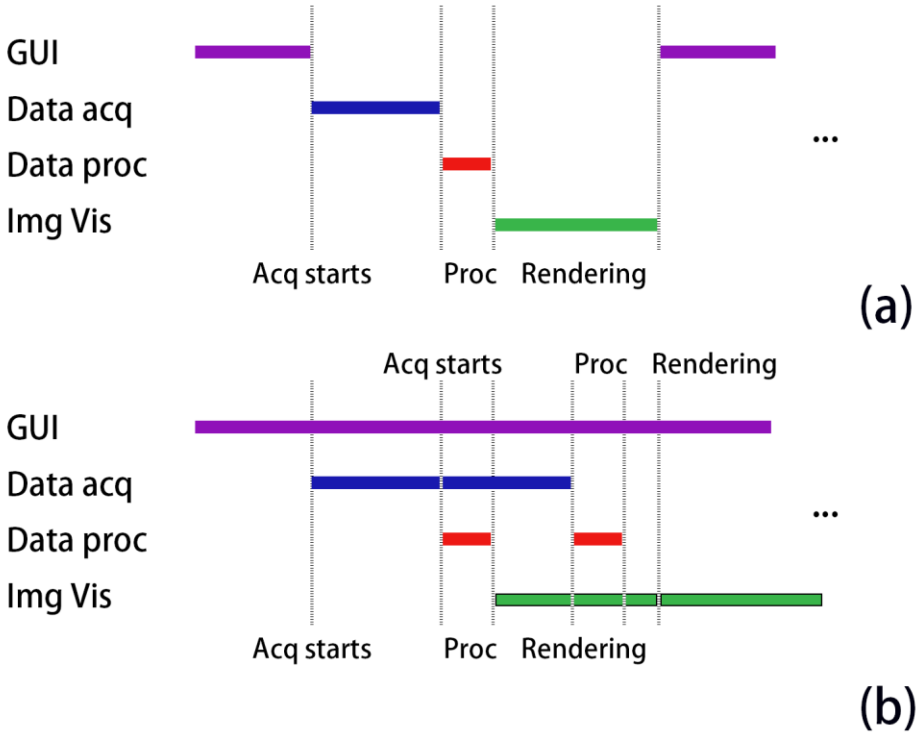

Figure 2-3 The sequence diagram for the entire SS-OCT software with (a) single thread, (b) multithread.

The sequential procedure does not fully utilize the throughput of the system and could lead to congestion when the data rate is too high. For example, a hold placed on the data acquisition stream during the data processing and imaging rendering could lead to an overflow in the DAQ board. Fortunately, the process could be parallelized, since each task actually uses different devices and resources: GUI monitors the inputs from the keyboard and mouse, data acquisition occupies

the data bus between the Peripheral Component Interconnect Express (PCI-Express) and memory, the data process consumes the CPU power, and the image rendering solely relies on the GPU.

A modified sequence diagram which utilizes simple parallelism is illustrated in Figure 2-3(b). In this new scheme, for example, the second data buffer could be acquired, while the first data buffer undergoes post-processing. This scheme is implemented by using multithreading and the inter-thread communication is conducted through a special mechanism provided by Qt called "signal and slot" as illustrated in Figure 2-4.

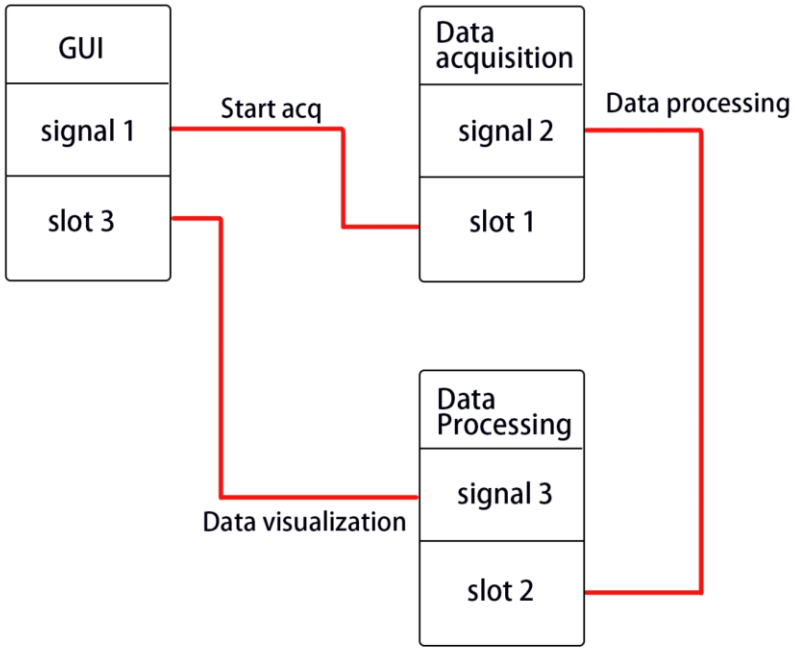

Figure 2-4 The multi-threading implementation of the application. Signal 1 will be emitted once the "acquisition" button is pressed in the GUI. Once slot 1, which is connected with the signal 1, receive the signal, the host thread "Data acquisition" will start. After the data stream fills one buffer, signal 2 will be emitted to notify the slot 2 that the data is ready and could be sent for post processing. Finally, the processed data will be transferred back to the GUI via "signal 3-to-slot 3" connection for final visualization.

2.1.2 Signal and slot

The “signal and slot” is a Qt version “callback”: a signal is emitted when a specific event occurs and is connected to a slot that will respond by performing certain tasks. For example, when the data acquisition for the first data is finished, a signal will be emitted to the connected slot, which is the data processing build in this case, will get notified. A new thread will be initiated and designated to the data processing. However, unlike that in the sequential mode, the original data acquisition thread will not be halted. It will move on to the next buffer right after emitting the signal.

In addition to the improvement on the performance, the adoption of multi-threading also enhances the user experience. The new GUI could now manifest asynchronous responses to events: one thread is now dedicated to the monitoring of the user’s actions, while the other threads are designated to different tasks as listed above.

2.2 Analog-digital interfacing sub-system

After describing the GUI, we move onto the next building block of the system, ADI sub-system. The main functionality of the ADI sub-system is to bridge the gap between the host computer and the underlying hardware (image sub-system). In the imaging sub-system, there are two devices need attention: the 2D MEMS mirror and the DAQ board. The control of the 2D MEMS mirror is straightforward and an open-loop control scheme is sufficient: the coordinates of the desired trajectory of the mirror scanning are encoded and sent to the device via a manufacturer provided driver API. On the other hand, the configuration of the DAQ board is more complicated as will be discussed in the following section.

2.2.1 Data acquisition

As I pointed out at the beginning of the chapter, the objective of this project is to implement a *real-time* OCT imaging system. To achieve this, we must be able to acquire the data in real-time, which turns out to be completely non-trivial.

2.2.1.1 Acquisition throughputs

A common misconception circulated among developers is that the data transfer rate of a bus is guaranteed. For example, a DAQ board that is connected to a host computer via PCIe 3.0 ×8 port should support a data rate close to its specification, i.e. 6.8 GB/s. But in reality, the effective data transfer rate is not even close to this value in most cases.

The biggest reason is that the operating systems (OS) including Windows and Linux that are not *real-time*. The scheduling of the response to an event is at the hand of the OS, which might lead to a significant delay. By bypassing the CPU and directly manipulate the memory unit, we could apply direct memory access (DMA) technique to alleviate the situation to some extent. However, the re-arming process after each DMA will still need CPU's attention and drag down the overall performance.

Additionally, most digitizers in the market are now using single-port memory as a buffer to temporarily store the digitized data before it is transferred to the host [63]. Single-port memory only supports one type of operation at a time: either reading or writing could be performed.

To address these two issues, I selected ATS9373 (AlazarTech, Québec, Canada) for proposed SS-OCT. It is equipped with a dual-port memory to handle the concurrent acquisition and transferring, which effectively serves as a very deep first-in-first-out (FIFO) buffer. The DAQ board also adopts a proprietary technique called Asynchronous DMA, which uses hardware

circuitry rearming without software intervention. I showed a bandwidth benchmark result in Figure 2-5. The average transfer rate was measured 6.3 GB/s, which is very close to the specifications.

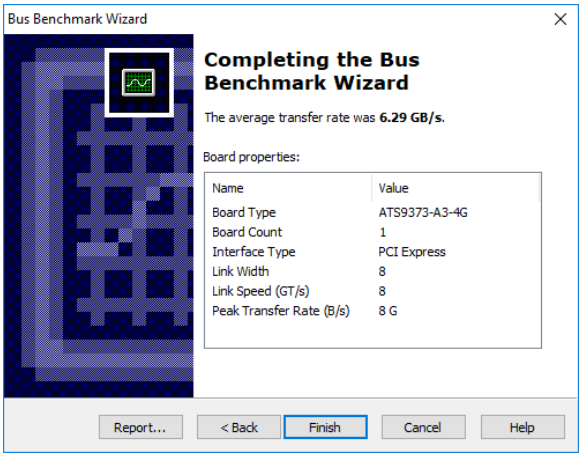

Figure 2-5 The data throughput of the DAQ board used in the proposed system.

The average transfer rate listed above is only applicable to the data transfer between the DAQ board and the memory in the host computer. I could get a different result, which is often much lower, if I further save the data to the hard disk (HD).

2.2.1.2 Memory layout in host computer

A special memory layout is designed to accommodate the concurrent acquisition and processing of multiple data streams. Two buffer arrays (or more) are allocated in the host memory before the acquisition. Once the acquisition starts, the first buffer receives the data from the current stream. After the first buffer is filled, the data stream will be directed to the other buffer, while data of the first buffer could be posted and ready for processing. This model matches very well with the multi-threading scheme introduced before.

2.3 Data processing, storage, and visualization

After having acquired gigabytes of data in the computer memory, I then need to process them to reconstruct the images. There are three main challenges:

(1) How to reconstruct the image? This is a computational problem.

(2) How to save the data? This is a hardware and file input/output problem.

(3) How to display the image? This a device input/output problem.

2.3.1 GPU computing

The first challenge is also the most difficult one. If we recall the Figure 1-3, which describes the procedure of the data processing in OCT, at least three FFTs (two from the Hilbert transform) have to be performed to reconstruct a single A-line.

Fortunately, the recent breakthroughs in GPU computing could rescue us. The computational power offered by the off-the-shelf GPU is enormous nowadays. As opposed to CPU, GPU does not have the complicated logic controller, which significantly simplifies its structure and thus enables massive integration of computational units. For example, 5,120 cores are integrated in a single NVIDA Tesla V100 GPU Accelerator, while at most 18 cores could be integrated in a single CPU (Intel i9-7980XE).

Instead of developing our own FFT algorithms from scratch, I took advantage of the existing `cuFFT` library (v7.5), which is an NVIDIA CUDA library to efficiently compute Fast Fourier Transform (FFT) [64], to achieve the best performance. Furthermore, I maximized the system performance with different optimization and profiling techniques, including memory coalescing, concurrent transfer and computation, tiling, and block/thread optimization.

In the current version of my software suite, a down-sampling factor of 10 is used and only a portion of the acquired data is fed to the *real-time* processing engine. This is due to the limited computing power provided by the GPU (Quadro K600 GPU, NVIDIA, USA) deployed in our host computer, which is a relatively old model with 192 CUDA cores and 1 GB DDR3 on-board memory [65]. In the future, it is possible to implement the full *real-time* processing later with an upgraded GPU.

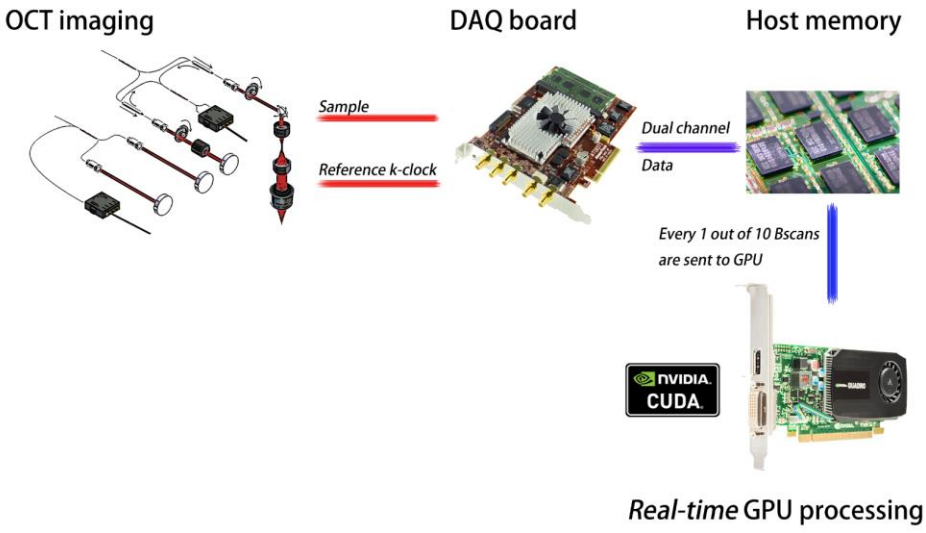

Figure 2-6 An illustrative block diagram for GPU data processing. Two channels of analog signals are digitized by a DAQ board and later transferred to the host memory at the full speed. After that, one every ten B-scans will be sent to the GPU for *real-time* processing.

A system-level block diagram is shown in Figure 2-6. The digitized dual-channel signals, including a clock channel and a data channel, are streamed to the memory in the host computer. The data is then decimated and transferred to the GPU to perform the CUDA post-processing before its being sent back to the memory. The processed data will then be displayed by screen. A detailed discussion on the implementation will be covered later in Chapter 4.

2.3.2 File input/output

The file I/O is handled by standard C++ input/output stream. A redundant array of independent disks (RAID) 0 is formed by using two Samsung SSDs to maximize the throughput of the file I/O.

2.3.3 Image visualization

The image visualization is implemented by using the Qt OpenGL module.

2.4 Trigger configuration

In previous three sections (section 2.1 to section 2.3), I have cover the software part of the system. In this final section, I will discuss the electrical configuration of the trigger signals, which is indicated by red solid arrows in Figure 2-1, that are essential in the OCT operations.

2.4.1 A-line trigger

There are two trigger signals in volumetric OCT imaging. The first one is the A-line trigger. Ideally, the A-line data acquisition should be synchronized with the start of wavelength sweeping, so that the timing jitter could be removed. Meanwhile, the MEMS mirror rotation should also be synchronized with the wavelength sweeping to eliminate the motion artifacts. Therefore, the output A-line trigger from the light source is split into two branches. One branch is connected to the "TRIG IN" port of the DAQ board. By configuration the device driver, I start the acquisition right after a rising edge is received from the "TRIG IN". The other branch is connected to the Port 2.6 (The details information about this connection could only be found in the exemplary demo codes "MTIDemo.cpp" (ln. 62)) of the NI DAQ board to trigger the motion of the MEMS mirror.

2.4.2 Frame trigger

An addition frame trigger is required to synchronize the raster scanning of the mirror with the data acquisition, so that each A-line could be well aligned in C-scan direction. In the proposed system,

I programmed the NI DAQ board, which is connected with the MEMS mirror, to output a digital trigger signal and synchronize the DAQ board with it. The M channel (digital output of the NI DAQ board) is set to 1 at the end of each frame (B-scan), while it is maintained at 0 for the rest of the time. By doing so, a transistor–transistor logic (TTL) pulse is effectively generated at the output of Port 0.0. By connecting this port to the "AUX I/O" and setting the AUX I/O port accordingly, I configure the DAQ board such that a new frame (B-scan) acquisition will not start until a frame trigger is received.

2.5 Summary

In this chapter, I have discussed the objective of the system development and top-level design of the system. Without diving into the technical details of the implementation, I explained how the four sub-systems are interconnected at both hardware and software levels. Some basic considerations on the performance are given to justify the choice of some specific software and devices. In the next chapter, I will start the discussion on the corner stone of the entire SS-OCT system: the optical imaging sub-system.

Chapter 3 Optical system design

The optical system is truly the heart of an SS-OCT system, without which no images could be formed. The proposed optical arrangement of a benchtop SS-OCT is illustrated in Figure 3-1, and the arrangement could be divided into two parts: OCT imaging engine and a reference *k*-clock.

The OCT imaging engine is based on a LCI. The main output of a wavelength swept laser source (KSS20001310B00, NTT-AT, Japan or HSL-20, Santec, Japan) is split into two branches: one sample arm (90%) and one reference arm (10%). In the sample arm, a 4-quadrant MEMS mirror (A1S1.x, 1.7 mm integrated mirror, Mirroracle Technologies, USA) was paired with a scan lens (LSM03, Thorlabs, USA) to raster scan the laser beam over the sample. Two pairs of achromatic doublets, each pair of which forms a Plössl type eyepiece, were used as a beam expander to optimize the lateral resolution. In the reference arm, we added a dispersion compensator (LSM03DC, Thorlabs, USA) to balance the dispersion between the two arms. The back scattered light from both arms was collected, directed by two fiber optic circulators (CIR-1310-50-APC, Thorlabs, USA), and recombined in a fiber optic coupler (TW1300R5A2, Thorlabs, USA). The optically mixed outputs were detected by a high-speed balanced photodetector (PDB480C-AC, Thorlabs, USA).

The reference *k*-clock, on the other hand, is a Michelson interferometer with fixed OPL difference. Generally, it could be implemented by any interferometer, such as a Mach-Zehnder interferometer, as long as the same light source from the OCT imaging engine is used as the input and the spectral interferogram is recorded simultaneously. In fact, when the Santec light source is in use, a compact fiber-based MZI (INT-MZI-1300, Thorlabs, USA) is used to ensure the best performance.

In this chapter, I will only focus on the sample arm optics within the OCT imaging engine. The objective is to design an OCT imaging system, whose

1. axial and lateral resolution is between 10~15 μm,

2. FOV is larger than 4 mm with flat image surface

3. A modest depth of focus of ~500 μm

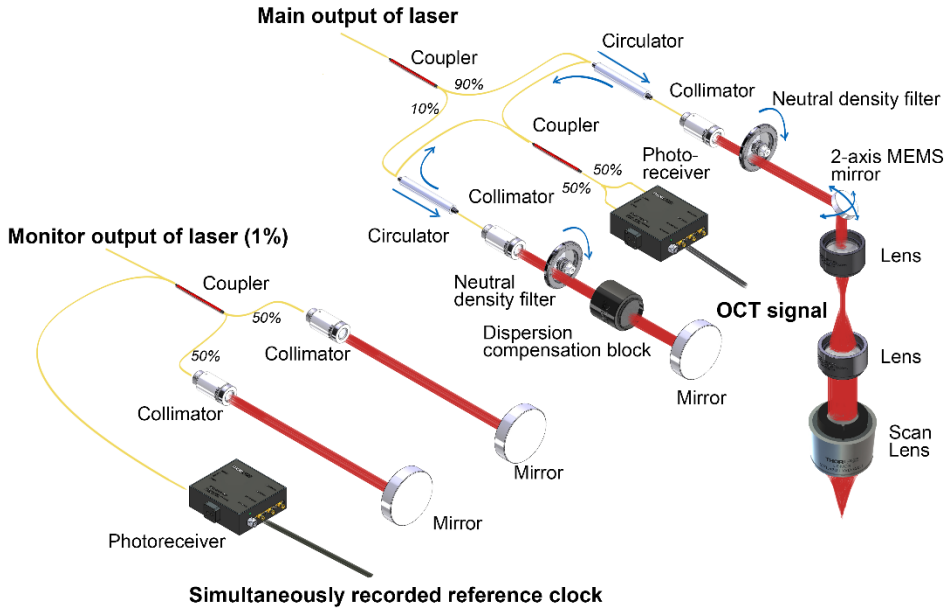

Figure 3-1 The schematic of the proposed highly phase-stable high-speed SS-OCT. The entire system could be divided into two sub-systems: an OCT imaging engine, and a simultaneously recorded *k*-reference clock.

3.1 Sample arm

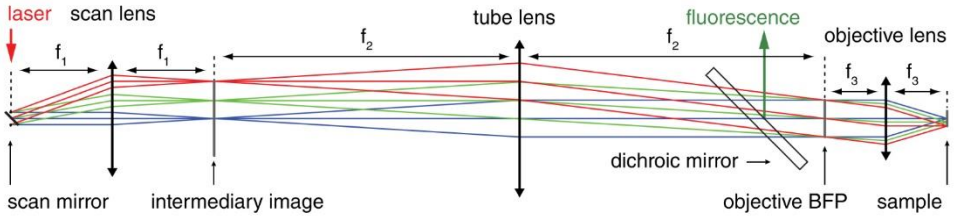

Figure 3-2 Ideal layout of a 1D laser scanning microscope. Scanning is achieved by placing the scan mirror's rotation axis at the focal plane of the scan lens. The scan lens together with the tube lens form an afocal telescope system that projects an expanded image of the laser beam from the galvanometric mirror onto the objective pupil (or back-focal plane) that only pivots within the objective pupil without any lateral shift. As the focused spot moves across the sample, it generates fluorescence which is collected by the objective and in the case of twophoton laser scanning microscopy, directed on to one or more detectors by a dichroic mirror placed between the tube lens and objective. [Adapted] with permission from ref [66], [OSA].

A typical OCT sample arm optics could be similar to that of a scanning microscopy, since both systems are intended to raster scan a laser beam on a flat surface. An exemplary arrangement of laser scanning microscopy is illustrated in Figure 3-2. The arrangement consists of three lenses and a scan mirror. The scan mirror is placed at the front focal plane of the scan lens, while the scan lens along with the tube lens makes up an afocal telescope. The afocal telescope forms an image of the original laser beam at the back focal plane of the tube lens with scaled beam diameter and inversely scaled scanning angle. The scaling factor is determined by the ratio of the focal length between the tube lens and the scan lens. The back focal plane of the tube lens further coincides with the front focal plane of the objective lens to form a telecentric telescope: the angular scanning of the laser beam at the front focal plane of the objective lens could be translated to lateral scanning at the back focal plane.

The quality of the optical design of the sample arm optics directly determines the image quality of OCT including the lateral resolution, the field-of-view (FOV), image quality (aberration), and signal-to-noise ratio (SNR) among others. The design of OCT sample arm features several unique challenges.

First of all, a telecentric optics is very attractive in 2D or 3D laser scanning system. A telecentric optical system possesses the benefits of having a flat image plane, a constant magnification, and a constant spot size even off axis [67]. However, it is not trivial to assemble a true two-dimensional telecentric optics by using conventional galvanometer-based scanners, where the *x*-and *y*- axis scanning head are separated. Although it is possible to just insert a relay optics between the scanning mirror [68], other interesting strategies have been proposed as well. Zawadzki *et al.* designed an adaptive optics based sample arm to reduce the aberration [69]. Hu *et al.* suggested that a quasi-telecentric optical system could be implemented with a compact *x*-*y* galvanometer scan head to obtain a satisfactory imaging quality over a large FOV [70]. Recently, with the development in MEMS technology, it is possible now to fabricate a MEMS mirror that is capable of rotating against two axes at high speed [71, 72]. We adopted this new technology in our design and used 2 axis MEMS mirror in our SS-OCT system.

However, even if the scan mirror is now placed at the front focal plane of the scan lens, the benefits of forming a telecentric optics could only be reaped if the mirror is scanning at a small angle. When the scan angle increases, the lateral displacement after the objective can no longer approximated to be linear to the angle unless an f-theta lens is used. Off-axis related aberrations will also emerge [73].

Moreover, the broadband emission spectrum of the light source in OCT system must be taken into consideration during the optical design, especially when off-the-shelf optical components are used to develop the system. Achromatic aberration and astigmatism could significantly reduce the quality of the resulted image. A simple remedy without getting into the hassles of designing a custom lens could be forming a Plössl type of scan lens and tube lens by putting two achromatic doublets back to back [66].

Last but not the least, the mirror size needs to be carefully picked. A smaller mirror is usually preferred in SS-OCT in order to achieve a high scan rate, since a smaller size usually leads to a smaller inertia and a higher resonance frequency. However, a smaller mirror, which highly possibly be an aperture stop in the system, in turn requires a higher magnification of the relay optics in to fill the entrance pupil of the objective to ensure a high lateral resolution, which will not only make the system bulky but also introduce more aberrations.

3.1.1 Sample arm design and simulation

Bearing these in mind, I designed an OCT sample arm optics, and it is illustrated in Figure 3-3. The broadband laser light is first collimated by a collimation package (F220APC-1310, Thorlabs, USA) before being deflected by the 2-axis MEMS mirror. The output beam diameter of the collimation package is 2.04 mm.

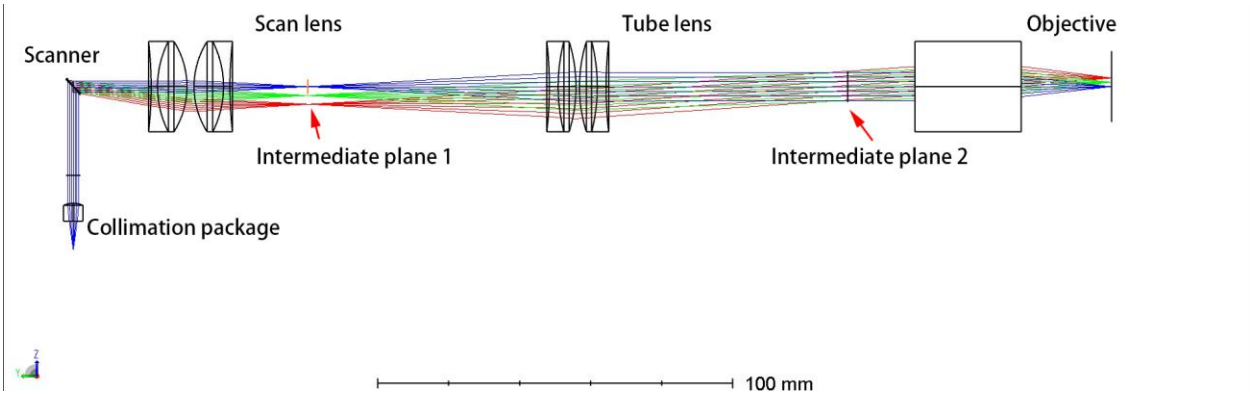

Figure 3-3 The optical design of the OCT sample and the configuration for the computer simulation in OpticStudio (version 14.2 SP3, Zemax, USA). The incident light is first collimated by a collimation package before being deflected by a MEMS scanner. The beam is then expanded by an afocal telescope. It is finally focused by an objective lens.

After that, the deflected beam is expanded by the afocal telescope, and the image of the pivot point of the MEMS mirror is formed on an intermediate plane. The afocal telescope is comprised of two pairs of achromatic doublets (AC254-060-C and AC254-150-C, Thorlabs, USA), each of which forms a Plössl. The effective focal length of the Plössl is 21.93 mm and 68.07 mm, respectively, and the magnification is approximately 3 times. The main purpose of this expansion is to enlarge the beam diameter to match the entrance pupil of the objective lens (LSM03, Thorlabs, USA). On the other hand, it also helps enlarge the space between the MEMS mirror and the objective lens, and make inserting a folding mirror to rotate the optical axis possible. The objective lens is then placed so that the intermediate plane, where the image of the pivot point of the MEMS mirror locates, coincides with the back focal plane of the scan lens. Therefore, whenever the MEMS mirror rotates around its pivot point, the angle of the incident beam into the entrance pupil of the scan lens will follow accordingly. This rotation will be translated to lateral scanning on the surface of the sample.

3.1.1.1 Zemax simulation

Before assembling the system, I first simulated the proposed optics in OpticStudio (v14.2 SP3 Professional, Zemax, USA). Because of the broad emission bandwidth of the OCT light source, which is often not fully covered by off-the-shelf optical components, a thorough computer simulation could help fine tune the optical system's parameters and evaluate the exact performance.

The telecentric optics possess one very important property: the chief ray is perpendicular to the image plane. This is also the reason why the image magnification of the system is constant. In OpticStudio, I thus took advantage of this property to construct the metric function and conduct the optimization to find the best system geometry. Parameters such as the separation between two achromatic lenses that form a Plössl, the separation between the tube lens and the scan lens, the etc. are all set as variables. In addition to confining the chief ray angle in the image plane, I also imposed a restraint on the chief ray angle in the intermediate plane 1 by using operand "RANG". A global optimization was then performed by using dampest least squares.

After optimization, the system performance is evaluated by various means. I first analyzed the spot diagram as shown in Figure 3-4. The first row gives the on-axis spot diagrams at different defocus positions with the Airy disk presented as a black circle. The overall on-axis performance is very good with no chromatic aberration. As the field angle (deflection angle from the MEMS mirror) increases, both chromatic aberration and astigmatism are introduced: the shorter wavelength of light is focused a little bit closer to the axis, while the tangential focus falls shorter than the sagittal focus. As to the resolution, almost all nine spot diagrams falls within the range of Airy disk. The inferred depth of focus also matches with the specified Rayleigh range of the objective.

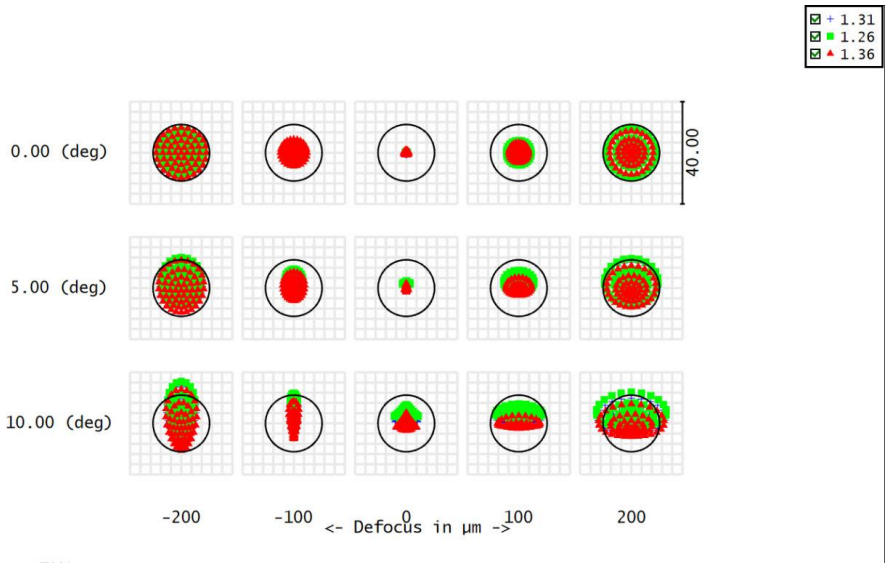

Figure 3-4 Spot diagram of the sample arm optics at different planes (columns) including the focal plane (middle column) obtained in OpticStudio. The first row shows the on-axis results, while the second and the third row gives the results when the mirror is rotated by 5 °and 10 °, respectively.

Since there is astigmatism at larger angles, I then analyze the flatness of the imaging plane and the field curvature. The result of the field curvature is presented in Figure 3-5(a). The overall flatness is very good over most of the FOV; the distance between the tangential focus and sagittal focus is less than 100 μm at an angle up to ~8 °. The T-Theta distortion versus deflecting angles is shown in Figure 3-5(b). The maximum of the distortion is below 2% at the maximum angle (10 °), which showcases an almost linear relationship between the rotating angle and the lateral translation of the light spot.

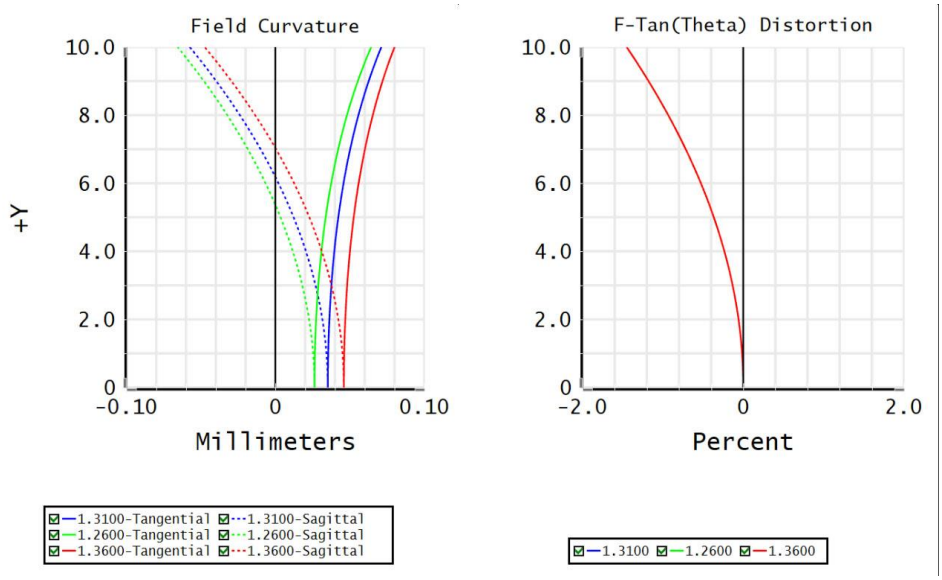

Figure 3-5 (a) The field curvature and (b) the F-Theta distortion of the sample arm optics at different incident angles. The solid curves in different colors in (a) represent for the tangential focus of different wavelength, while the dashed curves coded in different colors stand for their sagittal counterparts.

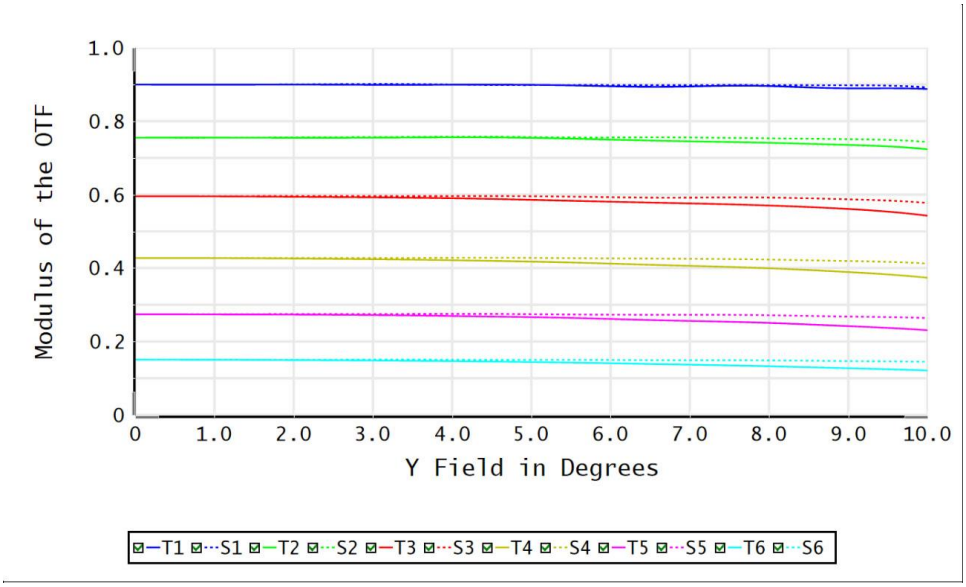

Figure 3-6 The optical transfer function of the sample arm optics at different incident angle. Blue, green, red, yellow, purple and cyan represent 10 cycle/mm, 20 cycle/mm, 30 cycle/mm, 40 cycle/mm, and 50 cycle/mm, respectively. The solid lines show the tangential results and the dashed lines give the sagittal ones.

In the last part, I examine the modulus transfer function (MTF) of the system at different field angle, which is provided in Figure 3-6. The MTF is generally flat over the entire FOV at low spatial frequency (Freq 1: 10 cycle/mm). We then constructed the optical system based on the simulation, a picture of the actual sample arm optics is shown in Figure 3-7.

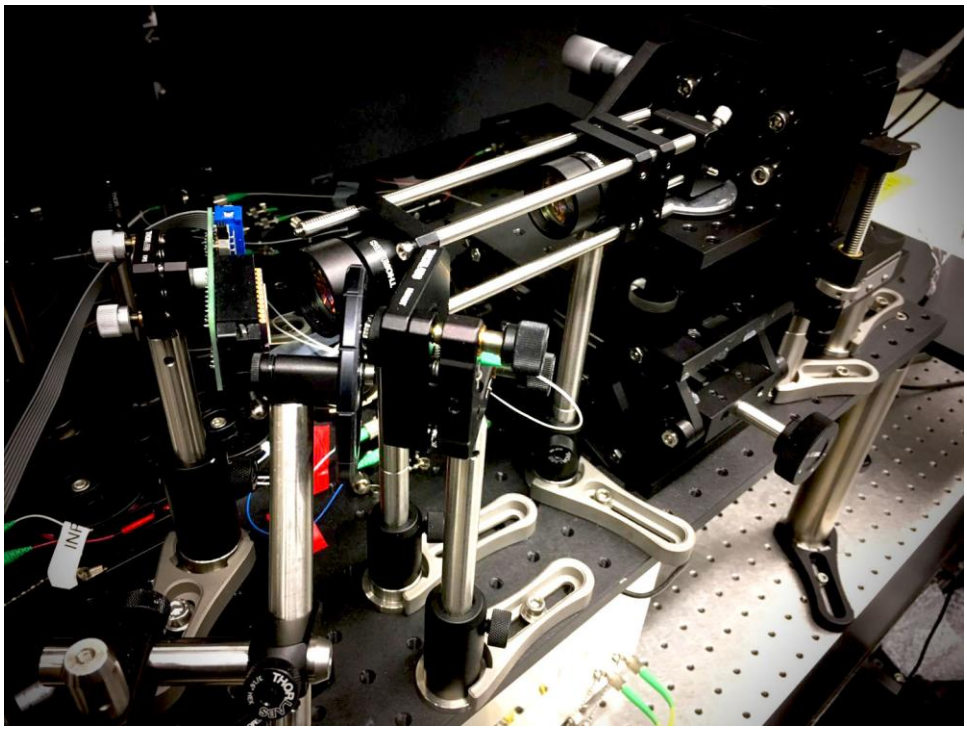

Figure 3-7 The actual optical assemble of OCT sample arm.

3.1.2 Experimental evaluation

A series of experiments are conducted to further validate and characterize the performance of the designed optical system. In this evaluation, only the NTT's light source is used. The axial resolution was measured to be 15.8 μm as the full width half maximum (FWHM) of the A-line profile as in Figure 3-8(a). In comparison, the theoretical axial resolution of 17.15 μm was calculated as $(2\ln 2/\pi)\cdot(\bar{\lambda}^2/\Delta\lambda)$. The lateral resolution was determined to be 16.5 μm (Group 6-1) in Figure 3-8(b). Considering that the NA of the objective is 0.08, the theoretical lateral

resolution was calculated as 12.10 μm, using $\delta x = 0.37 \cdot \bar{\lambda} / \mathrm{NA}$. The measured values are well agreed with the theoretical values.

Following the definition of SNR in OCT [74], we measured the SNR or sensitivity (as the minimum sample reflectivity that can be detected) to be 104.8 dB, as the sum of the difference of the DFT peak from the noise floor (24.8 dB) and the total attenuation in the sample arm (80 dB, OD = 4) with a silver mirror at the focal plane of the sample arm. In contrast, the theoretical prediction of the sensitivity is 109 dB.

For the SNR fall-off measurement, a silver mirror was placed at the focal plane of the sample arm, while the reference mirror was displaced by a linear translation stage. As shown in Figure 3-8(c), we observed a -18.44 dB fall-off at 2 mm.

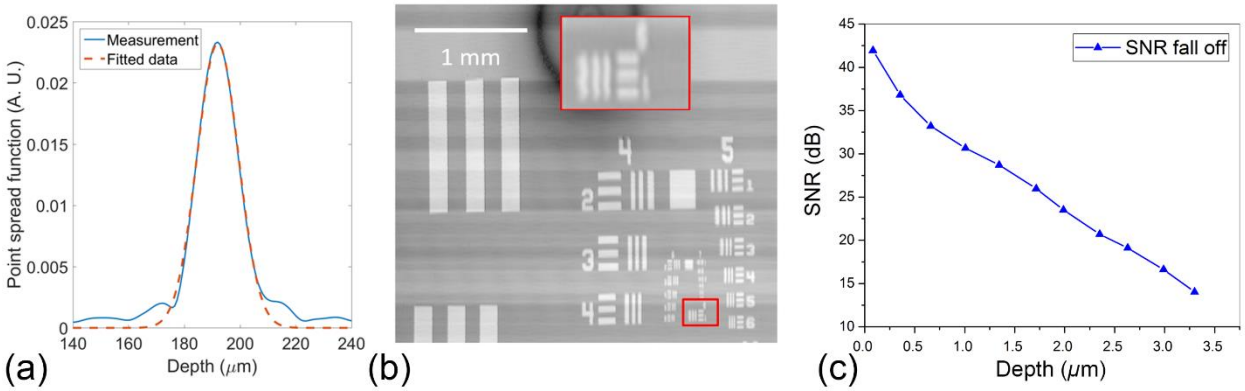

Figure 3-8 The standardized test for the OCT system. (a) The axial point spread function. (b) An en face image of resolution target. (c) The signal fall off plot of the system.

3.2 Discussions

3.2.1 System alignment

The optical arrangement of OCT sample arm is straightforward, if we compare it with other laser optics setups such as that in nonlinear optics. However, it still requires a huge effort and patience

to align the optics and to achieve the best performance. It is not uncommon for me to sit beside the bench for five hours just to re-align the optics after switching one achromatic lens in the beginning. After playing with optics for in the past couple years, I do have some experience on aligning optics to share with the readers.

One thing that makes the alignment difficult is that the light is invisible: the proposed system is operated at 1300 nm which is NIR. Although it is possible to use laser viewing card or fluorescence alignment disk to aid the process, it is still very cumbersome. In comparison, a better practice will be simply adding a visible aiming laser to the system, which could greatly speed up the prototyping.

It is also a good practice to use lens tube or cage system to assemble the optical components. This will not only automatically align the optics, but could also effectively improve the imaging quality since most stray lights will be blocked by the tube.

It is crucial to screw down everything in the optical system at all time: every screw in the system has to be fixed. Even a single loose screw on the lens mount will possibly reduce the phase stability by a large amount. It is equally important to tape down all the fibers (if there is any). Lose fibers will introduce random phase walk to the system and randomly change the polarization state of the system, both of which will degrade the imaging quality of the system.

Last but not the least, we have to consider the aperture of the system. There are three sets of MEMS mirrors provided by the manufacturer and their diameter is 4.2 mm, 1.7 mm, 1.2 mm, respectively. Depending on the application, the mirror could be interchanged. In most cases, however, the MEMS mirror functions as an aperture in this system. If the incident beam diameter is not matched

by the size of the MEMS mirror, apodization will occur and a low-pass filtering effect will be taken place in the image.

3.2.2 Discussion on SNR measurement

The definition of the SNR in FD-OCT is contradictory in literatures. Initially I measured the SNR (82.5 dB) following the procedures described in [26], but we may underestimate the minimum reflectivity that can be detected because the reference arm power was not optimized. Following the definition of SNR in OCT [74], we re-measured the SNR or sensitivity (as the minimum sample reflectivity that can be detected) to be 104.8 dB, as the sum of the difference of the DFT peak from the noise floor (24.8 dB) and the total attenuation in the sample arm (80 dB, OD = 4) with a silver mirror as a reflector.

The theoretical SNR under shot-noise limit is then calculated by using the maximum power returned from the sample arm to the detector (3.05 mW) as [74],

$$SNR = 10 \times \log_{10}\left(\frac{\eta P_{sample} \tau_i}{h\nu_0}\right) = 10 \times \log_{10}\left(\frac{0.8 \times 3.05 \times 10^{-3} \times 1/200000}{6.626 \times 10^{-34} \times 3 \times 10^{8}/(1320 \times 10^{-9})}\right) \approx 109\text{dB} \qquad (3.1)$$

The difference of ~-4 dB between the measured SNR and theoretical prediction might be caused by the relative intensity noise of the light source, unaccounted coupling efficiency of the system, and non-optimal reference power.

This concludes the Chapter 3. In the next chapter, we will move on to discuss the software part of the system.

Chapter 4 Software development for SS-OCT system

Although the implementation of the OCT imaging engine is of fundamental importance, the corresponding software development is also essential in order to make up a good OCT system: a versatile, user-friendly OCT control program could grant the user with more capability of performing imaging task quickly and effectively.

Here, I would like to first present the package I have developed, and the GUI is shown in Figure 2-2. In the following chapter, I will discuss the details on how I implement the package.

4.1 Objectives

The SS-OCT is a complex system as we have discussed previously at the beginning of Chapter 2 and illustrated in Figure. 2-1. As to the software package, a desired one should include following componets,

1. a graphic user interface (GUI) that allows the users to easily configure the system and evaluate the images,

2. full control over the MEMS mirror and the DAQ board,

3. a memory layout and file input/output (I/O) that could handle the digitalized signal stream,

4. a data processing routine that could reconstruct the image from raw data steam in real-time,

5. a visualization program renders the image to the user, also in real-time.

The main challenge of this project stems from the enormous data size I am confronted: the data rate of the system when being operated in a dual-channel mode could be easily surpassing 3 GB/s, and a 10 seconds recording will end up with a binary file as large as 36 GB. In order to implement the *real-time* visualization, GPU programming is used to boost the computation speed. Various levels of parallelisms existed in the conventional OCT algorithm has been exploited and a speed improvement in a factor of ~1000 is achieved.

The entire program is written in C/C++ to ensure the maximal compatibility and portability. The data acquisition, post processing, and visualization part are 64-bit programs, while the mirror control is a separate program compiled in 32-bit. The compilation is done in Microsoft Visual Studio Professional 2013. The GPU programing part is based on NVIDIA CUDA 7.5, and the GUI is designed by Qt 5.6.

4.2 Device drivers

Before I start describing the more exciting part of the chapter such as parallel programming, I would like to first review how I managed to resume the full control over the hardware including the MEMS mirror and the DAQ board.

4.2.1 Mirror control

Unlike the conventional galvanometer-based scanner, which is driven by a pure analog waveform, the new generation MEMS-based scanner could be viewed as a digital device. One of the most interesting features of these MEMS mirror is that they could be opted into a so-called “discrete scan mode”, in which the mirror only actions whenever a trigger signal is received and the magnitude of the movement (rotation) is dictated by an input digital value. This operating mechanism offers a huge advantage: an arbitrary scanning pattern, which is a series of coordinates,

could be easily generated by a computer and immediately sent to the device. For example, it is much easier for us to program the MEMS scanner to operate in a “move-hold-move” mode, which is commonly used in phase-resolved OCT.

4.2.1.1 Device initialization

Once the MEMS mirror is correctly connected and powered on, I first initialize the device and make it visible to the control program. A device handle is first created by calling function `MTICreateDevice`, and the device is then initialized by calling function `MTIInitializeDevice`.

4.2.1.2 Parameter initialization

After initializing the device, I could directly get access to the device’s registers through the MTI API. In order to operate the scanner properly, some of the registers has to be reset. Among all those parameters, there are two sets are of the most importance: the *vMax*, which determines the maximum voltage could be applied on to the mirror, and the *filterBW*, which gives the cutoff frequency of the hardware filter integrated on the device. I set these two parameters to the exact values given in the device datasheet, otherwise the device could be damaged if it is driven too hard (higher *vMax* than the recommended value) or too fast (higher *filterBW* than the recommended value).

For the raster scanning of the laser beam, one parameter that needs to be specified beforehand is the FOV. MTI API provided a useful function `MTISetAmplitude`, in which the input amplitude is linear to the deflecting angle of the MEMS mirror. *Amplitude*, *vMax*, and the yet to be introduced *scaling* will collectively determine the exact scanning range of the device.

4.2.1.3 Preparation for scan

Once the global variables are initialized, I start to reset the hardware and prepare the mirror for scanning. Depending on the termination status of the last scan, the mirror might not necessarily be located at the origin. `MTIResetDevicePosition` is called to make sure that the mirror starts its scan from the origin.

We could also specify whether we would like to synchronize the mirror scanning with the A-line acquisition by using `MTISetSampleClkSource` function. When the second argument of the function is set "*true*", the discrete mirror movement will only be triggered by the external clock, which is the A-line trigger from the light source in our case. Otherwise, the mirror scanning will be in "*free run*" mode: the mirror motion is triggered by an internal crystal oscillator, which is out of the synchronization with the A-line acquisition. After that, the high-power amplifier is switched on, and the mirror is ready to action.

4.2.1.4 Scan pattern generation

As we mentioned at the beginning of this section, the MEMS mirror is rotating according the received discrete coordinates. In another word, if I want to rotate the mirror linearly in y=0 plane, I could simply send the following discretized triangle function (vector) to the device,

$$x[i] = -1 + \frac{2i}{N} \tag{4.1}$$

where i is the index, and N is the total number of the sampling point in x direction. Once a trigger signal (either external or internal) is detected, the next value in the vector will be evaluated and the mirror will be actuated to the corresponding position. The device could also scan against two axes simultaneously, so long as a pair of two coordinates is sent.

However, it is worth noting that the motion of the mirror does not necessarily follow the exact input coordinates due to the mechanics involved. For example, if I use the aforementioned triangular waveform to drive the MEMS mirror, resonance could be excited if the scanning period is small and the mirror is driven in open loop. Therefore, I follow the suggestion by Cogliati *et al.* and use a pre-filtered digital signal to drive the mirror instead of just sending the raw triangle function to reduce the distortion and avoid the resonance [75]. A detailed discussion on the mechanical response of the galvanometer-based scanner and MEME scanner could be found in elsewhere [75, 76]. Currently, the pre-filtered scanning curve (coordinates) is calculated offline and later loaded. In the future, an online pre-filtering routine will be integrated into the scanning program.

4.2.1.5 Synchronization

For any raster scanning type imaging technique, synchronization is the key. As we have discussed before in section 2.4, there are two levels of synchronization between the scanner and the DAQ board in OCT: (1) A-line synchronization and (b) B-scan (frame) synchronization.

For A-line synchronization, the mirror will only move to the next coordinate when an A-line trigger is received from the wavelength swept light source. In contrary to the "*free run*" mode, in which the scanner acts according to an internal clock, the A-line synchronization eliminates the inter-A-line jitters.

As to the B-scan synchronization, the DAQ board is synchronized to a trigger emitted from the mirror scanner: the DAQ board will not start a new B-scan acquisition until the MEMS mirror has been moved to the starting location of a new B-scan, and a frame trigger is emitted from the MEMS scanner to the DAQ board. The B-scan synchronization ensures that each frame will be

well aligned against each other. Otherwise, it is not uncommon to observe wavy edges on a straight line in the *en face* image due to the imperfect B-scan synchronization.

While the A-line trigger is already provided by the light source, the B-scan trigger has to be generated by myself. I modulate the digital output port P0.0-P0.7 on the mirror control board by setting the value of *M* channel. In this case, I connected P0.7 with the "AUX I/O" port of the DAQ board, and set P0.7 to be TTL high whenever a B-scan is finished. In the meantime, the DAQ board is also configured accordingly, so that a new B-scan will not be initiated unless a "high" level is received at the "AUX I/O" port.

4.2.1.6 Start and stop scanning

Once all the data (coordinates) is prepared and connections are ready, I start sending those coordinates to the device's register by calling `MTISendDataStream`, which followed by a call of `MTIStartDataStream` to officially start the scanning.

After use, we have to follow the correct sequence to cool down the system. The detailed procedures could be found in the data sheet of the MEMS mirror.

4.2.1.7 The actual program and GUI for mirror control

The mirror control program we developed is shown in Figure 1-1. It is a stand-alone program built upon the basis of the 32-bit MTIDevice–C++ Software Development Kit (SDK) provided by Mirrorcle Technologies, Inc. (USA). Ideally, the mirror control program should be integrated as a part of the OCT software package. Unfortunately, Mirrorcle refused to provide me with a usable 64-bit driver and API, so that it could not be combined with the rest parts of the 64-bit OCT software package.

The program is currently encapsulated within a simple Windows Form application to facilitate the interaction between the user and the device. Most frequently used parameters such as *x* direction sampling points, *x* direction oversampling factor and etc. could now be specified before each scan. In the future, we would like to modify the program, so that an online pre-filtering of the driving curve could be implemented.

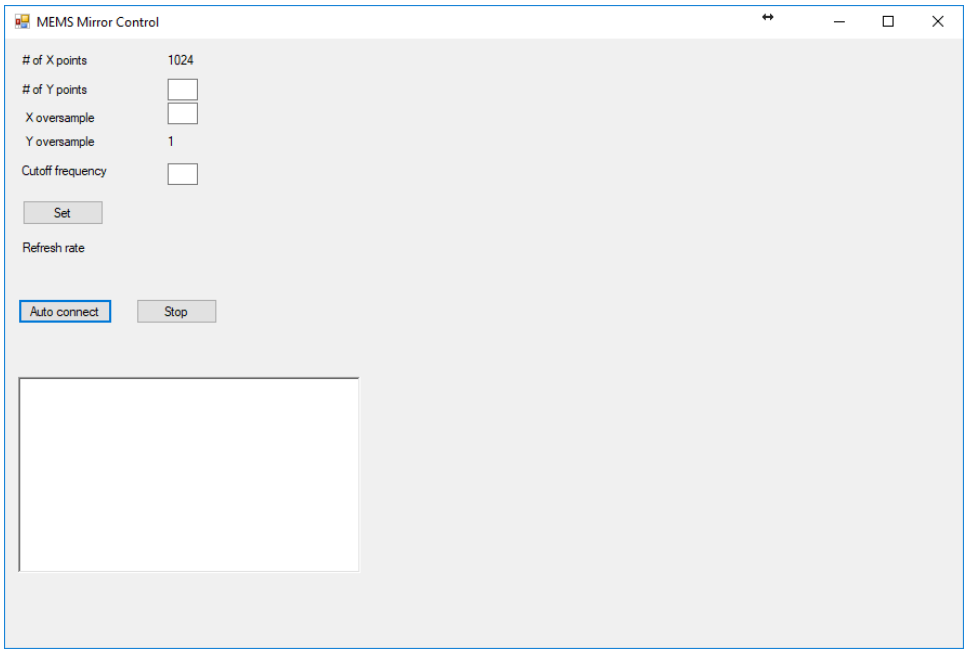

Figure 4-1 The current stand-alone MEMS mirror control program.

4.2.2 Data acquisition

The data acquisition routine is a key component of the software package. Due to the enormous data generated by the SS-OCT, successful handling, transferring, and recording the data all rely on a careful configuration of the DAQ board and design of the memory layout.

4.2.2.1 Data layout and parameter setting

I developed the data acquisition routine based on the ATS-SDK v.7.1.4 (AlazarTech, Canada). In ATS-SDK, the data acquisition is sliced into four levels: 1 acquisition includes *L* buffers, each

buffer consists of *M* records, and each record includes *N* samples (postTriggerSample1 in the program). This structure coincides with the data structure of OCT, in which we have C-scan, B-scan, A-line, and pixel, respectively. Before each data acquisition, I first identify the value for *L*, *M*, and *N*. *N* is collectively determined by the sampling rate of the DAQ board, the A-line rate of the light source, and the duty cycle of the wavelength scanning. In ATS-SDK, *N* must be an integer multiple of 128 due to a special requirement for data alignment. *M* gives how many A-lines are included in a signal B-scan (frame), and it should be equal to the number of sampling points used in *x*-direction mirror scanning. *L*, on the other hand, is mostly selected depending on the applications and is limited by the on-board buffer size as well as the data transmission bandwidth. Since the data throughput of a dual-channel OCT acquisition is much higher than the writing speed of current hard drive, a too large *L* (>1000) could overflow the allocated buffer.

The `AlazarSetRecordSize` function is used to set the postTriggerSamples1. `AlazarBeforeAsyncRead` is then called to configure the memory based on parameters including the channel number, *L*, *M*, and *N*. After that, the application calls `AlazarPostAsyncBuffer` to make the allocated buffers available to be filled by the board, and later calls `AlazarStartCapture` to start the acquisition.

4.2.2.2 Buffered data acquisition

Thanks to the proprietary software provided by AlazarTech, the ATS-9373 is capable of running in a so-called asynchronous AutoDMA mode. As I described back in section2.2.1, several buffers are allocated in the memory beforehand in this mode. Once a buffer is filled during the acquisition, an interrupt signal will be generated by the ATS-9373 and redirect the streaming to the next buffer. In the meantime, the filled buffer will be flagged as ready and the application could start processing

it. In this way, the CPU does not need to handle the data acquisition, which greatly enhance the data throughput. A schematic block diagram is provided to illustrate this process.

Once the acquisition starts, function `AlazarWaitAsyncBufferComplete` is called to wait for the board to receive sufficient trigger events to fill the buffers. Once the buffer is filled, the interrupt will notify the board, so that the data will be directed to the next available buffer. In the meantime, the CPU thread will start processing and transferring the filled buffer. After everything is finished, `AlazarPostAsyncBuffer` is called again to put the buffer back to the chain for next acquisition cycle.

4.3 Data processing by using GPU

In section 1.1.4, I have briefly introduced the SS-OCT data processing. In addition, the motivation of using parallel computing to accelerate the process is also discussed in section 2.3.1. In the following section, I will detail how I implement this on a NVIDIA GPU.

4.3.1 Parallel computing

There are two types of parallelism in parallel computing: data parallelism and task parallelism. Task parallelism is similar to the multithreading I have mentioned before (section 2.1.1) but is within a different domain. Data parallelism is also known as *Single instruction, multiple data* (SIMD), in which case that the same instruction is operated multiple times on different data in a device with multiple processing units. Compared with the conventional *Single instruction, single data* (SISD), SIMD not only saves the computing time but also reduces the memory accessing time, especially when each data is relatively small in size.

Real-time SS-OCT data processing as described in Section 1.1.4 and Section 2.3.1 is a perfect candidate for parallel computing. First of all, the SS-OCT data processing is per A-line

based and each A-line goes through exactly the same processing. Moreover, during the procedure, each A-line is independent from each other and there is no divergence in the control flow. Secondly, the data transferring between the host computer and the GPU could be parallelized with the data processing (on the GPU) to further speed up the program.

To implement the parallel computing, I will use the popular CUDA platform, which will be introduced in the next section.

4.3.2 CUDA basics

CUDA is a proprietary GPU programming model developed by NVIDIA, and it could be viewed as an extension based on the standard C/C++. The smallest unit to conduct computation in CUDA is *thread*. Multiple *threads* form a *thread block*, and multiple *thread blocks* forms a *grid.* On the other hand, the building block of the CUDA program is called *kernel.* Each *kernel* usually performs one task, and different *kernels* could be parallelized by being assigned to different *streams*.

The memory access in CUDA is also hierarchical. The memory space allocated in the host device (system memory in the PC) is not directly accessible to CUDA *kernels*, and an explicit transfer instruction (`cuMemcpy`) is required to move the data from the host memory to the GPU memory. Once the transfer is done, the data will be residing in the global memory by default. Global memory is usually slow in read/write operation. A shared memory could be allocated explicitly in CUDA during the variable declaration by inserting a prefix `__shaerd__` before the variable. Shared memory is orders of magnitude faster than the global memory, but it is scarce in amount. Moreover, shared memory is usually declared in a *kernel* and is only accessible within the *thread block*. The fastest vehicle is register. Register is very small (32k in size) and is only accessible within the *thread*. It is often used to save intermediate values.

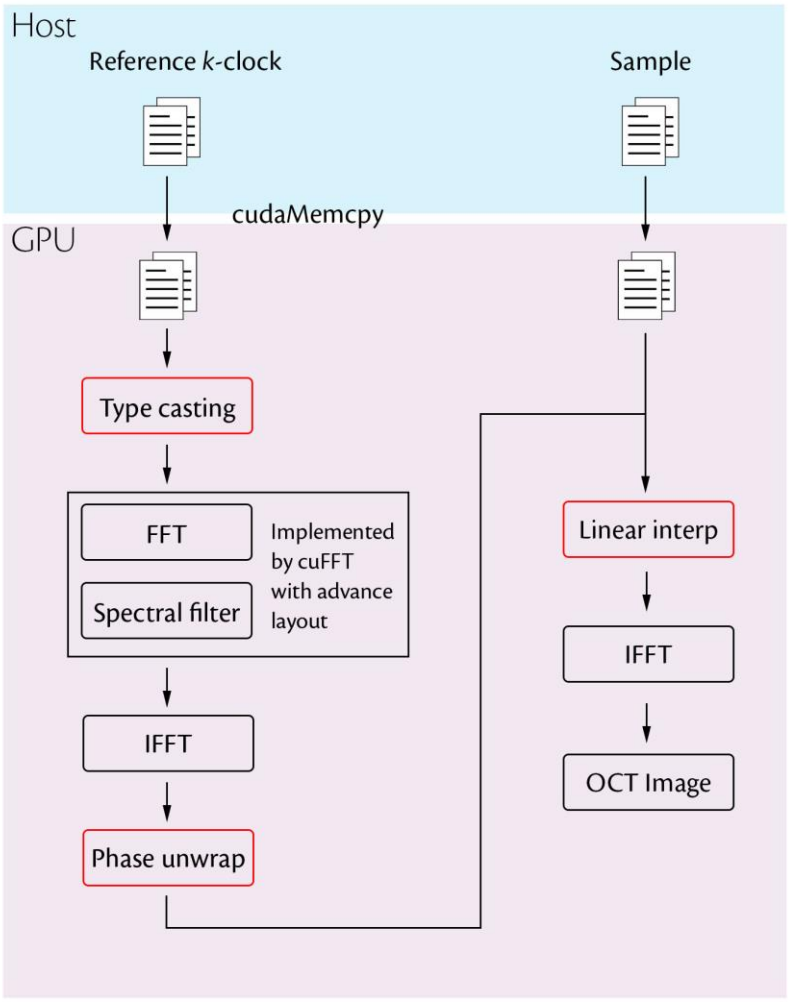

Figure 4-2 A block diagram for the GPU data processing of the SS-OCT data. The blocks in red, e.g. type casting, phase unwrap, and linear interp, are custom-implemented.

4.3.3 Kernels and functions

In Figure 4-2, a detailed block diagram of OCT data processing by using GPU is depicted. The four blocks painted in green, including “convert routine”, “filtering”, “phase unwrap”, and “linear interpolation”, are the kernels I developed. For the FFT and IFFT part, we simply use the provided cuFFT library for the best performance.

4.3.3.1 Typecasting routine

The first *kernel* I have implemented is a typecasting function to convert the input data from `unsigned short` type to `float32` (or `double`) type, so that the data can be processed by the GPU (`unsigned short` is not supported by the cuFFT library I am using). This typecasting issue seems trivial and unnecessary at the first glance: the conversion could be readily handled by manually looping the array and converting the values one by one on the host computer. However, transferring converted `float32` (or `double`) data instead of unsigned short one raises the data transferring rate immediately by a factor of 2 (or 4). Moreover, the type casting operation itself is highly parallelable, and a GPU implementation will greatly improve the performance.

In fact, the discrepancy of the data type between the output of the DAQ board and the input of the CUDA library was previously mentioned by Watanabe *et al*. [77].

4.3.3.2 Implementation of discrete Hilbert transform

The discrete Hilbert transform performed on the reference *k*-clock channel data is a very important procedure in SS-OCT data processing. The extracted instantaneous phase angle will be used to reconstruct the *k*-sweeping curve of the light source. The precision of this procedure will affect the resampling of the imaging channel data and further affect the overall phase stability of the reconstructed images as we will discuss extensively later in Chapter 5.

Here I used the spectral filtering method, which is previously mentioned in section 1.1.4.1. The discrete Hilbert transform is then approximated by performing the following steps,

1) Fast Fourier transform (FFT) the raw signal

2) Set the negative-frequency components to zeros, and reduce the amplitude of the DC component by half

3) Inverse fast Fourier transform (IFFT) the filtered signal

The FFT and IFFT are readily implemented in the latest cuFFT library within the CUDA package. There is no need for us to reinvent the wheel. The only task left is to simply filter out the negative-frequency components. Interestingly, I discover that this spectral filtering is not necessary to be implemented explicitly. In fact, it could be fulfilled by exploiting the "advanced data layout" feature of the cuFFT library.

Assuming that the input B-scan consists of M A-lines and each A-line consists of $2N$ samples, I could allocate a `cufftReal` array for the input data a `cufftComplex` array the output data, both of which is equal in element numbers ($M \times 2N$). Due to the symmetry property of the Fourier transform of a real sequence, the output complex sequence in cuFFT will only span half the length of the input real sequence. In other words, the negative-frequency components are already removed after performing the FFT, and a simple zero padding is needed to perfect the spectral filtering. I thus used `cufftPlanMany` to structure the output sequence: `inembed`, `idist`, `istride`, `onembed`, `odist`, `ostride`, is set to $2N$, $2N$, 1, N+1, $2N$, and 1, respectively. Therefore, the zeros will be automatically padded after the halved complex sequence without calling another spectral filtering routine explicitly.

The discrete Hilbert transformed sequence is later inverse FFTed to acquire the analytic signal of the original reference *k*-clock channel data.

4.3.3.3 Phase unwrapping

After obtaining the analytic signal of the reference *k*-clock channel data, I need to extract its instantaneous phase and unwrap it. The algorithm used in this kernel is based on the discontinuity detection. Assuming that the directly extracted phase angle $\phi[n]$ is wrapped in $[-\pi, \pi]$, the phase unwrapping algorithm is described as follows,

1) Calculate $\Delta\phi[n]$, which is the first difference of $\phi[n]$,

$$\Delta\phi[n] = \phi[n+1] - \phi[n] \tag{4.4.2}$$

2) Wrap $\Delta\varphi[n]$ into the range of $[-\pi, \pi]$,

$$\Delta\phi'[n] = \Delta\phi[n] + 2\pi C[n] \quad \text{s.t.} \quad -\pi \le \Delta\phi'[n] \le \pi \tag{4.4.3}$$

where $C[n]$ is the correction term and is an integer.

3) The unwrapped phase $\Phi[n]$ is given by,

$$\Phi[n] = \phi[n] = \sum_{m=0}^{n-1} 2\pi L[k] \tag{4.4.4}$$

This algorithm could be implemented on GPU with a high parallelism without the problem: the operation is element-wise except for the first difference (in Equation (4.4.2)) and the summation could be implemented with high efficiency by using *parallel reduction*, which will be discussed later in . Moreover, the algorithm itself works very well in my case, since the signal frequency as well as the signal SNR is tunable in SS-OCT's reference *k*-clock to avoid working in a low-SNR or high-frequency regime.

4.3.3.4 Linear interpolation

In SS-OCT, the analog signal is physically sampled in the time domain and it is not necessarily uniform in the wavenumber domain. Therefore, a re-sampling of the signal is required to make it linear in *k* domain. Linear interpolation is thus used,

$$S_{\text{resampled}}[n+1] = S[n](1 - \frac{\phi_{\text{linear}}[n] - \phi[n]}{\phi[n+1] - \phi[n]}) + S[n+1](\frac{\phi_{\text{linear}}[n] - \phi[n]}{\phi[n+1] - \phi[n]}) \qquad (4.4.5)$$

where $S[n]$ is the measured signal, $S_{\text{resampled}}[n]$ is the resampled signal, $\phi[n]$ is the *k*-scan curve (unwrapped phase from *k*-reference clock), and $\phi_{\text{linear}}[n]$ is the uniform grid in *k* domain.

Before the interpolation, $\phi[n]$ and $\phi_{\text{linear}}[n]$ are sorted by a simple linear search algorithm: for each $\phi[n]$, it will be compared against $\phi_{\text{linear}}[n]$ sequentially until a number N is found, so that $\phi_{\text{linear}}[N] \leq \phi[n] \leq \phi_{\text{linear}}[N+1]$. Since both $\phi[n]$ and $\phi_{\text{linear}}[n]$ are monotonic, linear search yields the best performance.

Although this algorithm is not the most suitable one for parallel computing due to the necessity of sorting, its performance could still be boosted by exploiting the vast computational resources provided by the GPU.

4.3.4 Optimization

In GPU programming, optimization is often more important and challenging than the plain implementation. Various optimizations techniques including occupancy optimization, asynchronous transfer, memory coalescing, parallel reduction among others are used in my program to speed up the computation.

4.3.4.1 Occupancy optimization

It is important to understand that the *thread* in CUDA is merely a programming concept: on the device level, *thread* is not individually executed but collectively in a form of *warp*, which comprises of 32 threads. Due to the limitation imposed by the total number of the registers, different thread-block layout will lead to different number of simultaneously resident threads. The ratio between the number of simultaneously resident threads of a kernel and the maximally allowable threads number is occupancy. Generally speaking, the higher the occupancy, the better the performance. Therefore, it is often a good practice to sweep the block size (the number of threads in each block) and the grid size (the total number of blocks in the problem space) to find the highest occupancy to ensure the best performance.

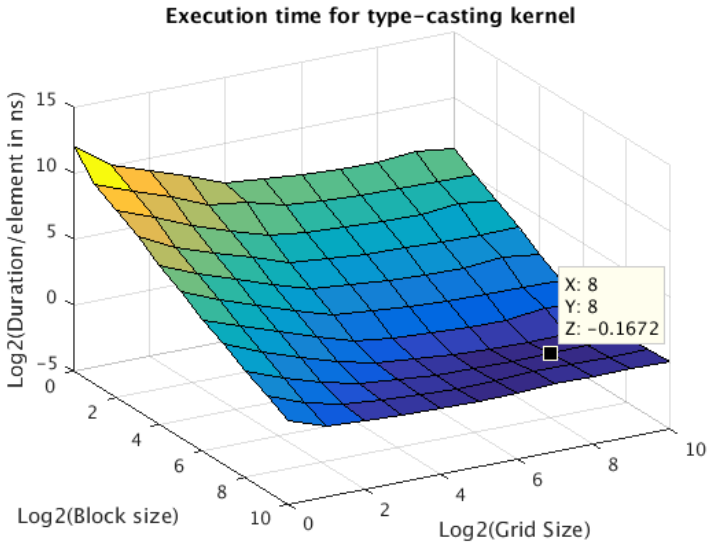

Figure 4-3 Block size & grid size optimizations for the typecasting kernel

For example, I optimized the typecasting kernel by sweeping the block size and grid size: both dimensions were swept from 2^0 to 2^{10}. The execution time against block size and grid size is plotted in the logarithmic scale as shown in Figure 4-3. I found that a block size of $2^8 = 256$

combined with a grid size of $2^8 = 256$ gave the best performance with an execution time of 0.8906 ns per element.

4.3.4.2 Memory coalescing

Accessing the global memory is generally slow in GPU computing. However, it could be greatly improved by using *memory coalescing*.

In CUDA programming, the access to the global memory is coalesced: a neighborhood of data is addressed at the same time no matter how many addresses are requested at the first place. For example, even if we are only interested in the value stored in address 0x00, we will have to load all the values from 0x00 to 0x08 and everything other than that of 0x00 will be discarded later, which will dramatically drag down the overall performance of the system. However, if we could program so that the data loaded by each transaction of data fetching could be utilized by the same thread warp, the overall requirement on the data bandwidth could be reduced.

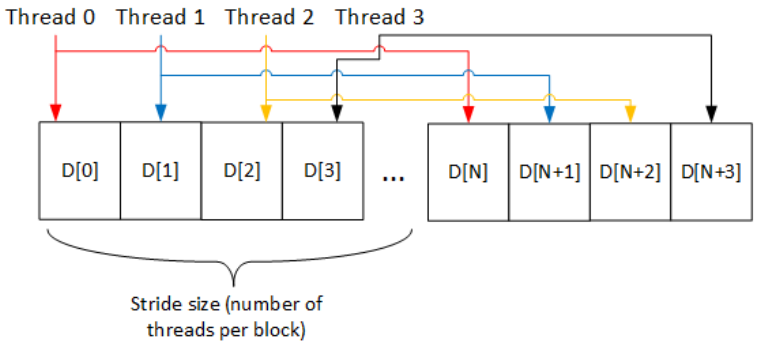

Figure 4-4 Memory coalescing.

To implement the “memory coalescing”, a particular number of input data, which is denoted by stride size and usually matches the count of the concurrent threads, are loaded in single operation and are collectively sent to the threads. Each thread then processed input data in parallel.

After the processing is finished, all threads then moved to the next address and repeat the loading and processing procedures. This is illustrated in Figure 4-4. The optimized stride size is obtained through parameter sweeping, while the block size and grid size are set to be the optimized values found above. In Figure 4-5 Execution I

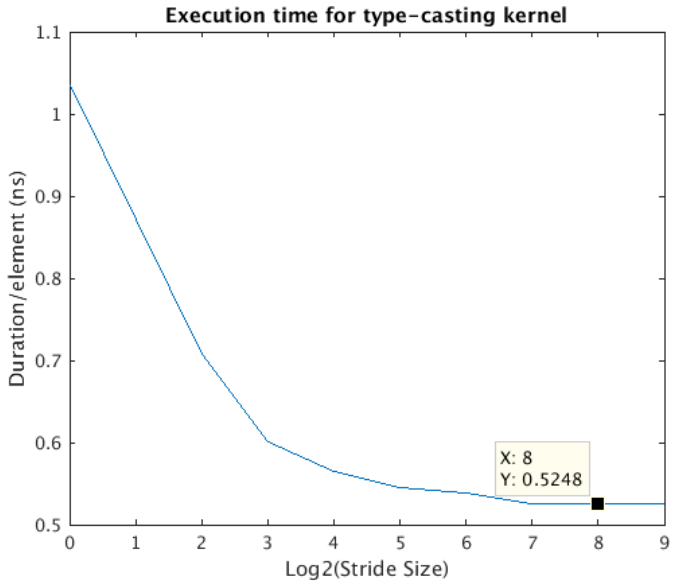

Figure 4-5 Execution time for type-casting kernel versus stride size (log2).

4.3.4.3 Asynchronous transfer

I further used CUDA *streams* to overlap the kernel executions and the memory transfer operations by calling `cudaMemcpyAsync` between the host and the GPU for task parallelism. A CUDA *stream* represents a queue of GPU operations that can be executed in a specific order. Multiple can be executed concurrently to accelerate the applications by running two or more completely different tasks in parallel.

It is worth noting that the manifestation of the asynchronous transfer requires the host memory to be pinned memory instead of pageable memory. The allocation of pinned memory

could be fulfilled by calling `cudaHostAlloc`. The pinned memory resides in the physical memory and the operating system never pages this memory out to disk. On the other hand, the pageable memory, allocated using the `malloc` function, can be paged in/out between the DRAM and secondary storage device in the host. When pageable memory is used, the CPU first copies the data from the pageable memory to a page locked memory, to or from which GPU copies the data using direct memory access (DMA). Here the copy operation happens twice. In contrast, when pinned memory is used, the first copying is not needed. Therefore, by using physical memory instead of the hard disk, the pinned memory provides improved transfer speed and larger throughput than the pageable memory.

4.3.4.4 Parallel reduction

Parallel reduction is a very common operation that is highly involved in scientific computation. For example, in the phase unwrapping kernel I just mentioned in last section, the partial summation (Equation (4.4.4)) could be accelerated by using the concepts of parallel reduction. All the details you need about how to maximize the parallel reduction could be found elsewhere [78].

4.3.4.5 Computation speed versus computation precision

It is not immediately obvious for most people that the using of `float32` instead of `double` could generate errors in a program. However, I have run into a situation that the cumulative error in the program of using `float32` could not be negligible and I have to use `double` instead.

An experiment was conducted to illustrate this. In Figure 4-6, I plotted the error between the CUDA (using `float32`) results against the MATLAB results of doing 1024 point discrete Fourier transform on the same dataset. The mean of the error is 1.41×10^{-4}. To the contrary, a much better computational precision could be obtained by using `double` precision instead of `float32`.

The resultant mean of the error is reduced to 3.56×10^{-13}, which is sufficient for our current purpose, is plotted in Figure 4-7 for comparison. It is worth noting that the `double` version imposes hefty penalties on the computation time compared with the `float32` version.

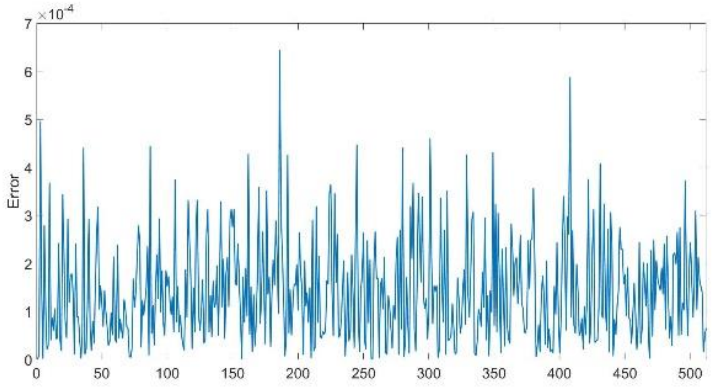

Figure 4-6 The error generated by using single-float cuFFT.

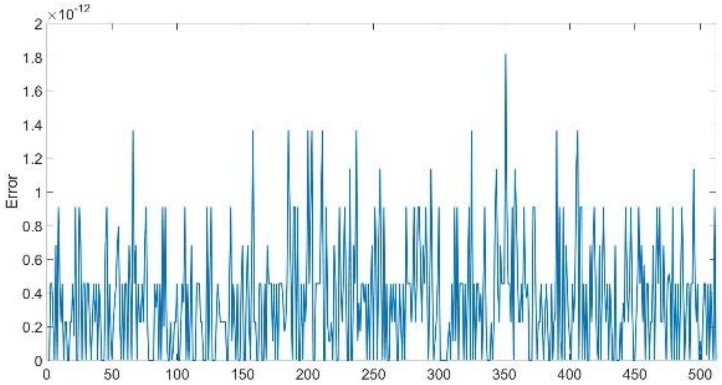

Figure 4-7 The error generated by using double cuFFT.

Chapter 5 Phase-resolved OCT

In Chapter 1, I have introduced an OCT theory based on a simplified multilayer model to understand its image formation as well as its imaging performance. It is shown that the object function $r(z)$, or its blurred version to be more precisely, could be reconstructed by performing an inverse Fourier transform on the measured spectral interferogram. It is worth noting that the reconstructed $\tilde{r}(z)$ is a complex function. In conventional OCT post-processing, researches only take the magnitude of $\tilde{r}(z)$ and use it as the structural (intensity) contrast. The absolute phase angle of $\tilde{r}(z)$ by itself is often considered to be meaningless, while the temporal variation of the absolute phase angle could be used to depict sub-wavelength displacement of object structure [49].

In fact, the utilization of phase information embedded in the OCT signal is started soon after the initial invention of OCT. In 1999, Chen *et al.* first proposed that pixel-level phase variation could be extracted by performing a Hilbert transform on the time-resolved interferogram [79]. Both computer simulation and *in vitro* experiment on a phantom system are conducted to prove the concept. Zhao *et al*. from the same group later presented that the pixel-level phase variation could be extracted to reconstruct the blood flow in human skin [80]. The phase change at each pixel location could be thus used to calculate the Doppler frequency shift in a depth-resolved fashion. It is also proposed that the standard deviation of the Doppler frequency shift could enhance the contrast of the image [49].

In the TD-OCT era, the phase noise resulted from the scanning reference arm is overwhelming, which makes the extracted phase information heavily contaminated. With the advent of FD-OCT, the landscape of phase resolved OCT was dramatically transformed. Thanks to the static reference arm in FD-OCT, the phase stability as well as the imaging speed of the

system has been greatly enhanced, which enabled tons of new applications. Choma *et al*. first proposed a phase-sensitive technique based on FD-OCT, which they coined as spectral domain phase microscopy [50]. They analyzed the mathematical form of the phase information in OCT, gave a theoretical limit on the phase noise, and experimentally presented the system's capability by measuring the sub-wavelength optical path length change of a beating chicken embryo.

5.1 The theory of phase sensitive OCT

Following the notation I used in Chapter 1, the detected interference fringe $I(k)$ of a single discrete reflector in a typical FD-OCT system can be written as,

$$I(k) = \rho[S(k)\sqrt{R_R R_S}\cos(2kz_d) + N(k)] \tag{5.1}$$

where $S(k)$ is the power spectrum of the light source, k is the wavenumber, ρ is the responsivity of the photodetector, z_d is the optical path length difference between the sample reflector and the reference mirror, $N(k)$ is the detection noise, and R_R and R_S are the reflectivity of the reference mirror and the sample reflector, respectively.

Before the analog signal $I(k)$ could be processed, it is first discretized in wavenumber domain k, and the resultant discrete signal could be written as

$$I[m] = I(k)\cdot\sum_{m=-\infty}^{\infty}\delta(k-m\delta k) = A[m]\cos[2(k[0]+m\delta k)\cdot z_d] + B[m] \tag{5.2}$$

where m is the index of the spectral sampling point, δk is the sampling interval in the k domain, $A[m] = \rho S[m]\sqrt{R_R R_S}/4$ and $B[m] = \rho N[m]/4$. For most samples, their spectroscopic properties are of no interest. Therefore, I could ignore the influence of the illumination spectrum and could

assume $A[m]$ to be a constant number A without losing generality. I then performed an M-point inverse discrete Fourier transform on Equation (5.2) against m, and the result is given by,

$$\begin{aligned} i[n] &= \frac{1}{M}\sum_{m=0}^{M-1} I[m]\exp[\frac{j2\pi mn}{M}] \\ &= \frac{A}{2M}\exp[-j2(k[0]+\frac{M-1}{2}\delta k)z_d - j\frac{n\pi}{M}]\frac{\sin(M\delta kz_d)}{\sin(\delta kz_d - n\pi/M)} \\ &+ \frac{A}{2M}\exp[j2(k[0]+\frac{M-1}{2}\delta k)z_d - j\frac{n\pi}{M}]\frac{\sin(M\delta kz_d)}{\sin(\delta kz_d + n\pi/M)} \\ &+ b\exp(-j\phi) \end{aligned} \tag{5.3}$$

where b is a constant, if we consider $B[m]$ to be an additive white Gaussian noise (AWGN). For an AWGN, the phase angle ϕ could be modeled by a uniform distribution over $(-\pi, \pi]$. The first and the second terms on the right-hand side of Equation (5.3) are the OCT image and its conjugate, respectively. For most OCT setups, these two parts could be well separated by manually adjusting the OPL difference between the sample and the reference mirror. Therefore, I will restrict my discussion on the first term.

The first term consists of two parts: a *sinc*-like function that defines the resolution (PSF) of the image, and a complex exponential function that gives the instantaneous depth-resolved phase angle. The *sinc*-like function reaches its maximum value when

$$n = [M\delta kz_d/\pi] \tag{5.4}$$

where the square brackets represents for the floor funtion. Let us define $N = M\delta kz_d/\pi$ for convenience, and the axial coordinate of this peak location to be z_N. The phase angle β of the obtained OCT signal at its peak location is,

$$\beta[n=\frac{\delta k z_N M}{\pi}]=-2(k[0]+\frac{M-1}{2}\delta k)z_d-\delta k z_N \tag{5.5}$$

It is interesting to see that the instantaneous phase angle β at the peak of the reconstructed reflector is not zero, although the original object function is a real function. The equation above could be rearranged

$$\beta[n=\frac{\delta k z_N M}{\pi}]=-2(k[0]+\frac{M}{2}\delta k)z_N-2(k[0]+\frac{M-1}{2}\delta k)\delta z \tag{5.6}$$

where $\delta z = z_d - z_N$ represents for the sub-axial-sampling-interval displacement. If the sample is translated in a large scale, we could not infer its motion from the modulation on its phase. However, if the object is slightly displaced in the order of the wavelength of the probing light, the phase angle will change linearly with the displacement δz. And this is the foundation of the phase resolved OCT.

5.2 The source of the phase noise

At the end of the previous section, we provided an equation from which people could extract the sub-axial-sampling-interval displacement δz. However, a faithful demodulation of δz relies on the assumption that both $k[0]$ and δk are constant values. In SD-OCT, this condition generally holds. The input broadband light is dispersed spatially by the spectrometer, and detected by a linear detector array. As long as the light source is stable and no mechanical movement is induced in the spectrometer setup, both $k[0]$ and δk are constant.

Unfortunately, the same condition is not guaranteed in SS-OCT. Unlike SD-OCT, the illumination spectral of the SS-OCT is temporally dispersed and detected by a photoreceiver. Neither the illumination part nor the detection side is stable.

First of all, the output spectrum of the wavelength swept laser source could vary from scan to scan, as illustrated in Figure 5-1(a), due to the imperfections existed in mechanical or electrical scanning. Ideally, we are expecting a wavelength scanning curve that is linear in time, which is illustrated by the black solid line. However, the actual wavelength scanning curve deviated from the ideal curve as shown in the red dash-dotted line. At a given temporal sampling point m, the deviation in wavenumber $\delta k[m]$ is the difference between the actual instantaneous wavenumber $k[m]$ minus the ideal $k[m]$. This wavenumber deviation over the time domain could be modelled as a random variable, and we call it "scanning variability". Without losing generality, we could assume that all $\delta k[m]$ (m=0, 1, 2, … , M – 1) follow the same normal distribution with a zero mean and a standard deviation of $\sigma_{\delta k}$. Therefore, both $k[0]$ and δk in Equation 5-6 are random variables instead of constants.

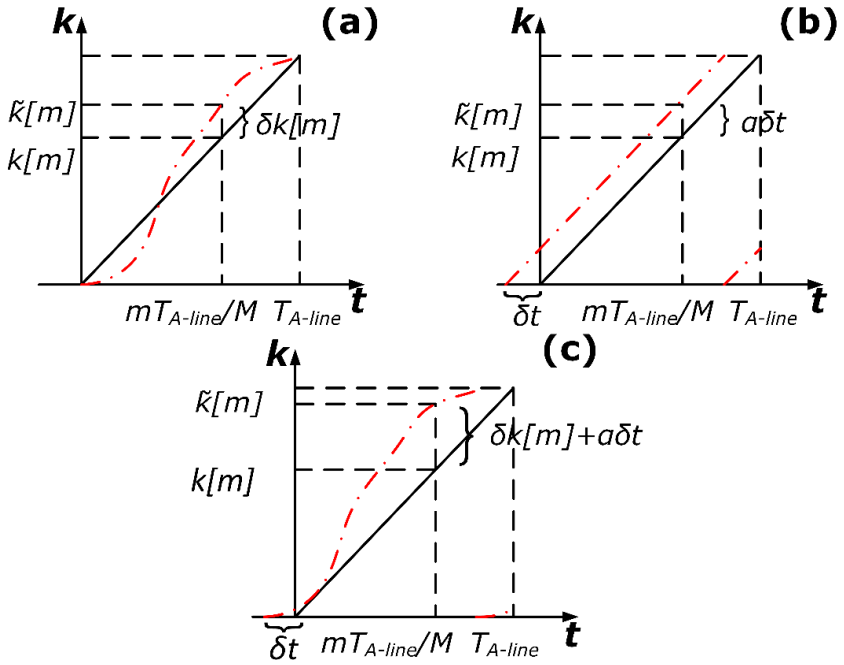

Figure 5-1 Effect of (a) scanning variability, (b) timing jitter, and (c) both on the scanning curve of SS-OCT.

Secondly, there exists a timing jitter between the starting time of the data acquisition and that of the actual wavelength sweep as shown in Figure 5-1(b). This arises from multiples causes. The most obvious cause is the imperfect synchronization between the light source trigger and the data acquisition board: there are various type of delay during the signal transmitting, and the noise presented in trigger signal also plays a role. The other cause is somewhat inconvenient: the timing jitter is effectively limited by the sampling rate of the DAQ. We use Figure xx to clarify this point … . Therefore, we could conclude that the timing jitter of the second type is inherent to the SS-OCT due to its nature of temporal sampling. The first type of error, which is induced by the imperfect synchronization, is easy to correct. Various techniques have been proposed to suppress its effect. Therefore, we are focused to model the second type of jitter, which is caused by limited sampling rate. The timing jitter could also be considered as a random variable. Based on the previous discussion, it is prudent to assume that the jitter is proportional to the sampling period: a slower DAQ will lead to a larger timing jitter and a faster DAQ will result in a smaller timing jitter. Therefore, we assume δt also follows a zero-mean normal distribution, and its standard deviation is written as $\sigma_{\delta t} = lT_{\mathrm{DAQ}}$. The impact of the introduction of δt on the measured wavenumber k is translated via the scanning speed of the light source $\alpha=(k[M-1]-k[0])/T_{\text{A-line}}$. Here, $T_{\text{A-line}}$ is the A-line scanning period of the light source.

$$\beta[n=\frac{k'z_N M}{\pi}]=-2(k[0]+\frac{M}{2}k')z_N-2(k[0]+\frac{M-1}{2}k')\delta z-2(\alpha\delta t+\delta k)z_N \\ +o(\delta t\delta z)+o(\delta k\delta z) \tag{5.7}$$

The first term in Equation (5.6) corresponds to the structural information that is readily available in OCT; the second term represents the sub-axial-sampling-interval phase term that techniques such as phase-resolved OCT intend to decouple; the third term is the phase modulation

introduced by both the time jitter and the scanning variability. The rest of the terms are considered higher order infinitesimals that could be ignored.

In addition to the phase uncertainty, we also need to add back the intensity noise to obtain a full depiction.

5.3 Phasor interpretation of the noise

To better understand the noise constituents and their effects on the original signal phase, we use the phasor notation to assist visualization as shown in Figure 5-2. Let us assume that the signal phasor A has a constant amplitude of 1, and an initial phase angle of β_0, which is given by the second term of Equation (5.7). The inclusion of the third term in Equation (5.7) effectively rotates the phase angle of A by $\delta\beta$. It is worth noting that the angle is also affected by the sample location in the axial direction.

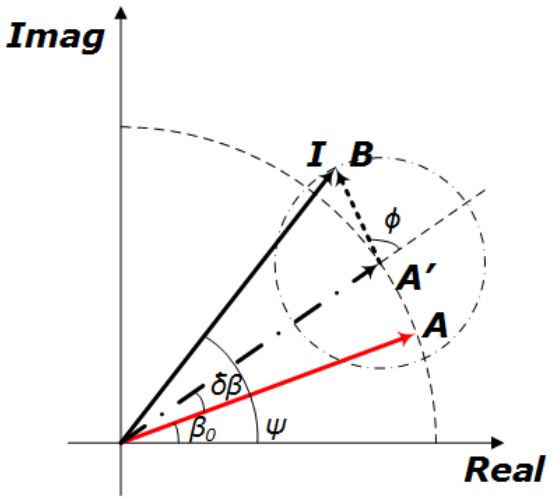

Figure 5-2 A phasor depiction for the phase angle in SS-OCT.

The resultant phasor *A'* after rotation is further affected by the intensity noise, which is a AGWN. We could model it as a randomly oriented phasor with a fixed amplitude *B*, which is

proportional to the noise intensity. The phase angle φ simply follows a uniform distribution. The final resultant phasor I could be written as,

$$\vec{I} = \vec{A} \cdot \exp^{-j\delta\beta} + \vec{B} \tag{5.4}$$

5.4 Calculation of the phase noise

5.4.1 Analytic analysis

As laid out in the previous section, the measured phase angle ψ from SS-OCT might be greatly deviated from the actual value β_0 due to the presence of three random variables: δk, δt, and φ. It is worth noting that the effect of both δk and δt are multiplicative. The parameters for these random variables are summarized in Table. 1.

Without losing generality, we could assume that $\beta_0 = 0$. Let $\varphi' = \varphi + \delta\beta$, we have

$$\begin{aligned} \tan\psi &= \frac{b\sin\phi' + \sin\delta\beta}{b\cos\phi' + \cos\delta\beta} \\ b\sin(\psi - \phi') &= \sin(\delta\beta - \psi) \\ \delta\beta &= \psi + \arcsin[b\sin(\psi - \phi')] \\ \delta k &= \frac{\psi + \arcsin[b\sin(\psi - \phi')]}{z_N} \end{aligned} \tag{5.5}$$

Since δk follows a normal distribution $N(0, \sigma_{\text{total}})$, the probability density function of δk is given by

$$f_{\delta k}(\delta k) = \frac{1}{\sqrt{2\pi}\sigma_{total}} \exp(-\frac{\delta k^2}{2\sigma_{total}^2}) \tag{5.6}$$

Then, the probability density function of ψ for a given φ could be calculated,

$$f_{\psi}(\psi \mid \phi') = f_{\delta\beta}(\delta\beta)\frac{d(\delta\beta)}{d\psi} = \frac{1}{\sqrt{2\pi}\sigma_{total}}\exp[-\frac{\{\psi - \arcsin[b\sin(\phi' - \psi)]\}^2}{2\sigma_{total}^2 z_N^2}] \cdot[1 + \frac{b\cos(\phi' - \psi)}{z_N\sqrt{1 - b^2\sin^2(\psi - \phi')}}] \tag{5.7}$$

We finally compute the probability density of ψ by integral over φ, and obtain the following analytic form,

$$f_{\psi}(\psi) = \int_{-\pi}^{\pi} \frac{1}{\sqrt{32\pi^3}\sigma_{total} z_N} \cdot \frac{z_N\sqrt{1 - b^2\sin^2(\psi - \phi')} + b\cos(\phi' - \psi)}{\sqrt{1 - b^2\sin^2(\psi - \phi')}}] \cdot \exp[-\frac{\{\psi - \arcsin[b\sin(\phi' - \psi)]\}^2}{2\sigma_{total}^2 z_N^2}]d\phi' \tag{5.8}$$

where

$$\sigma_{total} = \alpha^2\sigma_{\delta t}^2 + \sigma_{\delta k}^2 = \alpha^2(lT_{DAQ})^2 + \sigma_{system}^2 \tag{5.9}$$

Recall that we assumed β_0 was equal to 0. Therefore, the statistics of ψ essentially give the statistics of the phase noise (phase measurement error) resulted from the light source, sampling, and detection. We could thus use the Equation (5.9) to calculate the theoretical phase noise in SS-OCT. Unfortunately, the above equation could neither be integrated to an analytic form nor could be numerically computed in our case: a numerical resolution of 10^{-50} is required. So, we solve this problem by using Monte Carlo simulation instead.

5.4.2 Monte Carlo Simulation

Before the discussion, we need to first define the following k-sweep variation coefficient *W* to conveniently characterize the system phase stability

$$W = -10\log_{10}\frac{\sigma_{total}}{\bar{k}} \tag{5.10}$$

where $\bar{k}$ is the wavenumber of the central wavelength of the light source. The larger the W is, the higher phase stability the system possesses. We also formally define the SNR of the system to be

$$SNR = -20\log_{10} b \tag{5.11}$$

For the Monte Carlo simulation, we first launch a photon, whose amplitude is 1. The photon will first be rotated by a random angle $\delta\beta$, which is generated by a normal distribution $N(0, \sigma_{\text{total}})$. After that, a noise vector, whose amplitude is b, is added. Its angle is randomly generated by a uniform distribution. For each pair of σ_{total} and b, i.e. W and SNR, 10 million of photons are simulated. We then calculated the standard deviation σ_ψ to evaluate the phase stability of the system at different conditions.

In Figure 5-3(a), we presented an exemplary plot to illustrate the phase stability of the system under different conditions (W and SNR). The phase stability is color coded and presented in logarithmic scale. We further plotted the RMSE of the measured phase at different SNRs against W in Figure 5-3(b). When the k-sweep variation coefficient, W, is very low, the system suffers large noises from the scanning variability and the timing jittering. The measured phase angle ψ is random in the entire range of $[-\pi; \pi]$. In this regime, σ_ψ is bounded and is not changed with either SNR or W. When W rises above a certain threshold (~30 dB), σ_ψ starts to reduce linearly against W in logarithmic scale. If W is further increased, σ_ψ will saturate at a certain level that is determined by both SNR and z_N . We also plotted σ_ψ at different values of W against SNR in Figure 5-3(c). When SNR is large, the noise b in Equation (5-8) approaches 0. The probability distribution function shown in Equation (5-8) is equivalent to a normal distribution with a standard deviation of $2\sigma_{\text{total}}z_N$. It is noted that σ_ψ tends to saturate at a higher level with higher W. For large W (>60

dB), σ_ψ is mostly linear in the selected dynamic range. In fact, the curve will converge to the previously reported SD-OCT case [49] if W goes to infinity.

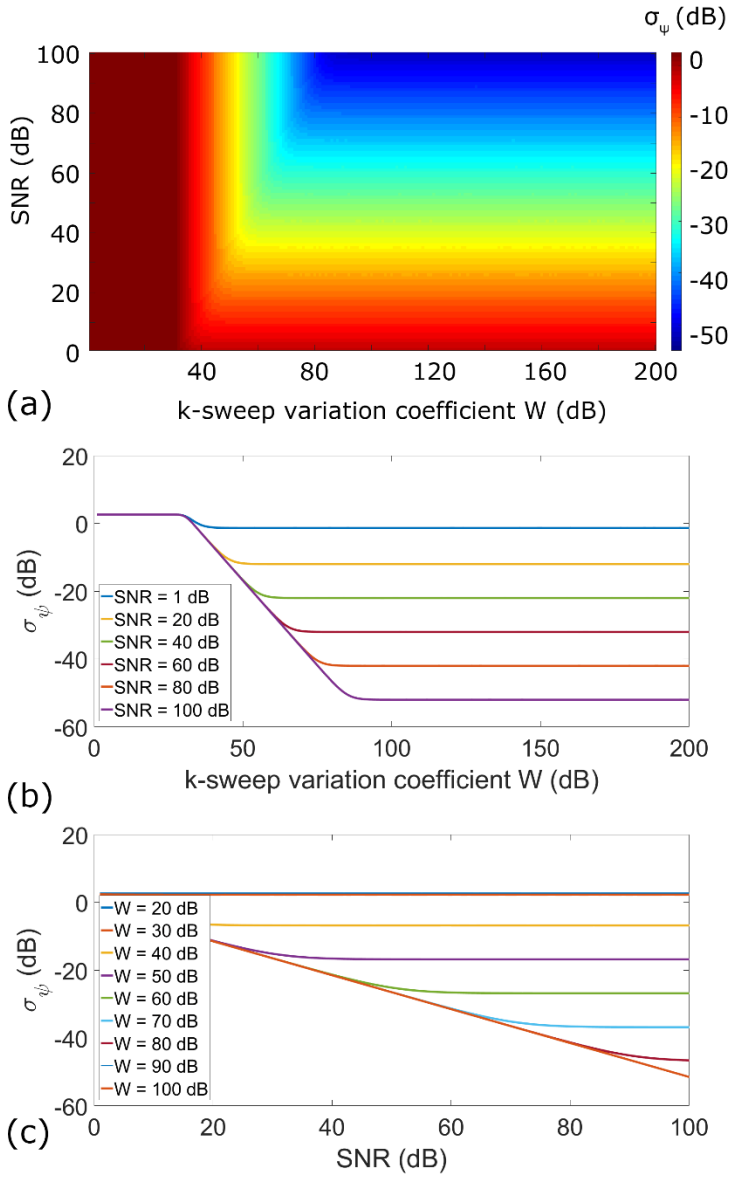

Figure 5-3 Monte Carlo simulation of the proposed model. The calculated standard deviation of the final phase angle is first plotted as a pseudo-color image against SNR and W in logarithmic scale in (a). The σ_ψ are plotted against W in (b) and SNR in (c), respectively.

5.5 Experimental verification

Experiments were conducted to verify the proposed model. The custom-built SS-OCT system described in previous chapter was used. Two light sources including the NTT's akinect light source as well as the Santec's MEMS light source are tested. Since the scanning variability is inherent to a specific system, we first verified the effect of timing jitter with controlled z_d. A piece of No. 1 glass coverslip was used, and we altered the δt by changing the sampling rate of the DAQ from 200 MS/s to 1.8 GS/s. For each sampling rate, we tuned the SNR of the OCT signal by a continuously variable neutral density filter (NDC-25C-4M, Thorlabs, U.S.). The results are plotted in Figure 5-4(a). As a comparison, we also added the experimental data obtained from a 32 kHz SD-OCT system using a superluminescent diode. The SD-OCT measurements were very close to the theoretical limit as predicted in [49]. However, the SS-OCT measurements saturated at higher SNR; this behavior is predicted in our model, as shown in Figure 5-3(c).

A family of curves $\sigma_\psi(\sigma_{\text{total}}, \text{SNR})$ was obtained based on Equation (5.8) via Monte Carlo simulation and then fitted to the experimental data (σ_ψ, SNR) by using least squares approximation. The fitted σ_{total} are listed in Table 5-2.

After that, we used the fitted σ_{total} to obtain the coefficient l and σ_{system} in Equation (5.9). From Figure 5-4(b), we can see that the fitted coefficient l is equal to 0.5612, and the fitted σ_{system} is 89.68 m^{-1}. We then fixed the sampling rate of the DAQ to be 800 MS/s and validated our model with different values of z_d. We used No. 1 (110 μm), No. 1.5 (130 μm), and No. 2 (170 μm) glass coverslips as samples in a common-path configuration. Theoretical predictions were made by using the fitted parameters l and σ_{system}. The experimental data and the theoretical predictions presented great agreements, as shown in Figure 5-4(c). In summary, the fitted timing jitter of the

system at 800 MS/s is 701.5 ps, while the fitted scanning variability is 0.0019% compared with $\bar{k}$.

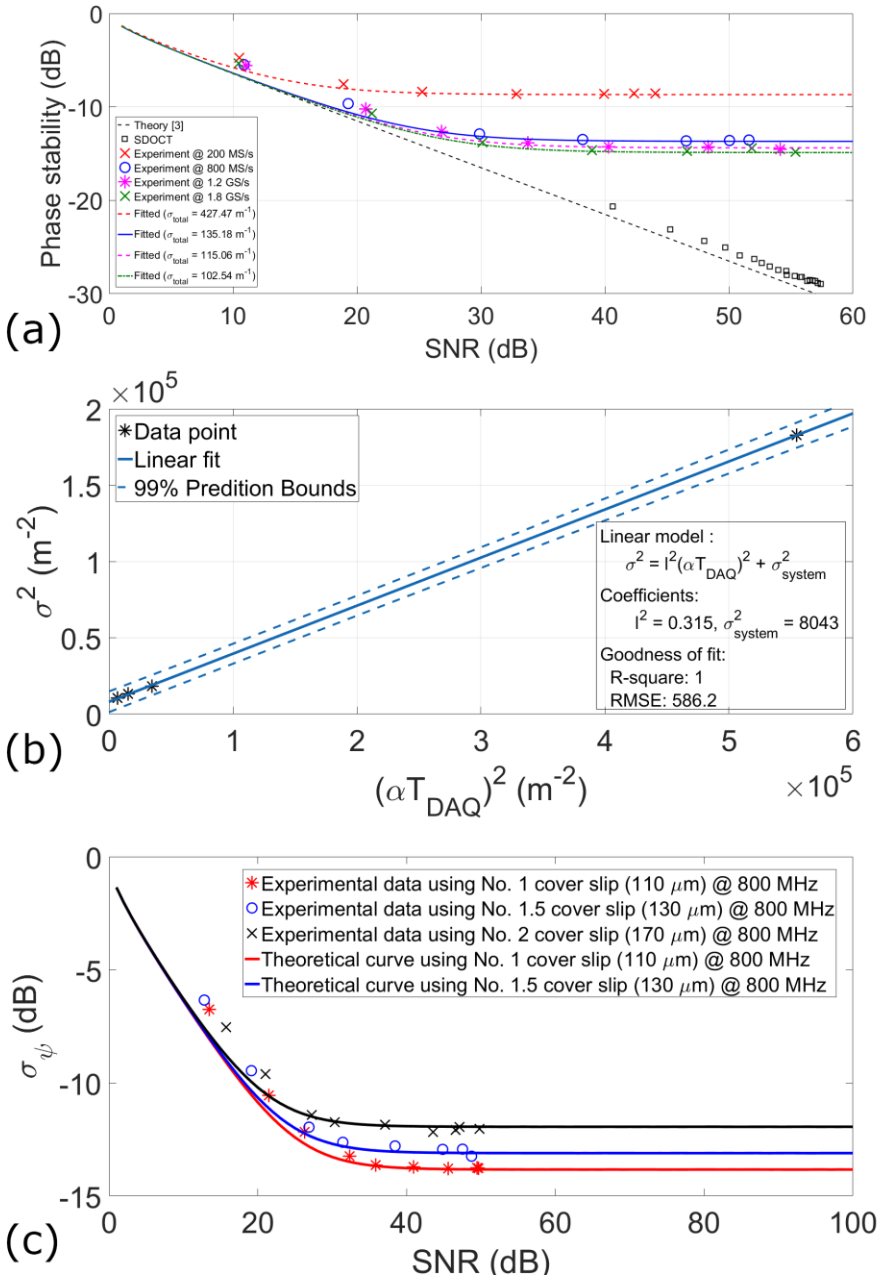

Figure 5-4 Experimental verification of the proposed model. (a) A No. 1 glass coverslip was tested by both SD-OCT and SS-OCT systems. The theoretical limit of SD-OCT was calculated using Choma's model

5.6 Summary

In conclusion, we presented a new theoretical model for phase noise analysis of SS-OCT. Compared with the models previously conceived upon SD-OCT, the proposed model incorporates two new factors and fits the SS-OCT experimental data better. The new model also suggests that SS-OCT is fundamentally at a disadvantage in absolute phase measurements against SD-OCT in terms of phase stability/sensitivity due to its temporal measurement nature; the collection of the three factors affects as a multiplicative noise on the original signal in addition to the additive noise such as the shot noise and the excess noise. The sole increment on the SNR will no longer boost the phase stability in SS-OCT. However, there are merits for using SS-OCT in phase-related tasks. The faster A-line acquisition of SS-OCT could improve the temporal resolution of sectional or volumetric phase measurements. The variance on the absolute phase measurement could also be washed out if the absolute measurement was later Fourier transformed to obtain the vibrational information.

Chapter 6 High speed imaging of *ex vivo* human ciliary motion

Cilia-driven mucociliary clearance (MCC) is a self-defense mechanism in pulmonary system with great clinical importance. Conventional light microscopy possesses the capability to visualize individual cilium and its beating pattern but lacks the throughput to assess the global ciliary distribution, depth-resolved ciliary motion, and cilia-induced flow dynamics. OCT, which possesses the optical resolution within millimeter-level imaging range, is recently introduced to this area in the hope of solving the aforementioned issues.

In this chapter, I will discuss a series of studies that we have conducted on imaging *ex vivo* human tracheobronchial ciliated epithelia. Multiple OCT systems including a commercially available SD-OCT, a custom-built high-resolution SD-OCT, and our high-speed phase-stable SS-OCT are used.

6.1 Introduction

Cilia are microscale protrusions from ciliated epithelium and can be either motile or immotile. They are very common structures in human body and are found in various organs' linings such as respiratory tracts, fallopian tubes, epididymis, and middle ear. Afzelius suggested that the cilia could be divided into 8 categories based on their functionalities [81]. In our study, we are most interested in the "Mucus-propelling cilia", which is also known as respiratory cilia.

The respiratory cilia reside densely on the upper and lower airways. A typical histological slide showed that a single respiratory epithelium cell could be covered by up to 200 cilia as illustrated in Figure 6-1 [82]. Each individual cilium has a typical length of 5-7 μm with a diameter

less than 1 μm. Under normal circumstances, the cilia are submerged in the periciliary liquid (PCL), which is the lower part of a two-layer airway surface liquid (ASL), and beat periodically. The ciliary beating is believed to consist of two strokes. During the effective stroke, the tip of the cilium reaches the upper layer of ASL (mucus layer) and shove the layer forward. On the other hand, during the recovery stroke, the tip of the cilium is lowered in height so that the mucus layer will not be driven backwards. This procedure is illustrated in Figure 6-2. More interestingly, the ciliary motion is collective: adjacent cilia usually possess the same ciliary beat frequency (CBF) but differs in phase, which result in a metachronal wave [83]. Therefore, a constant, unidirectional, forward mucous flow is generated and is commonly referred as mucociliary clearance (MCC).

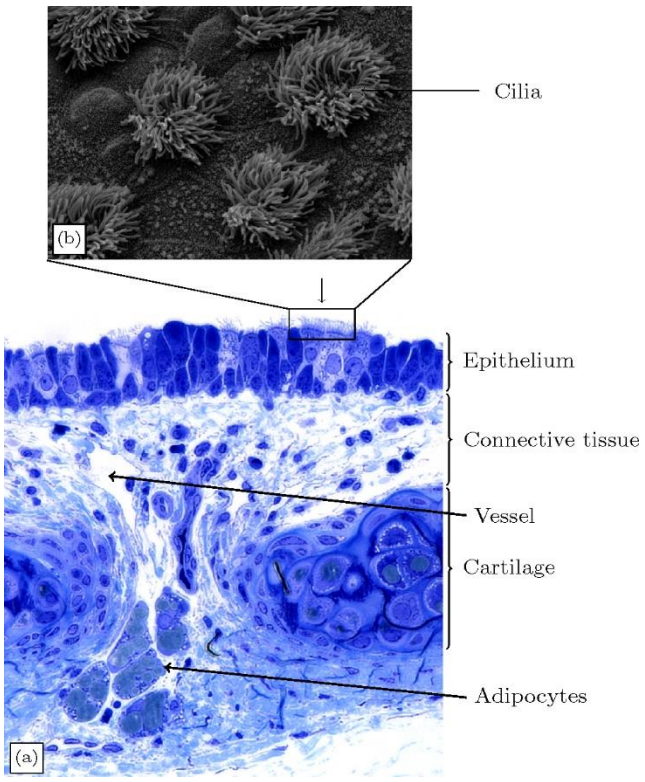

Figure 6-1. (a) H&E stained histology of trachea cross-section, (b) Scanning electron microscope image of ciliated cells. Reprinted with permission from ref [82], [OSA].

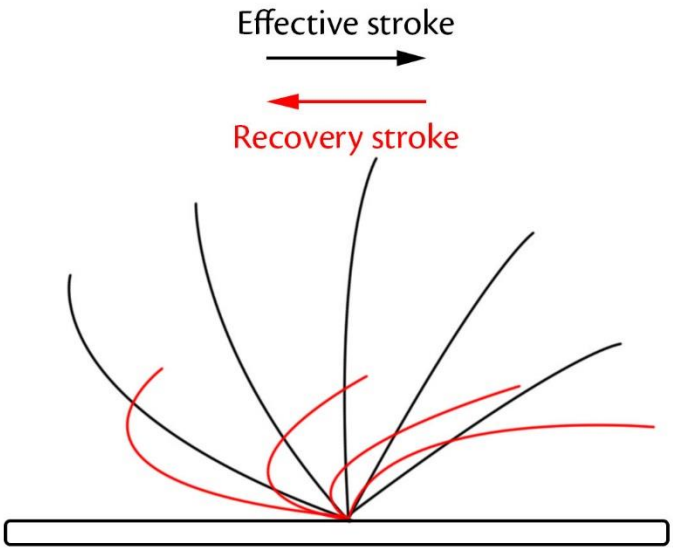

Figure 6-2 An illustration for ciliary motion. Black lines represent the position of a single cilium during the effective stroke. Red lines represent the positions of a single cilium during the recovery stroke.

Conventional light microscopy and confocal microscopy have been widely used for direct visualization of cilia and measurement of related parameters such as ciliary beat frequency (CBF) [84]. However, due to the inherent limits on the spatial-bandwidth product imposed on high numerical aperture (NA) systems, the field-of-view of the aforementioned technology is inadequate to evaluate more global parameters such as flow pattern, and depth-resolved flow rate.

Recently, optical coherence tomography (OCT) has been applied to study the human respiratory system [85-87], and the MCC in specific, thanks to its cross-sectional imaging capability and fast imaging rate. Like conventional light microscopy, an OCT image can be used to directly assess ciliary motion. Liu *et al.* used high-resolution micro-OCT which enabled direct visualization of ciliary activities on cultured human bronchial epithelial (HBE) and swine trachea samples. The motion pattern of cilia and CBF was directly extracted from the intensity image [88].

The latest work by the same group presented an *in vivo* animal study, in which they quantitatively measured the mucociliary transport rate [59].

Although not every OCT possesses the high resolution to allow for the resolving of individual cilium, it is still possible to extract parameters from ensemble measurements. Oldenburg *et al.* presented a quantitative imaging of mucus flow and a semi-quantitative analysis of CBF [89], Wang *et al.* reported an in vivo mapping of cilia located in mouse oviduct using a similar method [90], Lemieux *et al.* demonstrated that the CBF could also be extracted from the Doppler frequency shift [91].

On the other hand, it is also possible to increase the contrast and study the flow dynamics by adding exogenous agents. Jonas *et al*. proposed an OCT based particle tracking velocimetry (PTV) to characterize the cilia driven flow on the ciliated epithelium of Xenopus tropicalis embryos [92]. Follow up studies by the same group further expand the measurement to three dimensions [93, 94].

6.1.1 Objective

Despite the recent surge of using OCT to observe ciliary motions, there is not many studies dedicated to *ex vivo* human samples which we deemed as a stepstone towards future *in vivo* experiment: compared with the popular cultured HBE cells, excised human tissues feature complex morphology and actually secreted mucus, both of which are essential to *in vivo* imaging quality but missing from the cultured HBE cells. The large elevation presented in human tissues might impose harsher requirements on the imaging system, while the freshly secreted mucus might possess distinctive optical property and might obstruct the observation of ciliary activities below.

Therefore, the aim of this study is first to establish a protocol for observing *ex vivo* human tracheobronchial ciliary motion by using OCTs. Multiple systems and various post-processing techniques are later used to extract three important ciliary functions including cilia coverage and ciliary beating frequency (CBF). A preliminary study on characterizing cilia-induced flow dynamics is also presented.

6.2 Method

6.2.1 Sample preparation

In our study, we used only de-identified human tissues, which were reviewed by the Columbia University Institutional Review Board and deemed not human subjects research. Human tracheal/bronchial tissues were obtained from discarded regions of healthy donor lungs at the time of surgical lung transplantation and processed as previously described [95]. In brief, regions of trachea or mainstem bronchi that were trimmed in preparation for anastomosis of the donor lung to a recipient's mainstem bronchus were collected and immersed in Medium 199 (Gibco, USA) and bubbled overnight in 5% CO_2 and 95% O_2 at 4 ℃. The tissue was carefully dissected without damaging the ciliated epithelium, and cut into square patches to flatten the surface. The tissue was warmed in a water bath at 37 ℃ right before the imaging experiments. All patches were kept in Medium 199 during transport, warming, and imaging.

6.2.2 Experiment procedure

During the experiment, one patch of the tissue was placed in Medium 199 in a 35-mm glass petri dish (Fisher Scientifics, USA) on top of a gauze layer with the ciliated epithelium facing upward. The petri dish was heated by a close-looped heating platform (TC-423C, Warner Instruments, USA) at 37 ℃, while the platform was placed under the sample objective of the SD-OCT (Telesto I, Thorlabs, USA), a custom built 800-nm high resolution SD-OCT system [96], and another custom

built 1300-nm phase stable SS-OCT system [44]. For flow imaging, 20 μL 0.0099% solids 5.15-μm polyester microspheres (Bangs Laboratories, Inc., USA) were added to the solution as contrast enhancement agents.

6.2.3 Image protocol

6.2.3.1 B-scan imaging

Table 6-1 Imaging system configuration for B-scan imaging

	FOV (length × depth)	Axial resolution	Lateral resolution	A-lines per B-scan	A-line rate
Thorlabs	2/4 mm × 2.51 mm	6.5 μm	15 μm	2048	28 kHz
High-resolution	2 mm × 1.78 mm	2.72 μm	5.52 μm	500	42 kHz
High-speed	4 mm × 2.5 mm	15.7 μm	16.5 μm	1024	200 kHz

6.2.3.2 Volumetric functional imaging

Three-dimensional functional images were only acquired by using high-resolution system. A special scanning protocol was programed in LabView (National Instruments, USA). The FOV was 2 mm (length) by 4.4 mm (width) by 1.78 mm (depth). For each width location, 30 consecutive B-scans were acquired at 42 kHz. The step size in width direction was 100 μm.

6.2.3.3 Time-elapse imaging

Two-dimensional time-elapse images were obtained from the high-speed SS-OCT system. The FOV is set as 4 mm (length) by 2.5 mm (depth). For each location, more than 2,000 frames are recorded within 10 seconds and the equivalent frame rate is over 200 frames per second (fps).

6.2.4 Histology processing

The tracheobronchial tissue samples were fixed in 10% neutral buffered formalin solution for 24 hours. They were then transferred to 70% ethanol, dehydrated, embedded in paraffin and sectioned as per standard protocols by the Histology Service Center of the Molecular Pathology department at Columbia University Medical Center. For each specimen, 10 tissue levels were taken with 100 μm displacement. The tissue sections were stained by H&E and digitalized by using an Aperio system (Leica Biosystems, Germany) at 40x. ImageScope (v12.1.0.5015, Aperio Technologies, USA) was used to review and export the digital images.

6.2.5 Post processing

6.2.5.1 Intensity B-scan image

For intensity B-scan images, I am mostly interested in the structural information and its correlation with the histology slides. Therefore, the raw images were first spatially filtered by a 3×3 median filter frame by frame to reduce the salt-and-pepper noise. The preprocessed data were then averaged for 4 consecutive B-scans to further improve the contrast. The histogram of averaged B-scans was adjusted in ImageJ for best visual effect.

6.2.5.2 Speckle variance contrast for cilia mapping

The time-series B-scan images were processed in a way similar to that reported in [89]. The flow diagram of the speckle variance imaging is provided in Figure 6-3. The maximum intensity projection (MIP) of the B-scan stack (not in logarithmic scale) is first computed long the time axis. The maximum intensity projection is manually thresholded to generate a binary mask, which excludes the extremely bright part of the image such as the air-medium interface, mucous clouds, and cartridge surface. The standard deviation of the stack is also calculated and normalized by

median filtered image in a pixel-by-pixel manner. The normalized standard deviation image is then multiplied by the binary mask to generate the final speckle variance image.

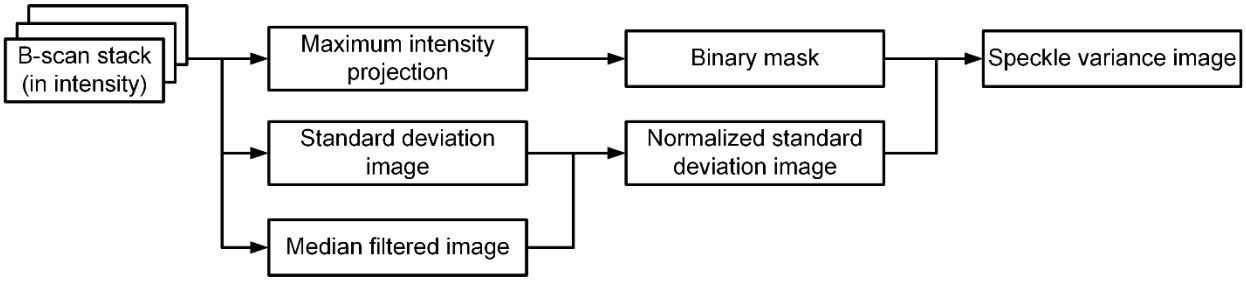

Figure 6-3 The flow diagram for speckle variance image processing.

6.2.5.3 Temporal frequency analysis for CBF

By taking advantages of the higher axial resolution of the custom-built system, I performed a temporal frequency analysis on the time-series B-scan images following the method reported by Wang *et al.* [90, 97]. The imaging configurations as described in section 6.2.3.1 were the same, except that the number of the frames acquired for analysis was increased to 1,350. 1D Fourier transform was performed on the time-series data in a pixel-by-pixel manner. For each pixel within a B-scan, a temporal spectrum was obtained. I then looked for a dominant frequency with maximum power spectral density corresponding to the CBF in the temporal spectrum in the range of 3 Hz to 20 Hz. The amplitudes of the dominant frequencies were first thresholded to create a binary mask. Color-coded maps were used to visualize the spatial distribution of the dominant frequencies as well as the peak amplitudes above the selected threshold. A flow diagram is provided in Figure 6-4.

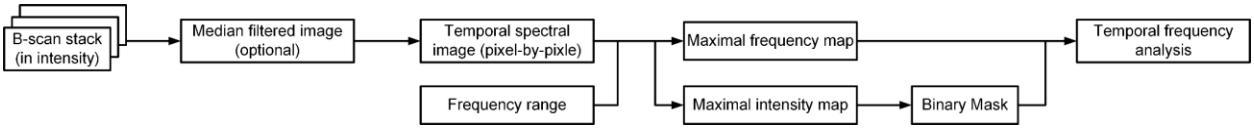

Figure 6-4 The flow diagram for temporal frequency analysis.

6.2.5.4 Phase variance analysis

I also used a phase-based contrast technique reported by Chen *et al.* to improve the contrast of the ciliary visualization [98]. I first take the depth-resolved phase angle $\varphi_i(x, z)$ from the complex OCT images, and then compute the signal $C(x, z)$ as the averaged phase difference over the time,

$$C(x,z) = \frac{1}{N-1}\sum_{n=1}^{N-1}\left|\phi_n(x,z) - \phi_{n-1}(x,z)\right| \tag{6.1}$$

In Equation (6.1), the phase difference between adjacent frames is calculated. However, it is also possible to utilize the phase difference between extended time interval depending on the applications. Moreover, we could also calculate the phase variance as,

$$D(x,z) = \sqrt{\frac{1}{N-1}\sum_{n=0}^{N-1}\left|\phi_n(x,z) - \bar{\phi}(x,z)\right|^2} \tag{6.2}$$

where $\bar{\phi}(x,z)$ is the mean value over the entire data stack.

6.2.5.5 Qualitative flow imaging

The flow image was presented in two ways after I subtracted the static background from the raw image. In the first approach, I took the maximum intensity projection (MIP) of acquired 200 B-scans that provided a direct visualization of the beads moving trajectory over time. In the second approach, 200 B-scans were used to construct a color-encoded time-elapsed flow image as described in [92]. This color-encoded flow image provided us with additional qualitative perception of the flow rate.

6.2.5.6 Quantitative flow analysis

I also implemented a quantitative flow analysis to further analyze the flow direction, flow rate, and regional particle statistics. The entire process can be divided into four stages: preprocessing the raw image, locating microspheres within each image, matching microspheres between adjacent frames, and visualizing and calculating the results.

The preprocessing is similar to that described in section Intensity B-scan image6.2.5.1; the images were spatially median filtered and the background was suppressed by using MIP. The preprocessed images were thresholded to produce a series of binary masks, where only the highly scattering microspheres were preserved.

I then calculated the centroid of each microsphere based on the mask frame by frame. After locating all the microspheres in the first frame and recording their location in stacks, I paired the microspheres from the next frame based on following criteria,

The microsphere #m in i^{th} frame was paired with the microsphere #n in $(i+1)^{th}$ frame if and only if the nearest neighbor of microsphere #m in $(i+1)^{th}$ frame is #n and the nearest neighbor of microsphere #n in i^{th} frame was #m.

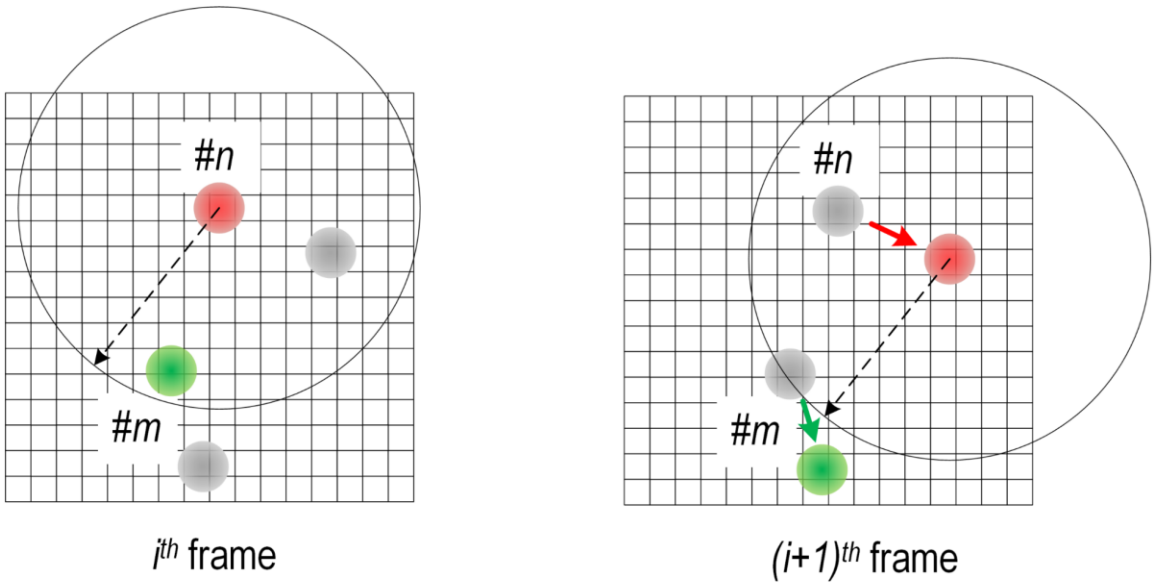

Figure 6-5 A schematic shows the particle pairing algorithm. Starting with the #n bead (red) in i^{th} frame, I first search the image and found #m bead (green) in the neighborhood within a pre-defined radius.

The presumption was that the inter-frame displacement (velocity) of each microsphere was relatively smaller than the distance between neighboring microsphere s. In other words, as long as the frame rate was high to keep the inter-frame displacement low, I could always correctly pair microspheres from frame to frame.

After pairing, the coordinates of the microspheres in the second frame were pushed into the corresponding stacks. By repeating this procedure, I created a series of stacks, each of which corresponds to a unique microsphere. The stacks saved all the evolved coordinates of the microspheres, and the length of an individual stack represents the life time of a microsphere. Therefore, based on the data, I evaluated the parameters of our interest such as the microsphere traveling velocity and its distribution.

6.3 Results

6.3.1 OCT structural image

In order to show the usefulness of OCT, I have taken OCT images from multiple human tracheobronchial samples, and compared them with their corresponding H&E stained tissue section. Figure 6-6 shows a comparison between the OCT images and the corresponding H&E stained section for the intended FOV. The OCT images are taken by using Thorlabs Telesto I system. From the structural OCT images, we could clearly see the structures such as mucus gland duct (MD), mucus secreting glands (MG), and perichondrium (P) with high contrast. However, the boundary between ciliated epithelium (CE) and basement membrane (BM) is not well discriminated in OCT images other than Figure 6-6(a), which is mainly due to the limited axial resolution and low optical contrast between these two layers. The mucous layer is not visualized in the H&E tissue sections due to its removal during tissue processing.

Other than the structural images that show the morphology of the tracheobronchial tissues, OCT images also provided us with an intriguing perspective about the way MCC functions; we were able to directly observe the phenomenon that the residue mucus on the surface of a trachea sample was shielding against the invading foreign objects (5.51-μm polyester microspheres) as shown in Figure 6-7. The OCT B-scan in Figure 6-7(a) illustrates that mucus is secreted from the mucus gland duct. It is worth noting that in these *ex vivo* preparations, the OCT visible mucus is the one that is actively secreted by the mucus grands, which is optically denser, but as the mucus becomes more hydrated and less dense it becomes OCT invisible. In Figure 6-7(b), we could recognize the clean boundary between the water solution filled with microspheres (A) and the mucus layer (M); the polyester microspheres are shielded away from the epithelium by the mucus layer.

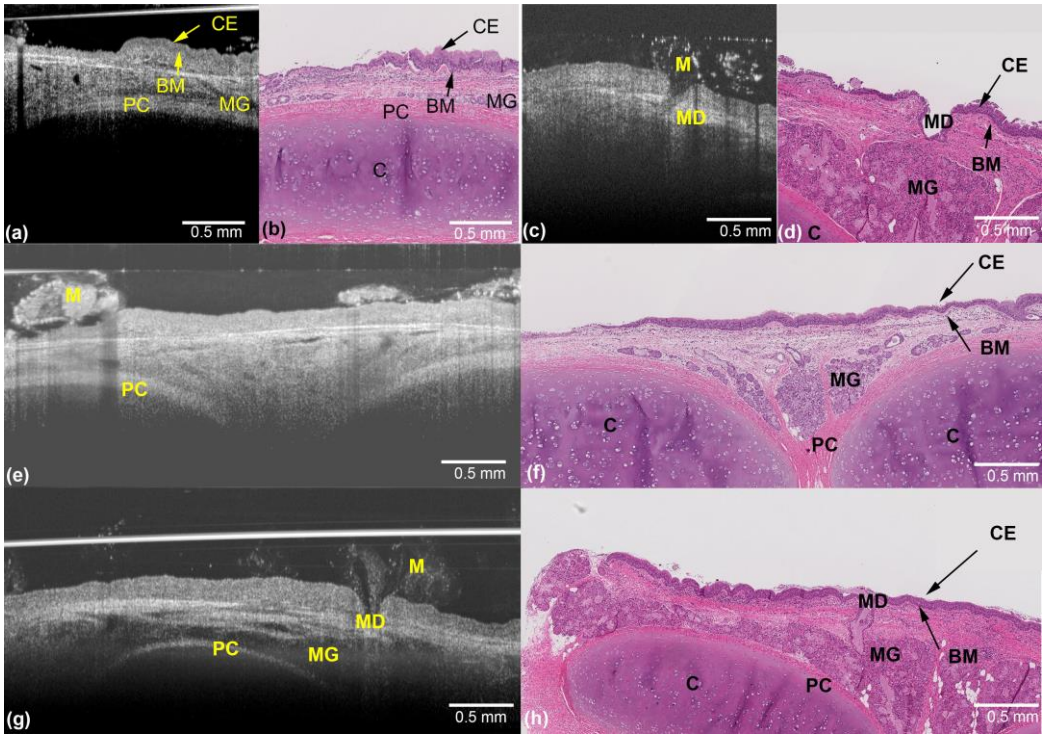

Figure 6-6 Human tracheobronchial tissue OCT images (a), (c), (e), and (g) and corresponding H&E stained tissue section (b), (d), (f), and (h). The OCT images were imaged by Thorlabs Telesto system. BM: Basement membrane, C: Cartilage ring. CE: Ciliated Epithelium, M: Mucus. MG: Mucus secreting glands. MD: Mucus gland duct. PC: Perichondrium.

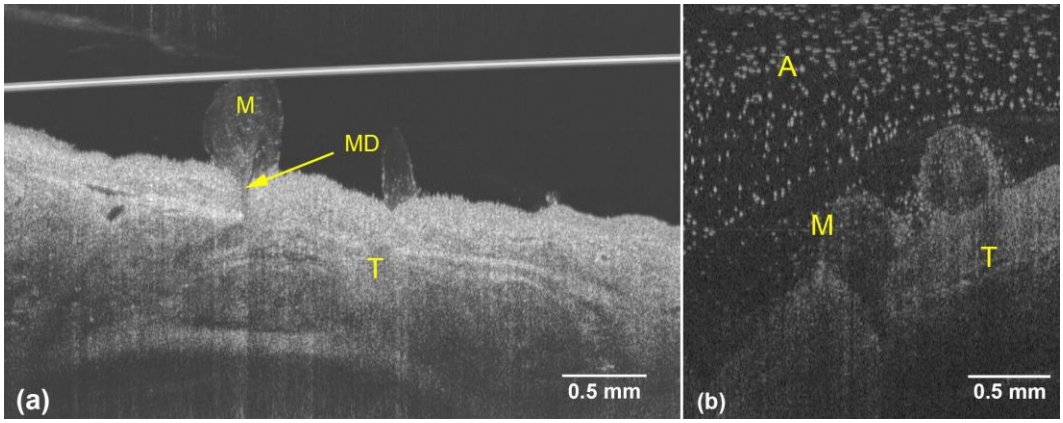

Figure 6-7 Observation of mucus excretion and its effect (a) Mucus secreted from the mucus gland duct. (b) Mucus layer is protecting the epithelium from the microspheres. A: 5.15 μm microspheres. M: Mucus. MD: Mucus gland duct. T: Tracheal wall.

6.3.2 Speckle variance image of ciliated epithelium layer

Although the OCT systems I used in this study do not have sufficient resolution to directly visualize individual cilium, I could indirectly identify intact ciliated regions through speckle variance images as reported in literatures [89, 99]; as the beating of cilia resulted in fluctuations of the acquired OCT image's intensity. Therefore, I can separate the intact ciliated epithelium from the cilia-denuded regions by using the method mentioned in section 6.2.5.2. I present a resultant image by processing Figure 6-6(e) in Figure 6-8, where I also compare the resultant speckle variance image with its corresponding H&E stained tissue section. We could see that an intensified layer covers most of the sample in Figure 6-8(a), which I believe is due to intensified ciliary motions. The speculation is later confirmed by the corresponding H&E stained section. One zoom-in region from the Figure 6-8(a) is shown in Figure 6-8(b), where we can see a uniformly intensified layer on the epithelial surface. From the corresponding H&E stained section in Figure 6-8(c), I could verify that the entire region is covered by dense cilia. On the other hand, I selected another region that shows a discontinued layer of intensified variance in Figure 6-8(d). Comparing it with its corresponding H&E stained section (Figure 6-8(e)), I can recognize that the discontinuity of the layer indeed stems from the absence of the cilia.

A volumetric visualization of ciliated epithelium of human trachea is then presented in Figure 6-9(a), where the speckle variance is color-encoded, thresholded above 0.5, and overlaid against intensity volumetric OCT image. A side-by-side comparison between the structural OCT B-scan and its functional counterpart is also given. In the volume, we can see that the ciliated epithelium only covers the right half of the sample. I believe this might be ascribed to physical injury sustained by the sample during the excision and handling, in which the left half of the ciliated epithelium is denuded by external forces.

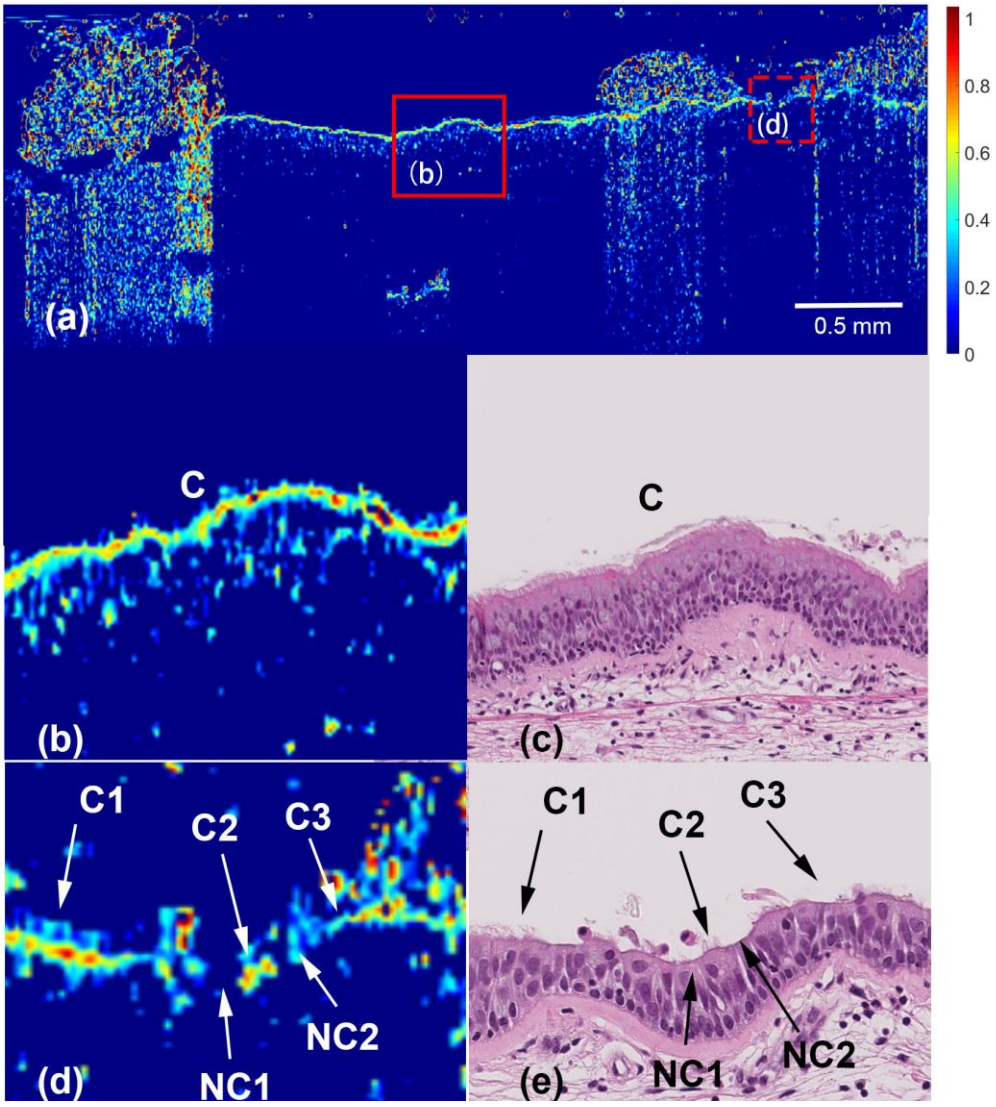

Figure 6-8 The calculated speckle variance image in comparison with its corresponding H&E stained tissue. (a) The calculated speckle variance image, where the ciliated epithelium has a higher variance than other parts of the sample. It is visualized as a layer on top of the specimen. Two zoom-in regions (b) and (d) of the speckle variance image and their corresponding H&E stained tissue (c) and (e). In (b), the entire specimen is covered by ciliated epithelium as confirmed in (c). In (d), there are two regions, where no high contrast layer-like structure is presented. Those two regions are not covered by cilia, which is verified by the H&E stained tissue (e). NC: cilia-denuded. C: ciliated epithelium. Note: the protrusions that C1 pointed to in (d) is really an interpolation artifact instead of cilia. The cilia are represented by the high intensity layer beneath.

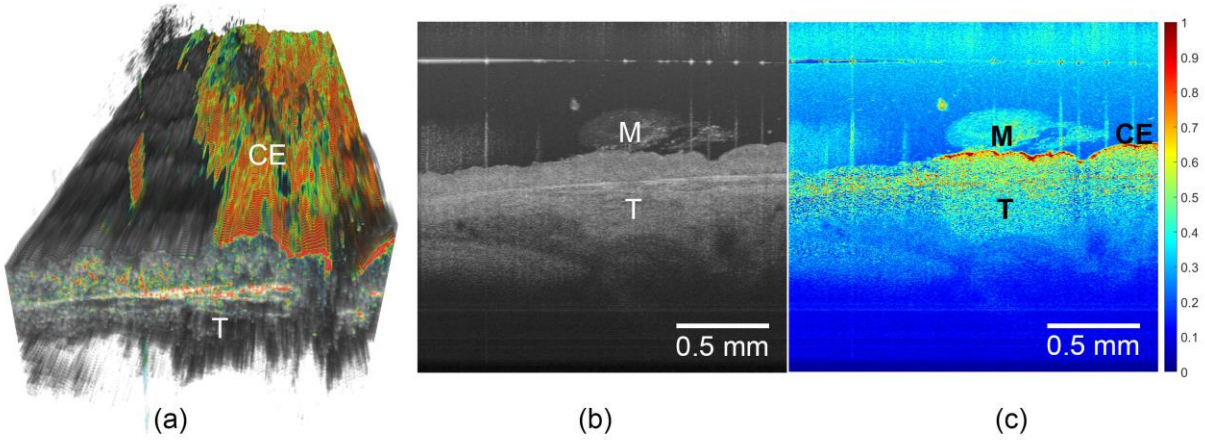

Figure 6-9 Three-dimensional visualization of human tracheal specimen. The volumetric dataset consists of 500 pixels (width) x 45 pixels (length) x 1024 pixels (depth) and was obtained by using the customized scanning protocol with high resolution SDOCT detailed in the method section. (a) Structural image overlaid against threshold variance image. The ciliary motion is only observed on the right half surface of the sample (b) The cross-sectional view of the sample, and (c) its corresponding variance image. M: mucus. CE: ciliated epithelium, which is visible in speckle variance image. T: trachea

6.3.3 Temporal frequency analysis on the ciliary beat frequency

The CBF of 11 regions of 3 donor samples that were immersed in medium were measured. The mean CBF was 8.6 Hz with a standard deviation of 1.0 Hz. I presented a color-coded spatial map of peak amplitudes of dominant frequencies of *ex vivo* human trachea samples taken by the custom-built high-resolution system in Figure 6-10(a). This sample was imaged without being immersed in medium and with an intact dense mucus layer. The pseudo-color map, which indicated the location of the motile cilia, was overlaid with the original intensity OCT image.

By comparing the temporal frequency analysis results with the speckle variance image presented in Figure 6-10(b), the ciliated epithelium on the surface of the tissue was recognized by the temporal frequency analysis, and the mucus artifact presented in speckle variance images were mostly rejected. For example, the artifacts due to the mucus presence in the left part of the speckle

variance image were rejected by the temporal frequency analysis. Zoomed-in views of the ciliated epithelium region were provided in the insets.

In Figure 6-10(c), the dominant frequencies were color-coded and overlaid with the original OCT image. The mean CBF was measured 6.5 Hz ±0.47 Hz. I also picked two locations, one on the ciliated epithelium and the other off, and plotted their temporal spectra in Figure 6-10(d). The red curve, which represents the ciliated epithelium, shows a dominant frequency around 8 Hz, while the spectrum of the cilia-denuded epithelium (blue curve) was more randomly distributed. The mean CBF we measured from the samples was slightly smaller than expected, which can be ascribed to the imperfect tissue preservation protocol.

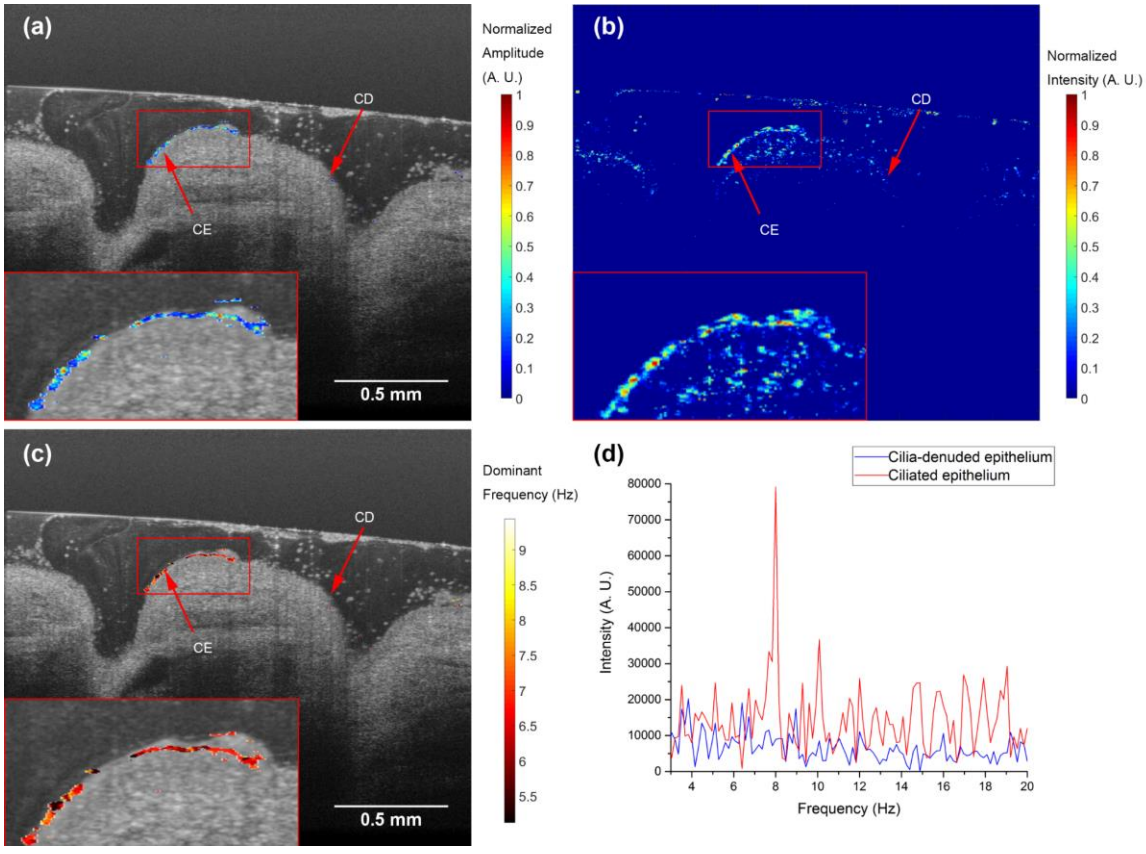

Figure 6-10 The temporal frequency analysis on the ciliary beat frequency of human trachea sample with the presence of mucus layer (sample 13). (a) A color-coded spatial map of dominant frequency amplitude after

thresholding and normalization. The pseudo-color spatial map was overlaid with the original intensity OCT image. (b) Speckle variance image. (c) A color-coded spatial map of dominant frequency. The pseudo-color spatial map was overlaid with the original intensity OCT image. (d) The temporal spectra of two locations. The red curve represents the ciliated epithelium, and the blue curve represents the cilia-denuded epithelium. We observed an 8 Hz peak on ciliated epithelium. The original intensity OCT image was averaged 4 times. All images were taken by the custom-built high-resolution SD-OCT system. CE: ciliated epithelium. CD: cilia-denuded epithelium

6.3.4 Phase variance analysis

I first recorded 2,000 OCT B-scans by using high-speed SS-OCT. An averaged of first 10 OCT B-scans is shown in Figure 6-11, where individual cilia could not be differentiated due to the insufficient resolution. However, and the ciliated epithelium could be segmented from the cilia-denuded area after being processed by speckle variance imaging, temporal frequency analysis, and two different phase variance imaging schemes. The overlaid images are given in Figure 6-12(a), (b), and (c), and (d), respectively. Magnified views are provided for closer examination. All the aforementioned methods generated similar cilia coverage map based on segmentation.

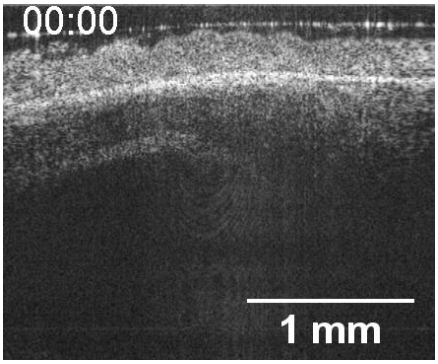

Figure 6-11 Structural image of human ciliated epithelium (averaged 10 times).

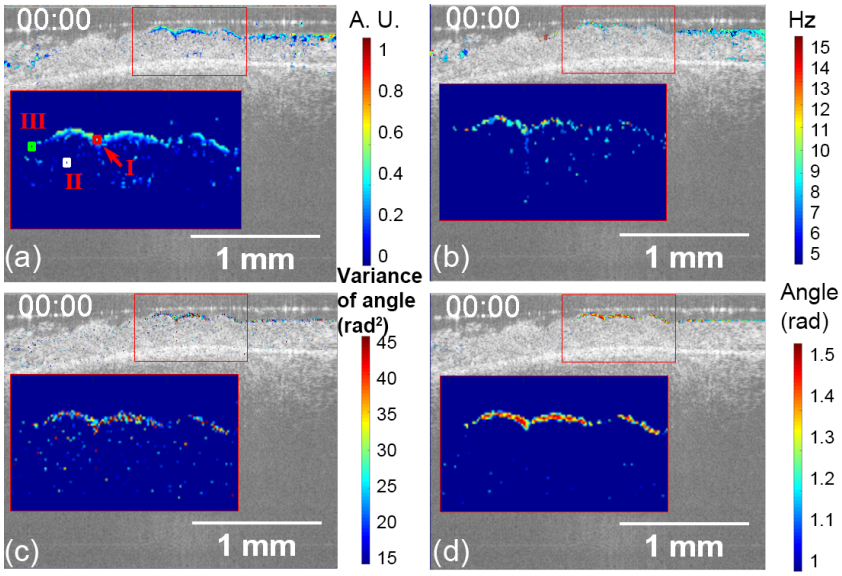

Figure 6-12 Functional imaging of human ciliated epithelium with various techniques. (a) Speckle variance imaging, (b) temporal frequency analysis, (c) phase variance (over the entire 2000 frames), (d) averaged phase difference overlaid on the structural image. We observed elevated contrast from ciliated epithelium region by using all techniques. For better visualization, the structural images are contrast-enhanced. I, II, and III represent for ciliated, background, and cilia-denuded regions, respectively.

I then obtained the frequency response curves at four representative locations (two ciliated sites, one cilia-denuded site, and one air-medium interface site) by using temporal frequency analysis. The frequency response curves are plotted in Figure 6-13(a)-(d). Ciliated site 1 and ciliated site 2 both displayed a pronounced peak around 9 Hz, which is typical for CBF. For the denuded site, I did not see any significant signals above the noise floor. For the high intensity air-medium interface site, I not only observed higher near-DC components (due to the higher intensity in the structural image), but also an enhanced peak around 1 Hz, which might be caused by the low frequency mechanical noise from the medium surface fluctuation. The exact locations of the selected sites are marked in Figure 6-13(e). Figure 6-13(f) gives the histogram and the statistics of the measured CBFs, where the mean is 8.98 Hz and the standard deviation is

2.25 Hz. The CBF statistics agree with the previously reported results (mean CBF is 8.6 Hz with a standard deviation of 1 Hz) [100].

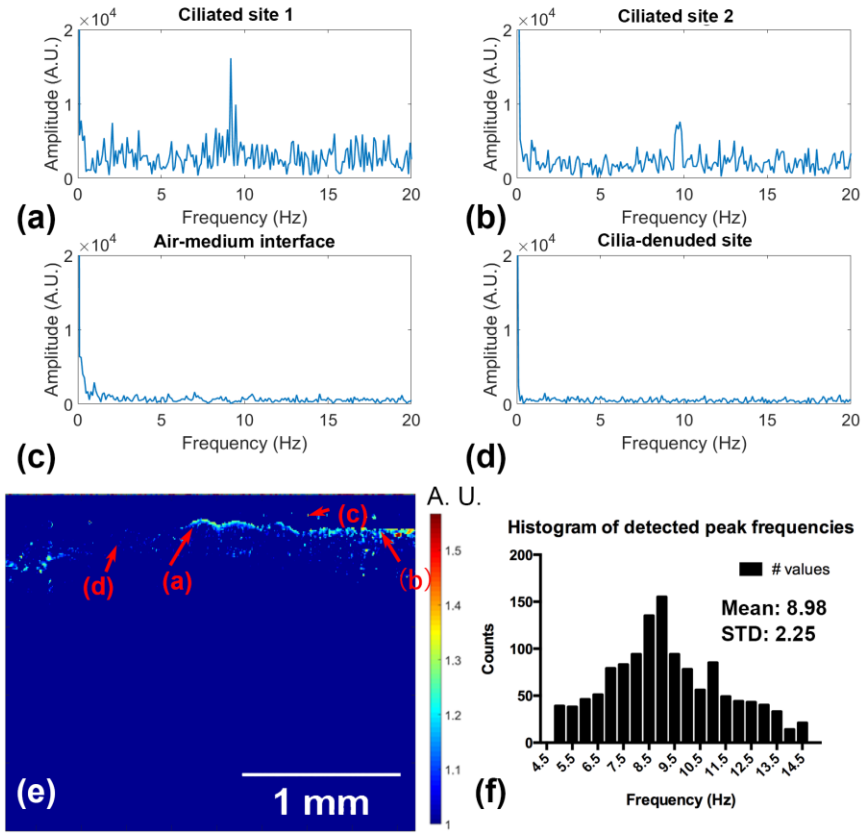

Figure 6-13 The temporal frequency analysis of the human trachea sample. The temporal frequency response of four different locations including (a) ciliated site 1, (b) ciliated site 2, (c) air-medium interface site, and (d) ciliate denuded site. The temporal frequency responses obtained from the cilia sites show very high peaks around 9 Hz, while that of the cilia denuded region has mostly flat response over the entire spectrum. The temporal frequency response measured at air-medium interface presents elevated low frequency components, due to the higher reflectivity or intensity. (e) The selected regions are illustrated and marked in the structural image. All of them are representative single-pixel values. (f) The histogram of the peak frequencies extracted from ciliated sites.

6.3.5 Qualitative flow image

In Figure 6-14, we presented the results by applying both the MIP and color-encoded time lapse imaging as mentioned in section 0. The MIP cilia-driven fluid flow patterns from two human tracheobronchial samples are visualized in Figure 6-14(a) and (c), while their color-encoded counterparts are illustrated in Figure 6-14(b) and (d). The time span for all the images is 16.627 s. The MIP images provide us with a general idea of the flow pattern; the particle path-lines roughly follow the surface topography of the tissue at the beginning, and then they start to circulate whenever the flow is blocked by the dense mucus areas. On the other hand, the color-coded images offer a semi-quantitative picture; the frequency of the change in color could help gain a basic view of the flow rate.

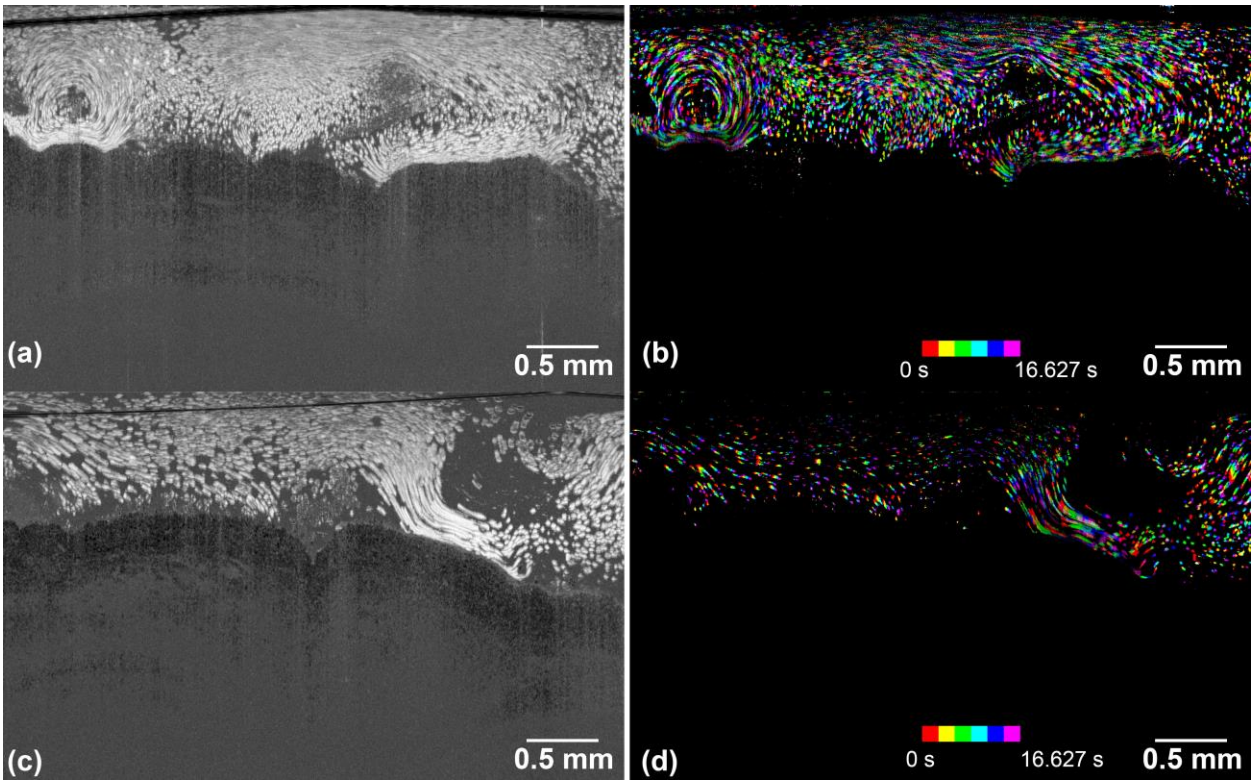

Figure 6-14 The flow images of the microspheres induced by the beating of ciliated epithelium. (a) and (c) are MIP image by integrating all 200 B-scans. (b) and (d) are corresponding color-coded images. The time

span of all the images are 16.627 s, while the 1st eighth interval of the entire time duration is colored by red, the 2nd of that is colored by yellow, …, and 8th of that is colored by purple.

6.3.6 Quantitative flow analysis

The dataset from Figure 6-14(a) is used in this quantitative flow analysis following the procedure in section 6.2.5.6. The results are illustrated in Figure 6-15. The direction of each arrow represents the local averaged direction of particle movements, and the averaged particle velocity is color- and length-encoded. In Figure 6-15(a), I further focused on the statistics of the particles that are in the closest proximity of the ciliated epithelium as shown in the red box. A total number of 2,251 microspheres are tracked and the mean velocity is measured 54.868 μm/s with a standard deviation of 12.327 μm/s, and a corresponding histogram is presented in Figure 6-15(b). The measured particle velocity is consistent with in vivo radioactive particle tracing velocity measurements [101].

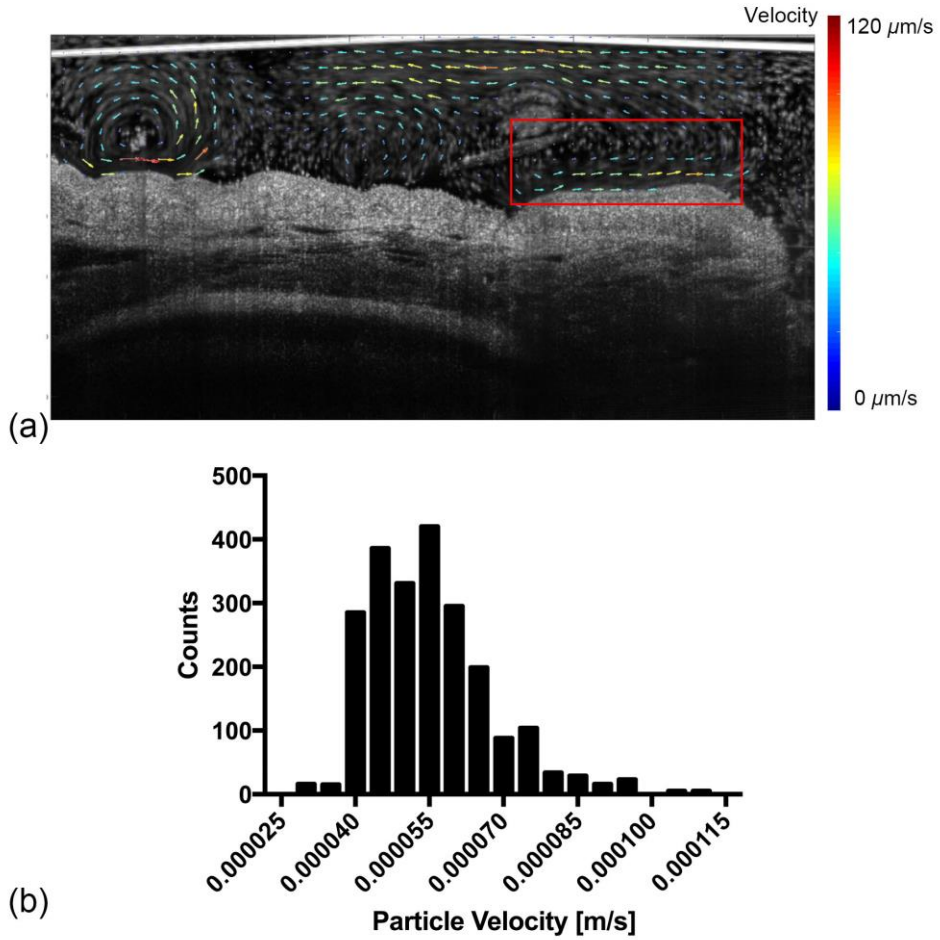

Figure 6-15 The quantitative cilia-driven flow analysis. The dataset is the same as that in Figure 5(a). (a) The vector visualization of flow dynamics. The direction of the arrow represents the averaged flow direction and the flow rate is encoded in both arrow length and color. (b) The histogram of all the tracked particles inside the red box shown in (a). The total time duration is 16.627s and 2,251 microspheres are tracked.

6.4 Discussions

To our best knowledge, this is the first time that ciliary motion on human tracheobronchial tissue as well as its induced flow is simultaneously analyzed by using OCT. With the help of functional OCT technique, including speckle variance imaging, phase variance imaging, and temporal frequency analysis, I successfully differentiated the ciliated epithelium from its cilia-denuded

region and provided important ciliary functions which is promising for future diagnostic purpose. The cilia coverage results were validated by corresponding H&E stained sections. Moreover, both qualitative and quantitative flow analyses were performed to assess the cilia-induced flow direction and rate.

6.4.1 The noise from residual mucus in speckle variance imaging

One of the issues we have encountered in our speckle variance imaging was the adverse influence from the residual dense mucus layer. As illustrated in both Figure 6-3(e) and Figure 6-5(a), the dense mucus layer not only scattered excessive light in structural image, but also introduced noises in speckle variance images and reduce the visibility of cilia.

However, it was possible to utilize the temporal frequency analysis to spectrally filter the signal and reject the noises from the mucus. As I presented in Figure 6-10, the ciliary activities induced dominant frequencies in the temporal frequency domain, and we could use both amplitude and frequency of the dominant frequencies to differentiate the cilia against the mucus [90, 102]. It is worth mentioning that the mucus located in the proximity of the ciliated epithelium possessed a similar dominant frequency as the underlying cilia. However, its peak amplitude was much lower than that of the underlying cilia, and we could reject those signals by carefully thresholding the peak amplitude.

Moreover, it is recently developed in our group that by using a Frequency-constrained robust principal component analysis we could completely segment the dynamic ciliary motion from its stagnating background in the time-elapse images [103].

6.4.2 Study limitations

The human tissues we received were discarded samples from healthy donors. The tissues were bubbled with 95% oxygen and 5% carbon dioxide in medium 199 in the operation room to maintain viability until imaging. This process diluted the mucus concentration from what would be observed *in vivo*. I observed that dense and thick mucus layers reduce the ability to observe the cilia-induced speckle variance signals. Moreover, the presence of mucus prevented microspheres from reaching the ciliated epithelium and thus made it difficult to conduct flow analysis. On the contrary, temporal frequency analysis was robust against the presence of the mucus as shown in section6.3.3. In the future, flow dynamics can be conducted by tracking inherent scatters within thick and dense mucus, as within samples from CF patients, and I can also conduct OCT imaging within physiologically-relevant mucus environment that are comparable to *in vivo* situation by utilizing an air-liquid interface experimental setup [104]. One way of doing this is through utilizing the active mucus secretion (Figure 6-7) from the excised tracheobronchial tissue [59] or I can first unload the mucus attached to the sample upon retrieval, and load with newly secreted mucus. Nevertheless, our current system can be helpful in assessing ciliary motility abnormalities that is primarily due to intrinsic ciliated epithelium defects, such as in PCD.

It was also important to control the temperature of the sample through the entire process; the tissue had to be immediately placed in ice after excision, and bubbled at 4 ℃. After the tissue being transferred to the nutrition solution, it was necessary to gradually heat the nutrition solution up to 37 ℃ and then maintain the temperature at this level throughout the imaging session by using a heating plate. Higher or lower temperature will lead to reduced vitality of the sample and suppressed viability of cilia [105], which thus reduces speckle variance or flow rate.

6.4.3 Measuring CBF by using OCT

CBF is an important parameter in studying MCC. In previous OCT literatures, there is discrepancy in the discussion on how the CBF could be measured. First directly observed by Liu *et al*. in their μ-OCT system, the ciliary motion is manually segmented and measured in the same way as that in high-speed video microscopy. Later, Oldenburg *et al*. attempted to repeat the experiment by using an OCT system with a lightly lower axial resolution (~3 μm), but failed to obtain the frequency peak after Fourier transform the depth resolved profile over the time. They thus concluded that the lack of resolving power for individual cilium might be the reason to miss the spectral signature of the CBF.

However, Wang *et al.* for the first time showed that the frequency peak of ciliary beating, though in mice oviduct, could be extracted from a low-resolution system: the reported axial resolution of their system is only 5 μm.

The difference is really in the spectral resolution and temporal frequency resolution of their system. In Oldenburg *et al*.'s study, only 10 consecutive frames are obtained, which leads to a spectral resolution of larger than 4 Hz. To the contrary, the spectral resolution of the Wang *et al.*'s system is ~0.1 Hz.

This observation agrees well with my experimental results. In our study, three different systems are used, and I observed frequency peaks at the images from the high-resolution system and the SS-OCT system, both of which could continuously acquire large number of frames (high spectral resolution). In fact, this requirement, especially on SS-OCT, has caused me a lot of trouble: the large number of frames is equated to a large amount of data. This makes the already bulk SS-OCT dataset even larger and more difficult to work with.

Chapter 7 Compressive sensing based SS-OCT

Throughout the entire dissertation, I have constantly mentioned the challenges of handling and processing the huge amount of data generated by SS-OCT. And in the last section particularly, I have detailed the issues I encountered when I was trying to take time-lapse imaging of *ex vivo* human trachea sample. In fact, the data transfer and record rate has been recognized as one of the main constraints in SS-OCT system design by Wieser *et al* back in 2014 [45].

The situation is even worse for functional SS-OCT systems, where multiple channels are usually recorded. For example, a simultaneously recorded reference *k*-clock channel [32] or an oversampling scheme [106] is suggested to stabilize the phase of the measurement. It is also the case in polarization-sensitive OCT, where two channels of signals with orthogonal polarization states are usually recorded. To address this issue, we proposed a compressive sensing (CS) based SS-OCT, in which we randomly down-sample the simultaneously recorded reference *k*-clock channel on hardware level and later recover the original signal based on the theory of compressed sensing (CS). In this way, only a fraction of the reference *k*-clock data is digitized during the acquisition. To our best knowledge, this is the first experimental demonstration of CS empowered OCT in which the data is spectrally under-sampled at the time of acquisition.

7.1 Theory

One of the fundamental questions in signal processing is how to sample the signal and precisely reconstruct it. Shannon clearly stated in his profound article that a sampling rate over than 2*B* is required in order to successfully recover a band-limited signal whose bandwidth is 2*B*: a Whittaker–Shannon interpolation formula was suggested to reconstruct the original analog signal

[107]. This teach has guided generations of engineers when designing their communication or measurement system.

It is not until recently, researches started to question whether there is a way to circumvent this limit. Compressed Sensing (CS) is one of the attempts. The mathematical framework of CS was originally developed by Candès and Donoho in 2006 [108, 109]. This theory states that a sparse signal can be recovered from a drastically low amount of randomly sampled data compared with that predicted by Shannon's sampling theorem.

In the case of image acquisition, we would like to reconstruct the true image $x \in R^N$ from a given observation $y=\Phi x \in R^M$ (with $M<<N$), where $\Phi \in R^{M \times N}$ denotes the measurement operator. The image x has a sparse representation with respect to a known dictionary $\Psi \in R^{N \times L}$. It means that there is an image $s \in R^L$ with only S non-zero coefficients ($S << N$), such that $x = \Psi s$. The CS theory implies that, under some constraints, it is possible to recover an estimator $\hat{x}$ of the true image x from the observation y by solving the following convex optimization problem:

$$\hat{x} = \arg\min \left\| \Psi^{\dagger} x \right\|_1 \qquad \text{s. t.} \quad \Phi x = y \tag{7.1}$$

where $\Psi^{\dagger}$ is the pseudo inverse of the operator Ψ.

Most applications of CS exploit the sparsity of images in the direct domain (in a straightforward fashion [110]or through Total-Variation regularization [111]) or using a Wavelet transform to recover an image from a small subset of random Fourier coefficients.

Although this approach is very efficient in theory, the requirement to have access to the Fourier coefficients directly during acquisition is very restrictive. It has been applied successfully

in fields such has MRI [112] and holography [113, 114], but the CS theory struggles to find its way out of these fields.

Indeed, if one considers an image that has a periodic sinusoidal structure, this image has the specificity to contain most of its information inside very few Fourier coefficients. In other words, if a signal is a sum of a few Fourier coefficients, it's by definition sparse in the Fourier domain [56].

Now, consider an image x that has such Fourier-domain sparsity property. I can rewrite the CS problem in Equation (7.1) where the sensing matrix Φ is a direct-domain selection matrix, built by keeping only M out of N lines of the identity matrix, and where the sparsifying matrix Ψ being the Fourier Transform. Now, I can rewrite the optimization problem:

$$\hat{x} = \arg\min \left\| TFx \right\|_1 \qquad \text{s.t.} \quad \Phi x = y \tag{7.2}$$

This technique allows to reconstruct a Fourier-sparse signal from very few direct domain measurements, chosen randomly.

In the case of SS-OCT, the inherent temporal redundancy of the reference *k*-clock signal and its sinusoidal shape make it suitable for CS acquisition directly on the system hardware, with sparsity enforced in the Fourier domain. In practice, the reference *k*-clock signal is subsampled in time, and recovered almost exactly via convex optimization in the Fourier domain.

7.2 Previous research

Two distinct pathways have been taken by OCT researchers. Lebed *et al.* approaches the problem by scanning an under-sampled grid; for a single volume, both a horizontal and vertical scan with skipped B-scans were taken [115]. In this case, the mathematical formulation was different from

the CS; the down-sampling was conducted in direct domain, while the reconstruction was implemented in wavelet domain. More importantly, both domains lack the incoherence required to provide an efficient CS reconstruction [109]. Moreover, the effectiveness of the reconstruction for a predefined scanning pattern is dependent on the content of the volume, which is mostly unknown.

On the other hand, Mohan *et al.* proposed to directly exploit the sparsity of A-line signal/k-domain spectrum [116]. This scheme was later adopted and demonstrated by Liu *et al.* [117]. In their demonstration, the down-sampling process is performed after the full acquisition due to the unavailability of addressable CCD camera, which reduces its practical usage. Similar to the previous approach, the precision of the reconstruction is not guaranteed for an unknown input.

It is interesting to observe that the handful of works mentioned above are performed on SD-OCT, regardless the fact that SS-OCT often generates orders of magnitude more data.

7.3 Experiment configurations and procedures

The schematic of the proposed system is illustrated in Figure 7-1. The simultaneously recorded reference *k*-clock signal is first digitized by A DAQ board at full speed. After that, a predefined pseudo-random mask is applied on the acquired dataset, so that only a small portion of the data is physically transferred to the host computer through the PCIe bus. Therefore, the requirements on the data transfer rate and data storage could be greatly lessened.

Specifically, the down-sampling process was implemented fully on the hardware level. There is a set of 65,536 registers on ATS 9373 (the DAQ board used in the custom SS-OCT system), which originally serves as a data skipping table. It is then programmed to be a data mask and determines whether a specific sampling point is stored or discarded. The value of those

registers could be pre-defined before the acquisition starts, but could not be altered during the acquisition due to the hardware limitation. For example, I could load a vector, which consists of 4,000 randomly sequenced 1s and 0s, to the register. Whenever a sampling trigger signal is received, the next value in the vector will be assessed and the DAQ board will only digitize and transfer the signal if the corresponding value is "1". Otherwise the digitized data will directly be discarded. The vector will simply repeat itself: the value assessed by the DAQ board at the arrival of the 4,001st will be the same as that of the 1st one. However, if I would like to alter the acquisition pattern, I have to disarm the DAQ board and go through the entire configuration process again to set up the new patterns.

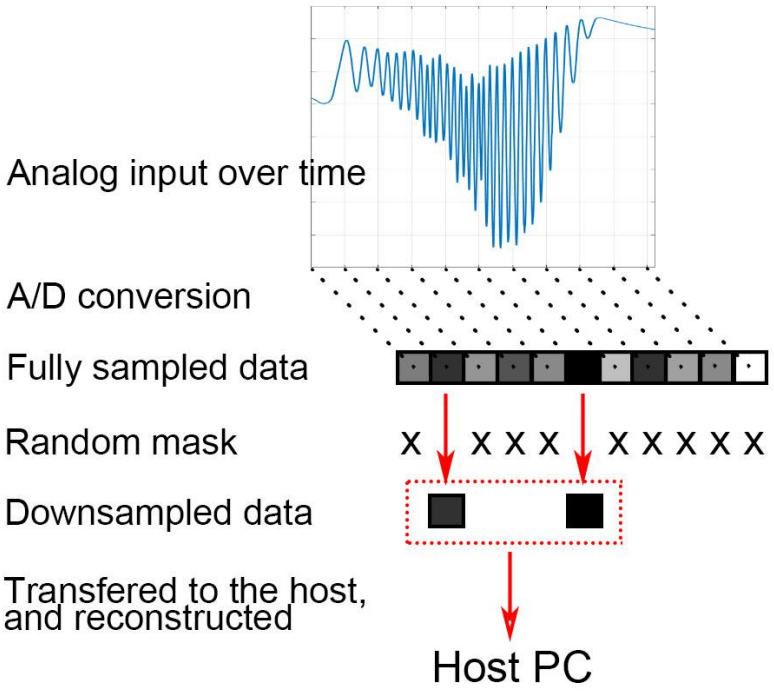

Figure 7-1 Schematic of proposed down-sampling scheme.

In order to make a fair comparison on the reconstruction precision, I added an extra DAQ board to the system to simultaneously acquire a raw copy of the reference *k*-clock channel as a

control. The additional DAQ has to be locked with original DAQ to ensure that there is no jitter between them. A mechanism similar to the "frame trigger" is used here: "AUX I/O" port of both boards is connected to a same function generator. Both DAQ boards are configured so that the acquisition will not start until a TTL trigger is received at "AUX I/O" port. Moreover, both DAQ boards are now triggered by an external sampling clock instead of using their internal crystal oscillator clock.

Convex optimization is solved by using the NESTA algorithm [118], which is very popular in the field of CS. It exploits a fast and accurate gradient descent technique that solves the Equation(7.1), requiring only the tuning of the parameter ε. This parameter can be viewed as a regularization term that enables CS reconstruction on noisy measures. In the present study, I aim for exact reconstruction and set this parameter to 0. Hence, the function to minimize can be rewritten as follows:

$$\hat{x} = \arg\min \left\| Fx \right\|_1 \qquad \text{s.t.} \quad \Phi x = y \tag{7.3}$$

where F denotes the Fourier Transform (either 1D or 2D depending on the data), and represents the acquisition matrix, that basically is a diagonal matrix with ones corresponding to the data that are kept by the mask.

All computations were run using Matlab code, on a PC workstation 2.93 GHz Quad-core CPU with 8GB of RAM, for a running time of 16 seconds for a complete 2048 x 1600 clock signal. In the future, the algorithm will be implemented directly on the computer board, for faster computation and easier usage.

7.4 Experimental results

Before discussing the detailed reconstruction performance, I would like to give the readers a rough impression of the procedure. A fully sampled clock signal from Channel 2 is shown in Figure 7-2(a). In the meantime, another identical DAQ board (Channel 1) was simultaneously down-sampling the same clock signal. The 2-d mask used in this experiment is plotted in Figure 7-2(b). The mask consisted of 2048 ×8 elements and 25% of them are nonzero. The down-sampled clock signal using the mask is illustrated in Figure 7-2(c), while the reconstructed clock channel is presented in Figure 7-2(d). The reconstructed clock signal is almost identical to the original signal, and the residual error is plotted in Figure 7-2(e).

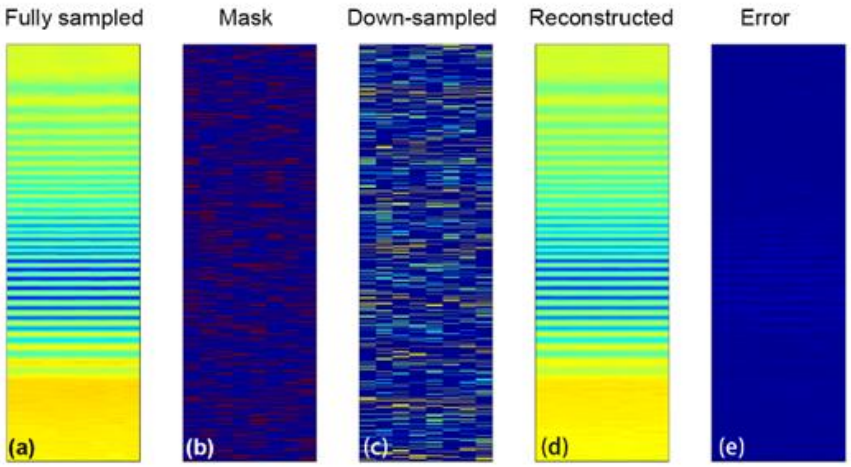

Figure 7-2 Experimental results (a) The fully sampled original clock signal. (b) The randomly generated 2D mask. (c) The resultant down-sampled clock signal. (4) The reconstructed clock signal. (e) The residual error.

7.4.1 Intensity based evaluation

I first evaluate the reconstruction quality based on the correlation between the reconstructed signal and the simultaneously recorded raw signal. Multiple measurements are made at different down-sampling rates and different mask width. For example, 1D mask, 2D mask with a period of 2 A-

lines, 2D mask with a period of 4 A-lines, and 2D mask with a period of 8 A-lines are used, respectively. The results are plotted in Figure 7-3.

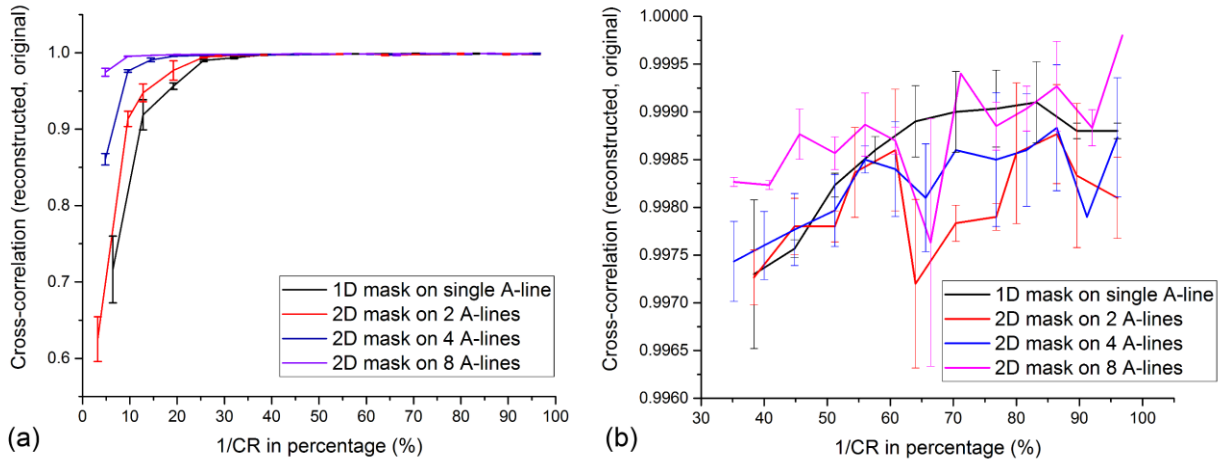

Figure 7-3 The experimental results on the intensity reconstruction quallity. (a)

In Figure 7-3(a), the cross-correlation between the reconstructed signals and the corresponding raw signals are plotted against down-sampling rate, which is represented by the inverse of compression ratio (CR). Different mask schemes are coded in different colors. It is inferred that the cross-correlation improves with less down-sampling, and a 1/CR > 30% could mostly guarantee the construction with a very high fidelity (>0.997) in terms of intensity based cross-correlation. Moreover, it seems that the mask with larger width (more A-lines) lead to better reconstruction especially at lower down-sampling rate but converges when the 1/CR is getting larger than 30%. If I magnify the region (1/CR > 30%), there appears to be little difference between different masking schemes, and the reconstruction quality are saturating.

7.4.2 Phase based evaluation

The evaluation based on intensity is very encouraging. However, the actual utility of the scheme has to be determined by its capability of precise recovering the wavelength sweeping curve and resampling the sample signal.

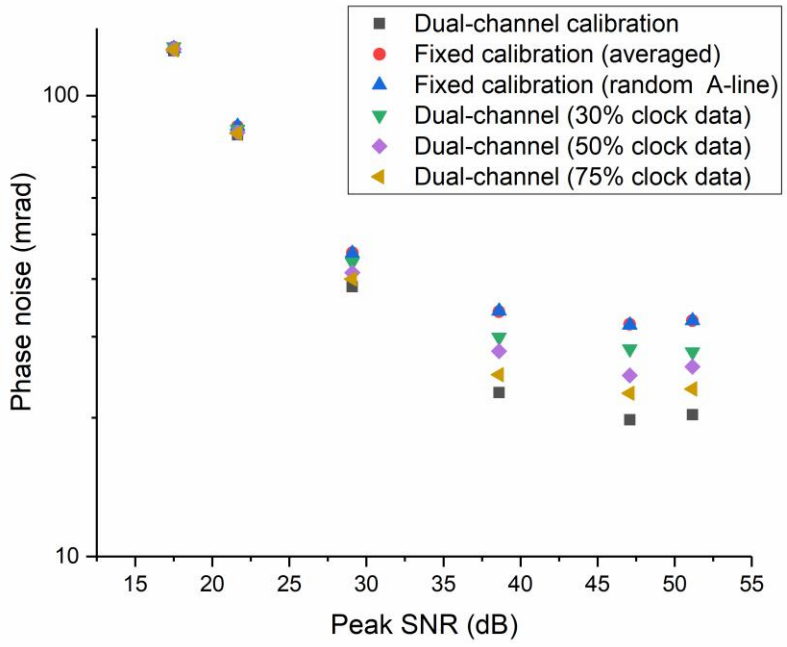

Figure 7-4 Measured phase noise at mirror surface at different SNR levels and different sampling/calibration strategies.

I then performed a standard phase noise measurement on a static No.1 cover glass by following the same procedure as shown in section 5.5. The sample arm is configured in common-path and the sampling rate is set to 800 MS/s. A neutral density filter is inserted in the sample arm to change the SNR of the measurement peak. For the down-sampling channel (Channel 1), three different down-sampling rates (30%, 50%, 70%) are used during the measurement of the reference *k*-clock. The full measurement of the reference *k*-clock is simultaneously recorded in Channel 2. I

first reconstructed the down-sampled measurements based on the compressive sensing theory, and then fed them to the post-processing algorithm at the place of reference *k*-clock signal. I then follow the same analysis detailed in section 5.5, and the resultant phase noise calculated at the mirror surface is plotted in Figure 7-4.

The phase noise after dual-channel calibration is no doubt the smallest, while the usage of either an averaged or a randomly picked instantaneous reference *k*-clock gives the worst performance. This observation matches up with my expectation. In between, the phase noise decreases with the reduced down-sampling rating. However, it is bounded at both ends. It is obvious that the reconstructed reference *k*-clock signal is not as good as the fully sample measurement, but the result is still decent if we consider the largely reduced data size. However, it does present a significant improvement over its non-calibrated counterpart.

7.5 Compressed sensing in sample data compression

In the previous sections, I discussed how the compressed sensing theory could be utilized to compress the reference *k*-clock signal. In this section, I will further explore the possibility of using the same idea on compressing sample data.

Generally speaking, the sample data does not possess the same degree of redundancy as that in reference *k*-clock; the spectral interferogram obtained is rapidly changed with the scene. However, in some special cases, there is some degree of redundancy that we could exploit. One of the prominent examples is the time-elapse imaging, in which most part of the image is static and only a small portion contains dynamic information. This is the exactly the redundancy we are looking for.

7.5.1 Frequency-constrained robust principal component analysis

Robust principal component analysis (RPCA) is a perfect candidate for the job. RPCA has been suggested in segmenting images: part of the image is represented by a low-rank matric, which could be roughly viewed as the stationary background, and the other part is abstracted by a sparse matrix, which is the dynamic foreground [119]. Since its invention, RPCA has been applied in various fields of imaging processing.

However, the RPCA lacks the specificity for the ciliary motion. Therefore, we proposed a modified version of RPCA which imposes additional constrains in frequency domain. The detailed discussion on the technique could be found in [103]. Here, I would like to present some of the results we obtained by using the FC-RPCA.

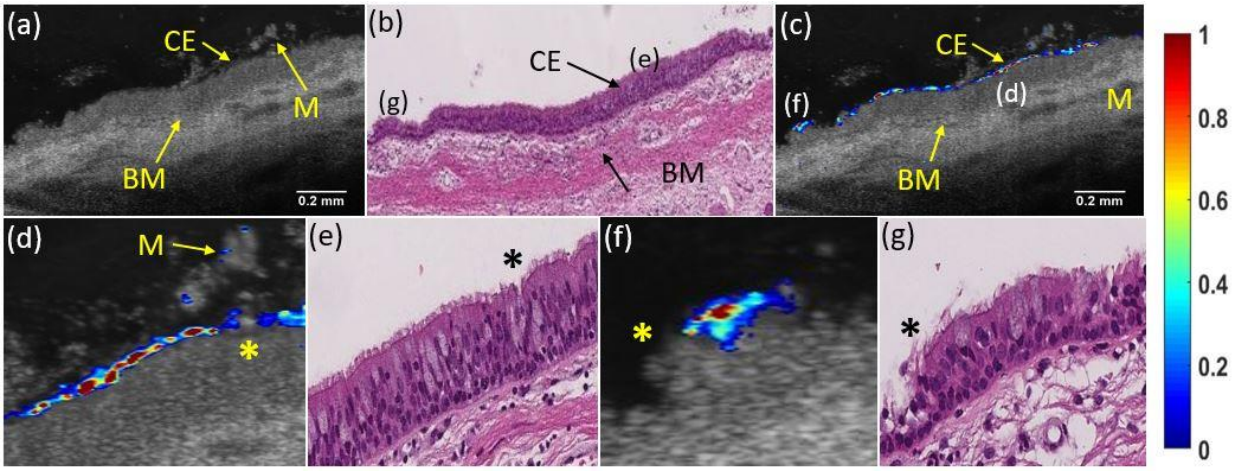

Figure 7-5 (a) *Ex-vivo* OCT B-scan image of ciliated epithelium from human trachea (Sample 5) and (b) corresponding histology. (c) The Maximum Intensity Projection of the FC-RPCA sparse output painted over the image in (a) using MATLAB's jet colormap. (d) A closer look at a dense area of cilia located directly under a mucus cloud from (c). In contrast, (f) examines a sparsely populated area of cilia where the cells may be damaged or non-functioning. (e) and (g) are closer views of the histology corresponding to (d) and (f), respectively. The locations of these two regions are marked with the corresponding figure letter in the full view histology (b) and OCT B-scan (c) images. Colorbar indicates normalized intensity of the FC-

RPCA sparse component. The arrows and corresponding labels mark key physiological regions (CE = ciliated epithelium, BM = basement membrane, M = mucus).

One dataset, its corresponding histology, and FC-RPCA results are shown in Figure 7-5. Arrows in Figure 7-5(a)-(d) are provided to highlight matching physiological features between the OCT B-scan and histology images. The segmentation results are visualized in Figure 7-5(c) which was created by calculating the MIP image from the FC-RPCA sparse component output and overlaying it on the B-scan image shown in Figure 7-5(a). The FC-RPCA overlay in Figure 7-5(d) shows a dense area of cilia directly under a thick mucus cloud. With the exception of the small region directly under the thickest portion of mucus (see asterisk), the algorithm identifies the ciliated area with practically zero false positives from the surrounding mucus. Figure 7-5(f) examines another interesting area where the epithelial cells are partially denuded. In the corresponding histology (Figure 7-5 (g)), the asterisk marks a small area of which appears partially denuded with some potentially non-functioning cilia.

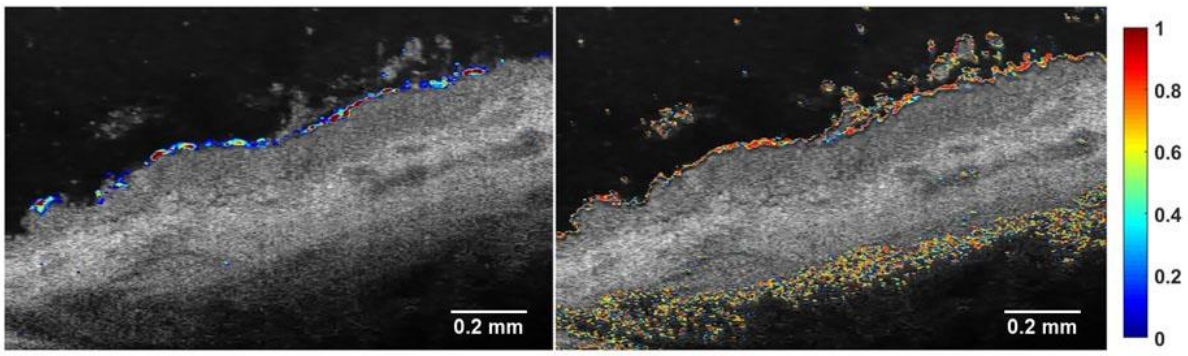

Figure 7-6 Differences between FC-RPCA and Speckle Variance. Left image is the FC-RPCA overlay (the same image shown in manuscript Figure 7-5(c)) and the right is the Speckle Variance overlay for the same dataset.

Moreover, a head-to-head comparison between the FC-RPCA results and the speckle variance results are provided in Figure 7-6. The FC-RPCA rejects most of the noise from mucus and deep tissue.

7.5.2 Discussion

The FC-RPCA results are intriguing. It has both the specificity and sensitivity to segment the ciliary motion. Indeed, it provide us with a natural way to exploit the redundancy in the sample data, at least from a specific type of dataset, which is the time-elapse images. It is highly feasible for us to first acquire a short time OCT video of the sample, and study the its sparsity in the temporal domain by using FC-RPCA. After that, we could design a specific measurement matrix based on CS theory, where only a small portion of the data is needed to reconstruct the full image. The hardware implementation will be in a similar way to what I have done for the reference *k*-clock.

It is also worth mentioning that the size of the mask is currently limited by the total number of the registers, i.e. 65,536. For example, if we have a SS-OCT with an A-line rate of 200 kHz and a sampling rate of 800 MS/s, the maximum size of the mask that we can accommodate is 16 A-lines $\times$ 4000 samples/A-line. In the future, it is possible for us implement our own mask by using FPGA or by using a specifically designed DAQ board.

Chapter 8 Summary and future works

To summarize, I have described a high-speed phase-stable SS-OCT system and its applications in this dissertation. I started with the details of the system development including optical system design, software package coding, and performance tweaking and characterizations. During the development, special considerations are given to handling the high data throughputs. Based on the experimental results, a new phase noise model for SS-OCT is developed. To our best knowledge, this is the first piece of work articulates the multiplicative nature of some typical noise sources in SS-OCT such as the timing jitter and the scanning variability. By using the new theoretical framework, I calibrated the SS-OCT we constructed and reported the best phase noise performance to date. We later use the proposed SS-OCT system along with two other systems to observe the ciliary motion of *ex vivo* human tracheobronchial tissues. Both intensity and phase based techniques are used to measure the ciliary beat frequency as well as the ciliary coverage. New technique, i.e. frequency constrained robust principal component analysis, is proposed to separate and isolate the ciliary motion to better visualization the process. In fact, by using this new technique, we believe we have for the first time observed the metachronal wave-like motion of collective ciliary activities. Finally, to address the issue of the shear amount of data generated by a high-speed SS-OCT, we proposed a novel hardware-based compressive sensing SS-OCT. By exploiting the redundancy in the reference *k*-clock of SS-OCT, I presented that the data rate could be at least reduced by 30% with slightly worse phase performance.

In the future, I am planning to further the study in the following directions.

8.1 Improve the phase stability in SS-OCT based on the new theoretical framework

With the aid of the new theoretical model for phase noise in SS-OCT, we now have a better understanding of the phase noise. It is possible for us to take advantage of the statistical nature of the noise factors such as timing jitter and scanning variability and to bring back the original signal by using advanced statistical inference techniques. In fact, in other areas of signal processing such as radar signal processing, this multiplicative noise has been extensively studied. The same technique could presumably be applied in phase de-noising in SS-OCT as well.

8.2 Observing new features in ciliary motion and connecting it with clinical significance

Ciliary motion is of great importance in clinical settings and there is simply no current technology could facilitate real-time *in situ* diagnostics, except OCT. We have already presented that the phase-stable SS-OCT is a promising tool that could directly measure the ciliary activities in human tissues. In the future, we would like to further extend the study of the ciliary motion and focus more on exploring the link between its biodynamic characteristics and its underlying physiologies. In the meantime, we will try to miniaturize the probe of OCT, and explore the possibility of conducting *in vivo* experiment by using the proposed techniques.

8.3 Study the possibility of using compressive sensing in sample arm

In the dissertation, we have dabbled a little bit on the topic of compressive sensing: we showcased the data reduction capability of using CS in reference *k*-clock. In the future, we would like to further this process to the sample arm as well. We believe this technique will be very suitable for time-elapse imaging, where the inter-frame variation is minimal and a full acquisition of the scenes is very redundant.

Bibliography

[1] M. Born and E. Wolf, "The coherence length: the application of two-beam interference to the study of the fine structure of spectral lines," in *Principles of optics: electromagnetic theory of propagation, interference and diffraction of light* 6th ed.: Pergamon Press, 1980, pp. 316-323.

[2] J. G. Fujimoto, C. Pitris, S. A. Boppart, and M. E. Brezinski, "Optical Coherence Tomography: An Emerging Technology for Biomedical Imaging and Optical Biopsy," *Neoplasia,* vol. 2, no. 1, pp. 9-25, 2000/01/01/ 2000.

[3] J. G. Fujimoto, "Optical coherence tomography for ultrahigh resolution in vivo imaging," *Nat Biotech,* 10.1038/nbt892 vol. 21, no. 11, pp. 1361-1367, 11//print 2003.

[4] R. C. Youngquist, S. Carr, and D. E. N. Davies, "Optical coherence-domain reflectometry: a new optical evaluation technique," *Optics Letters,* vol. 12, no. 3, pp. 158-160, 1987/03/01 1987.

[5] M. Tateda and T. Horiguchi, "Advances in optical time domain reflectometry," *Lightwave Technology, Journal of,* vol. 7, no. 8, pp. 1217-1224, 1989.

[6] E. Brinkmeyer and R. Ulrich, "High-resolution OCDR in dispersive waveguides," *Electronics Letters,* vol. 26, no. 6, pp. 413-414, 1990.

[7] C.-F. Lin and B.-L. Lee, "Extremely broadband AlGaAs/GaAs superluminescent diodes," *Applied Physics Letters,* vol. 71, no. 12, pp. 1598-1600, 1997.

[8] D. S. Mamedov, V. P. Valery, and S. D. Yakubovich, "Superbroadband high-power superluminescent diode emitting at 920 nm," *Quantum Electronics,* vol. 33, no. 6, p. 471, 2003.

[9] R. R. Alfano, *The supercontinuum laser source*, 2nd ed. Springer Science+Business Media, 2005.

[10] D. Malchow, J. Battaglia, R. Brubaker, and M. Ettenberg, "High speed short wave infrared (SWIR) imaging and range gating cameras," in *Defense and Security Symposium*, 2007, vol. 6541, p. 12: SPIE.

[11] R. Guntupalli and R. Allen, "Evaluation of InGaAs camera for scientific near infrared imaging applications," in *SPIE Optics + Photonics*, 2006, vol. 6294, p. 7: SPIE.

[12] R. H. Walden, "Analog-to-Digital Conversion in the Early Twenty-First Century," in *Wiley Encyclopedia of Computer Science and Engineering*: John Wiley & Sons, Inc., 2007.

[13] W. Wieser, W. Draxinger, T. Klein, S. Karpf, T. Pfeiffer, and R. Huber, "High definition live 3D-OCT in vivo: design and evaluation of a 4D OCT engine with 1 GVoxel/s," *Biomedical Optics Express,* vol. 5, no. 9, pp. 2963-2977, 2014/09/01 2014.

[14] D. Huang *et al.*, "Optical coherence tomography," *Science,* vol. 254, no. 5035, pp. 1178-1181, November 22, 1991 1991.

[15] R. A. Costa *et al.*, "Retinal assessment using optical coherence tomography," *Progress in Retinal and Eye Research,* vol. 25, no. 3, pp. 325-353, 2006/05/01/ 2006.

[16] E. A. Swanson and J. G. Fujimoto, "The ecosystem that powered the translation of OCT from fundamental research to clinical and commercial impact [Invited]," *Biomedical Optics Express,* vol. 8, no. 3, pp. 1638-1664, 2017/03/01 2017.

[17] J. M. Schmitt, "Optical coherence tomography (OCT): a review," *Selected Topics in Quantum Electronics, IEEE Journal of,* vol. 5, no. 4, pp. 1205-1215, 1999.

[18] E. Wolf, "Three-dimensional structure determination of semi-transparent objects from holographic data," *Optics Communications,* vol. 1, no. 4, pp. 153-156, 1969/09/01/ 1969.

[19] A. F. Fercher, C. K. Hitzenberger, G. Kamp, and S. Y. El-Zaiat, "Measurement of intraocular distances by backscattering spectral interferometry," *Optics Communications,* vol. 117, no. 1, pp. 43-48, 1995/05/15/ 1995.

[20] G. Haeusler and M. W. Lindner, ""Coherence radar" and "Spectral radar"- new tools for dermatological diagnosis," 1998, vol. 3, p. 11: SPIE.
[21] S. R. Chinn, E. A. Swanson, and J. G. Fujimoto, "Optical coherence tomography using a frequency-tunable optical source," *Optics Letters,* vol. 22, no. 5, pp. 340-342, 1997/03/01 1997.
[22] M. Choma, M. Sarunic, C. Yang, and J. Izatt, "Sensitivity advantage of swept source and Fourier domain optical coherence tomography," *Optics Express,* vol. 11, no. 18, pp. 2183-2189, 2003/09/08 2003.
[23] J. F. de Boer, B. Cense, B. H. Park, M. C. Pierce, G. J. Tearney, and B. E. Bouma, "Improved signal-to-noise ratio in spectral-domain compared with time-domain optical coherence tomography," *Optics Letters,* vol. 28, no. 21, pp. 2067-2069, 2003/11/01 2003.
[24] R. Leitgeb, C. Hitzenberger, and A. Fercher, "Performance of fourier domain vs. time domain optical coherence tomography," *Optics Express,* vol. 11, no. 8, pp. 889-894, 2003/04/21 2003.
[25] A. F. Fercher, "Optical coherence tomography," *Journal of Biomedical Optics,* vol. 1, no. 2, pp. 157-173, 1996.
[26] J. A. Izatt, M. A. Choma, and A.-H. Dhalla, "Theory of Optical Coherence Tomography," in *Optical Coherence Tomography: Technology and Applications*, W. Drexler and G. J. Fujimoto, Eds. Cham: Springer International Publishing, 2015, pp. 65-94.
[27] A. M. Davis, M. A. Choma, and J. A. Izatt, "Heterodyne swept-source optical coherence tomography for complete complex conjugate ambiguity removal," *Journal of Biomedical Optics,* vol. 10, no. 6, pp. 064005-064005-6, 2005.
[28] K. W. Ruikang and M. Zhenhe, "A practical approach to eliminate autocorrelation artefacts for volume-rate spectral domain optical coherence tomography," *Physics in Medicine & Biology,* vol. 51, no. 12, p. 3231, 2006.
[29] R. Tripathi, N. Nassif, J. S. Nelson, B. H. Park, and J. F. de Boer, "Spectral shaping for non-Gaussian source spectra in optical coherence tomography," *Optics Letters,* vol. 27, no. 6, pp. 406-408, 2002/03/15 2002.
[30] W. V. Sorin and D. M. Baney, "Measurement of Rayleigh Backscattering at 1.55 mu m with 32 mu m Spatial Resolution," *IEEE Photonics Technology Letters,* vol. 4, no. 4, pp. 374-376, 1992.
[31] E. A. Swanson, D. Huang, C. P. Lin, C. A. Puliafito, M. R. Hee, and J. G. Fujimoto, "High-speed optical coherence domain reflectometry," *Optics Letters,* vol. 17, no. 2, pp. 151-153, 1992/01/15 1992.
[32] M. Gora *et al.*, "Ultra high-speed swept source OCT imaging of the anterior segment of human eye at 200 kHz with adjustable imaging range," *Optics Express,* vol. 17, no. 17, pp. 14880-14894, 2009/08/17 2009.
[33] E. C. Titchmarsh, "The Zeros of Certain Integral Functions," *Proceedings of the London Mathematical Society,* vol. s2-25, no. 1, pp. 283-302, 1926.
[34] D. Vakman, "DETERMINATION OF CONCEPTS OF AMPLITUDE, PHASE AND INSTANTANEOUS FREQUENCY OF A SIGNAL," *Radiotekhnika i Elektronika,* vol. 17, no. 5, pp. 972-&, 1972.
[35] D. Vakman, "On the analytic signal, the Teager-Kaiser energy algorithm, and other methods for defining amplitude and frequency," *IEEE Transactions on Signal Processing,* vol. 44, no. 4, pp. 791-797, 1996.
[36] L. De Carli and G. S. Samad, "One-parameter groups of operators and discrete Hilbert transforms," *arXiv preprint arXiv:1506.03362,* 2015.
[37] S. Kim, P. D. Raphael, J. S. Oghalai, and B. E. Applegate, "High-speed spectral calibration by complex FIR filter in phase-sensitive optical coherence tomography," *Biomedical Optics Express,* vol. 7, no. 4, pp. 1430-1444, 2016/04/01 2016.
[38] Z. N. Karam, "Computation of the one-dimensional unwrapped phase," Massachusetts Institute of Technology, 2006.

[39] S. H. Yun, G. J. Tearney, J. F. de Boer, and B. E. Bouma, "Motion artifacts in optical coherence tomography with frequency-domain ranging," *Optics Express,* vol. 12, no. 13, pp. 2977-2998, 2004/06/28 2004.

[40] R. J. Zawadzki *et al.*, "Progress on Developing Adaptive Optics-Optical Coherence Tomography for In Vivo Retinal Imaging: Monitoring and Correction of Eye Motion Artifacts," *Ieee Journal of Selected Topics in Quantum Electronics,* vol. 20, no. 2, Mar-Apr 2014, Art. no. 7100912.

[41] M. F. Kraus *et al.*, "Motion correction in optical coherence tomography volumes on a per A-scan basis using orthogonal scan patterns," *Biomedical Optics Express,* vol. 3, no. 6, pp. 1182-1199, 2012/06/01 2012.

[42] B. Potsaid, V. Jayaraman, J. G. Fujimoto, J. Jiang, P. J. S. Heim, and A. E. Cable, "MEMS tunable VCSEL light source for ultrahigh speed 60kHz - 1MHz axial scan rate and long range centimeter class OCT imaging," in *SPIE BiOS*, 2012, vol. 8213, p. 8: SPIE.

[43] M. Bonesi *et al.*, "Akinetic all-semiconductor programmable swept-source at 1550 nm and 1310 nm with centimeters coherence length," *Optics Express,* vol. 22, no. 3, pp. 2632-2655, 2014/02/10 2014.

[44] Y. Ling, X. Yao, and C. P. Hendon, "**Highly phase-stable 200 kHz swept-source optical coherence tomography based on KTN electro-optic deflector**," *Biomedical Optics Express,* vol. 8, no. 8, pp. 3687-3699, 2017/08/01 2017.

[45] W. Wieser, B. R. Biedermann, T. Klein, C. M. Eigenwillig, and R. Huber, "Multi-Megahertz OCT: High quality 3D imaging at 20 million A-scans and 4.5 GVoxels per second," *Optics Express,* vol. 18, no. 14, pp. 14685-14704, 2010/07/05 2010.

[46] D. Choi *et al.*, "Fourier domain optical coherence tomography using optical demultiplexers imaging at 60,000,000 lines/s," *Optics Letters,* vol. 33, no. 12, pp. 1318-1320, 2008/06/15 2008.

[47] Z. Wang *et al.*, "Cubic meter volume optical coherence tomography," *Optica,* vol. 3, no. 12, pp. 1496-1503, 2016/12/20 2016.

[48] B. Park *et al.*, "Real-time fiber-based multi-functional spectral-domain optical coherence tomography at 1.3 μm," *Optics Express,* vol. 13, no. 11, pp. 3931-3944, 2005/05/30 2005.

[49] M. A. Choma, A. K. Ellerbee, C. Yang, T. L. Creazzo, and J. A. Izatt, "Spectral-domain phase microscopy," *Optics Letters,* vol. 30, no. 10, pp. 1162-1164, 2005/05/15 2005.

[50] M. A. Choma, A. K. Ellerbee, S. Yazdanfar, and J. A. Izatt, "Doppler flow imaging of cytoplasmic streaming using spectral domain phase microscopy," *Journal of Biomedical Optics,* vol. 11, no. 2, pp. 024014-024014-8, 2006.

[51] M. Szkulmowski, A. Szkulmowska, T. Bajraszewski, A. Kowalczyk, and M. Wojtkowski, "Flow velocity estimation using joint Spectral and Time domain Optical Coherence Tomography," *Optics Express,* vol. 16, no. 9, pp. 6008-6025, 2008/04/28 2008.

[52] D. C. Adler, R. Huber, and J. G. Fujimoto, "Phase-sensitive optical coherence tomography at up to 370,000 lines per second using buffered Fourier domain mode-locked lasers," *Optics Letters,* vol. 32, no. 6, pp. 626-628, 2007/03/15 2007.

[53] J. Fujimoto and E. Swanson, "The Development, Commercialization, and Impact of Optical Coherence Tomography," *Investigative Ophthalmology & Visual Science,* vol. 57, no. 9, pp. OCT1-OCT13, 2016.

[54] B. E. Bouma *et al.*, "Evaluation of intracoronary stenting by intravascular optical coherence tomography," *Heart,* vol. 89, no. 3, pp. 317-320, 2003.

[55] J. Li *et al.*, "Integrated IVUS-OCT for Real-Time Imaging of Coronary Atherosclerosis," *JACC: Cardiovascular Imaging,* vol. 7, no. 1, pp. 101-103, 2014.

[56] C. P. Fleming, N. Rosenthal, A. M. Rollins, and M. Arruda, "First in vivo real-time imaging of endocardial RF ablation by optical coherence tomography," *The Journal of Innovations in Cardiac Rhythm Management,* vol. 2, pp. 199-201, 2011.

[57] B. E. Bouma, G. J. Tearney, C. C. Compton, and N. S. Nishioka, "High-resolution imaging of the human esophagus and stomach in vivo using optical coherence tomography," *Gastrointestinal Endoscopy,* vol. 51, no. 4, Part 1, pp. 467-474, 2000/04/01/ 2000.

[58] D. C. Adler *et al.*, "Three-dimensional endomicroscopy of the human colon using optical coherence tomography," *Optics Express,* vol. 17, no. 2, pp. 784-796, 2009/01/19 2009.
[59] K. K. Chu *et al.*, "In vivo imaging of airway cilia and mucus clearance with micro-optical coherence tomography," *Biomedical Optics Express,* vol. 7, no. 7, pp. 2494-2505, 2016/07/01 2016.
[60] M. R. Hee, E. A. Swanson, J. G. Fujimoto, and D. Huang, "Polarization-sensitive low-coherence reflectometer for birefringence characterization and ranging," *Journal of the Optical Society of America B,* vol. 9, no. 6, pp. 903-908, 1992/06/01 1992.
[61] K. Jina, B. William, R. M. Jason, L. Howard, and W. Adam, "Functional optical coherence tomography: principles and progress," *Physics in Medicine and Biology,* vol. 60, no. 10, p. R211, 2015.
[62] B. F. Kennedy, K. M. Kennedy, and D. D. Sampson, "A Review of Optical Coherence Elastography: Fundamentals, Techniques and Prospects," *Selected Topics in Quantum Electronics, IEEE Journal of,* vol. 20, no. 2, pp. 272-288, 2014.
[63] AlazarTech, "ATS9373 User Manual," 2015, Available: http://www.alazartech.com/Support/Download%20Files/ATS9373%20User%20Manual_V1_0_4b.pdf.
[64] NVIDIA. (12/14). *cuFFT*. Available: https://developer.nvidia.com/cufft,
[65] NVIDIA. (2013, 12/14). *Quadro K600 Datasheet*. Available: http://www.nvidia.com/content/pdf/data-sheet/nv-ds-quadro-k600-us.pdf
[66] A. Negrean and H. D. Mansvelder, "Optimal lens design and use in laser-scanning microscopy," *Biomed Opt Express,* vol. 5, no. 5, pp. 1588-609, May 1 2014.
[67] M. Watanabe and S. K. Nayar, "Telecentric optics for focus analysis," *Pattern Analysis and Machine Intelligence, IEEE Transactions on,* vol. 19, no. 12, pp. 1360-1365, 1997.
[68] J. S. Ploem, "Laser scanning fluorescence microscopy," *Applied Optics,* vol. 26, no. 16, pp. 3226-3231, 1987/08/15 1987.
[69] R. J. Zawadzki *et al.*, "Adaptive-optics optical coherence tomography for high-resolution and high-speed 3D retinal in vivo imaging," *Optics Express,* vol. 13, no. 21, pp. 8532-8546, 2005/10/17 2005.
[70] Z. Hu and A. Rollins, "Quasi-telecentric optical design of a microscope-compatible OCT scanner," *Optics Express,* vol. 13, no. 17, pp. 6407-6415, 2005/08/22 2005.
[71] V. Milanovic, G. A. Matus, and D. T. McCormick, "Gimbal-less monolithic silicon actuators for tip-tilt-piston micromirror applications," *Selected Topics in Quantum Electronics, IEEE Journal of,* vol. 10, no. 3, pp. 462-471, 2004.
[72] D. Wang, P. Liang, S. Samuelson, H. Jia, J. Ma, and H. Xie, "Correction of image distortions in endoscopic optical coherence tomography based on two-axis scanning MEMS mirrors," *Biomedical Optics Express,* vol. 4, no. 10, pp. 2066-2077, 2013/10/01 2013.
[73] M. Hafez, T. Sidler, and R.-P. Salathe ´, "Study of the beam path distortion profiles generated by a two-axis tilt single-mirror laser scanner," *Optical Engineering,* vol. 42, no. 4, pp. 1048-1057, 2003.
[74] N. A. Nassif *et al.*, "In vivo high-resolution video-rate spectral-domain optical coherence tomography of the human retina and optic nerve," *Optics Express,* vol. 12, no. 3, pp. 367-376, 2004/02/09 2004.
[75] A. Cogliati *et al.*, "MEMS-based handheld scanning probe with pre-shaped input signals for distortion-free images in Gabor-domain optical coherence microscopy," *Optics Express,* vol. 24, no. 12, pp. 13365-13374, 2016/06/13 2016.
[76] V.-F. Duma, "Optimal scanning function of a galvanometer scanner for an increased duty cycle," *Optical Engineering,* vol. 49, no. 10, pp. 103001-103001-9, 2010.
[77] Y. Watanabe and T. Itagaki, "Real-time display on Fourier domain optical coherence tomography system using a graphics processing unit," *Journal of Biomedical Optics,* vol. 14, no. 6, pp. 060506-060506-3, 2009.
[78] M. Harris, "Optimizing Parallel Reduction in CUDA," Accessed on: 11/29/2017Available: http://developer.download.nvidia.com/compute/cuda/1.1-Beta/x86_website/projects/reduction/doc/reduction.pdf

[79] Z. P. Chen, Y. H. Zhao, S. M. Srinivas, J. S. Nelson, N. Prakash, and R. D. Frostig, "Optical Doppler tomography," (in English), *Ieee Journal of Selected Topics in Quantum Electronics,* Article vol. 5, no. 4, pp. 1134-1142, Jul-Aug 1999.

[80] Y. Zhao *et al.*, "Doppler standard deviation imaging for clinical monitoring of in vivo human skin blood flow," *Optics Letters,* vol. 25, no. 18, pp. 1358-1360, 2000/09/15 2000.

[81] B. A. Afzelius, "Cilia-related diseases," *The Journal of Pathology,* vol. 204, no. 4, pp. 470-477, 2004.

[82] R. Ansari, C. Buj, M. Pieper, P. König, A. Schweikard, and G. Hüttmann, "Micro-anatomical and functional assessment of ciliated epithelium in mouse trachea using optical coherence phase microscopy," *Optics Express,* vol. 23, no. 18, pp. 23217-23224, 2015/09/07 2015.

[83] S. Gueron, K. Levit-Gurevich, N. Liron, and J. J. Blum, "Cilia internal mechanism and metachronal coordination as the result of hydrodynamical coupling," *Proceedings of the National Academy of Sciences,* vol. 94, no. 12, pp. 6001-6006, June 10, 1997 1997.

[84] P. Delmotte and M. J. Sanderson, "Ciliary Beat Frequency Is Maintained at a Maximal Rate in the Small Airways of Mouse Lung Slices," *American Journal of Respiratory Cell and Molecular Biology,* vol. 35, no. 1, pp. 110-117, 2006/07/01 2006.

[85] J. J. Armstrong, M. S. Leigh, D. D. Sampson, J. H. Walsh, D. R. Hillman, and P. R. Eastwood, "Quantitative Upper Airway Imaging with Anatomic Optical Coherence Tomography," *American Journal of Respiratory and Critical Care Medicine,* vol. 173, no. 2, pp. 226-233, 2006/01/15 2006.

[86] J. M. Ridgway *et al.*, "Optical Coherence Tomography of the Newborn Airway," *The Annals of otology, rhinology, and laryngology,* vol. 117, no. 5, pp. 327-334, 2008.

[87] S. Han *et al.*, "Evaluation of Tracheal Imaging by Optical Coherence Tomography," *Respiration,* vol. 72, no. 5, pp. 537-541, 2005.

[88] L. Liu *et al.*, "Method for Quantitative Study of Airway Functional Microanatomy Using Micro-Optical Coherence Tomography," *PLoS ONE,* vol. 8, no. 1, p. e54473, 2013.

[89] A. L. Oldenburg, R. K. Chhetri, D. B. Hill, and B. Button, "Monitoring airway mucus flow and ciliary activity with optical coherence tomography," *Biomedical Optics Express,* vol. 3, no. 9, pp. 1978-1992, 2012/09/01 2012.

[90] S. Wang, J. C. Burton, R. R. Behringer, and I. V. Larina, "In vivo micro-scale tomography of ciliary behavior in the mammalian oviduct," *Scientific Reports,* Article vol. 5, p. 13216, 08/17/online 2015.

[91] B. T. Lemieux, J. J. Chen, J. Jing, Z. Chen, and B. J. F. Wong, "Measurement of ciliary beat frequency using Doppler optical coherence tomography," *International Forum of Allergy & Rhinology,* vol. 5, no. 11, pp. 1048-1054, 2015.

[92] S. Jonas, D. Bhattacharya, M. K. Khokha, and M. A. Choma, "Microfluidic characterization of cilia-driven fluid flow using optical coherence tomography-based particle tracking velocimetry," *Biomedical Optics Express,* vol. 2, no. 7, pp. 2022-2034, 2011/07/01 2011.

[93] B. K. Huang, U. A. Gamm, V. Bhandari, M. K. Khokha, and M. A. Choma, "Three-dimensional, three-vector-component velocimetry of cilia-driven fluid flow using correlation-based approaches in optical coherence tomography," *Biomedical Optics Express,* vol. 6, no. 9, pp. 3515-3538, 2015/09/01 2015.

[94] U. A. Gamm, B. K. Huang, M. Syed, X. Zhang, V. Bhandari, and M. A. Choma, "Quantifying hyperoxia-mediated damage to mammalian respiratory cilia-driven fluid flow using particle tracking velocimetry optical coherence tomography," *Journal of Biomedical Optics,* vol. 20, no. 8, pp. 080505-080505, 2015.

[95] J. Danielsson *et al.*, "Antagonists of the TMEM16A Calcium-activated Chloride Channel Modulate Airway Smooth Muscle Tone and Intracellular Calcium," *Anesthesiology,* vol. 123, no. 3, pp. 569-581, 2015.

[96] X. Yao, Y. Gan, C. C. Marboe, and C. P. Hendon, "Myocardial imaging using ultrahigh-resolution spectral domain optical coherence tomography," *Journal of Biomedical Optics,* vol. 21, no. 6, pp. 061006-061006, 2016.

[97] W. Choi *et al.*, "Phase-sensitive swept-source optical coherence tomography imaging of the human retina with a vertical cavity surface-emitting laser light source," *Optics Letters*, vol. 38, no. 3, pp. 338-340, 2013/02/01 2013.
[98] Z. Chen *et al.*, "Phase-stable swept source OCT angiography in human skin using an akinetic source," *Biomedical Optics Express*, vol. 7, no. 8, pp. 3032-3048, 2016/08/01 2016.
[99] B. K. Huang, U. A. Gamm, S. Jonas, M. K. Khokha, and M. A. Choma, "Quantitative optical coherence tomography imaging of intermediate flow defect phenotypes in ciliary physiology and pathophysiology," *Journal of Biomedical Optics*, vol. 20, no. 3, pp. 030502-030502, 2015.
[100] Y. Ling *et al.*, "Ex vivo visualization of human ciliated epithelium and quantitative analysis of induced flow dynamics by using optical coherence tomography," *Lasers in Surgery and Medicine*, vol. 49, no. 3, pp. 270-279, 2017.
[101] W. M. Foster, E. Langenback, and E. H. Bergofsky, "Measurement of tracheal and bronchial mucus velocities in man: relation to lung clearance," *Journal of Applied Physiology*, vol. 48, no. 6, pp. 965-971, 1980.
[102] J. C. Burton, S. Wang, R. R. Behringer, and I. V. Larina, "Three-dimensional imaging of the developing mouse female reproductive organs with optical coherence tomography," 2016, vol. 9716, pp. 97160E-97160E-5.
[103] J. P. McLean, Y. Ling, and C. P. Hendon, "Frequency-constrained robust principal component analysis: a sparse representation approach to segmentation of dynamic features in optical coherence tomography imaging," *Optics Express*, vol. 25, no. 21, pp. 25819-25830, 2017/10/16 2017.
[104] A. A. Pezzulo *et al.*, "The air-liquid interface and use of primary cell cultures are important to recapitulate the transcriptional profile of in vivo airway epithelia," *American Journal of Physiology - Lung Cellular and Molecular Physiology*, vol. 300, no. 1, pp. L25-L31, 2011.
[105] A. B. Christopher *et al.*, "The Effects of Temperature and Anesthetic Agents on Ciliary Function in Murine Respiratory Epithelia," (in English), *Frontiers in Pediatrics*, Original Research vol. 2, no. 111, 2014-October-16 2014.
[106] Y. Ling, Y. Gan, X. Yao, and C. P. Hendon, "Phase-noise analysis of swept-source optical coherence tomography systems," *Optics Letters*, vol. 42, no. 7, pp. 1333-1336, 2017/04/01 2017.
[107] C. E. Shannon, "COMMUNICATION IN THE PRESENCE OF NOISE," (in English), *Proceedings of the Institute of Radio Engineers*, Article vol. 37, no. 1, pp. 10-21, 1949.
[108] E. J. Candes, J. Romberg, and T. Tao, "Robust uncertainty principles: Exact signal reconstruction from highly incomplete frequency information," (in English), *Ieee Transactions on Information Theory*, Article vol. 52, no. 2, pp. 489-509, Feb 2006.
[109] D. L. Donoho, "Compressed sensing," (in English), *Ieee Transactions on Information Theory*, Article vol. 52, no. 4, pp. 1289-1306, Apr 2006.
[110] W. Meiniel *et al.*, "Reducing data acquisition for fast Structured Illumination Microscopy using Compressed Sensing," in *2017 IEEE 14th International Symposium on Biomedical Imaging (ISBI 2017)*, 2017, pp. 32-35.
[111] Y. L. Montagner, E. Angelini, and J. C. Olivo-Marin, "Video reconstruction using compressed sensing measurements and 3d total variation regularization for bio-imaging applications," in *2012 19th IEEE International Conference on Image Processing*, 2012, pp. 917-920.
[112] R. Otazo, E. Candès, and D. K. Sodickson, "Low-rank plus sparse matrix decomposition for accelerated dynamic MRI with separation of background and dynamic components," *Magnetic Resonance in Medicine*, vol. 73, no. 3, pp. 1125-1136, 2015.
[113] M. M. Marim, M. Atlan, E. Angelini, and J.-C. Olivo-Marin, "Compressed sensing with off-axis frequency-shifting holography," *Optics Letters*, vol. 35, no. 6, pp. 871-873, 2010/03/15 2010.
[114] Y. Rivenson, Y. Wu, H. Wang, Y. Zhang, A. Feizi, and A. Ozcan, "Sparsity-based multi-height phase recovery in holographic microscopy," *Scientific Reports*, Article vol. 6, p. 37862, 11/30/online 2016.

[115] E. Lebed, P. J. Mackenzie, M. V. Sarunic, and M. F. Beg, "Rapid volumetric OCT image acquisition using Compressive Sampling," *Optics Express,* vol. 18, no. 20, pp. 21003-21012, 2010/09/27 2010.
[116] N. Mohan, I. Stojanovic, W. C. Karl, B. E. A. Saleh, and M. C. Teich, "Compressed sensing in optical coherence tomography," 2010, vol. 7570, pp. 75700L-75700L-5.
[117] X. Liu and J. U. Kang, "Compressive SD-OCT: the application of compressed sensing in spectral domain optical coherence tomography," *Optics Express,* vol. 18, no. 21, pp. 22010-22019, 2010/10/11 2010.
[118] S. Becker, J. Bobin, and E. J. Candes, "NESTA: A Fast and Accurate First-Order Method for Sparse Recovery," (in English), *Siam Journal on Imaging Sciences,* Article vol. 4, no. 1, pp. 1-39, 2011.
[119] E. J. Candès, X. Li, Y. Ma, and J. Wright, "Robust principal component analysis?," *J. ACM,* vol. 58, no. 3, pp. 1-37, 2011.